Tunneling effects in non-integrable systems and ergodicity of complex classical dynamics

Ryonosuke Koda

Department of Physics
Tokyo Metropolitan University

Thesis submitted for the degree of Doctor of Philosophy in Physics

2024

CONTENTS

Chapter 1 Introduction 3

Chapter 2 Hamiltonian dynamics 7

2.1 Hamiltonian dynamical systems 7
2.2 Properties of non-integrable systems and invariant sets 10
2.3 Energy barriers and dynamical barriers 14

Chapter 3 Quantum tunneling in non-integrable systems and semiclassical theory 17

3.1 tunneling effect in integrable systems 17
3.2 tunneling effect in non-integrable system 20
3.3 Complex semiclassical theory and tunneling effects 21

Chapter 4 Complex dynamics and tunneling effect 25

4.1 One-dimensional complex dynamical systems 25
4.2 Two-dimensional complex dynamical systems 28
4.3 Semiclassically contributing complex orbits and Julia sets 32

Chapter 5 Dynamical tunneling and complex stable manifolds 35

5.1 Intersection of complex stable manifolds in the real plane and the initial manifold 35
5.2 Propagator and the initial manifold 36
5.3 Periodic points of the scattering mapping system 38
5.4 Comparison of the magnitude of the imaginary part of the action along complex orbits 39
5.5 Imaginary actions and dominant complex orbits 39
5.6 Characteristics of dominant orbits 41

Chapter 6 Ergodicity of complex dynamics and quantum tunneling in non-integrable systems 47

6.1 tunneling tails for ultra-near integrable systems 48
6.2 Time-domain semiclassical propagator 56
6.3 Ergodicity in the complex space 57
6.4 Imaginary action of complex paths and the plateau amplitude 63
6.5 Real action of complex paths and quantum resonances 75

Chapter 7 Conclusion 79

Appendix A Exploration of periodic points and numerical methods 83

A.1 Newton method 83
A.2 SD method 84
A.3 DL method 85

Abstract

The purpose of this paper is to study quantum tunneling in non-integrable systems. Quantum tunneling is a phenomenon that allows the transition between regions that cannot be reached by orbits following the classical equations of motion. In contrast to quantum tunneling in one-dimensional systems found in textbooks of quantum mechanics, quantum tunneling occurs under completely different circumstances: in generic non-integrable systems, which are neither completely integrable nor fully chaotic, their phase space becomes is composed of regular and chaotic components. All these components are themselves invariant, so the classical orbits do not connect them. Quantum tunneling in non-integrable systems thus occurs between regions in phase space that are dynamically, not energetically, separated, so the type of tunneling is called dynamical tunneling in the literature [1, 2, 3].

Here we try to clarify essential differences between quantum tunneling in integrable and non-integrable systems by performing the semiclassical analysis in the complex domain. The instanton method is widely known to be a technique to develop the semiclassical theory of tunneling in one dimension or multi-dimensional integrable systems. Since quantum tunneling is a process that is absent in the classical dynamics in the real plane, it would be reasonable to use classical dynamics in the complex plane to describe quantum tunneling in non-integrable systems as well. To this end, recent advances in complex dynamical systems greatly aid our analysis by revealing the nature of invariant sets and the asymptotic behavior of the dynamics.

Based on this, this thesis investigates two problems. The first problem is to specify the most dominant complex path(s) responsible for tunneling transports in the situation where chaotic regions are reasonably large enough compared to the size of the Planck cell. In such situations, there is a rigorous result claiming that the complex paths responsible for the tunneling transition are contained in the Julia set, and these complex paths are well approximated by the complex stable manifolds tending to the chaotic regions in real phase space. Note, however, that this result is merely a necessary condition, and there remain still infinitely many complex paths in the complex region as possible candidates. We try here to narrow down the candidates and explore the principle under which the most dominant paths should satisfy. In particular, for a properly designed scattering map, we examine the imaginary action associated with the stable manifolds for the periodic orbits in the real plane and find that the orbits tending to the sticky zone close to the regular region provide the most dominant contribution in the semiclassical sum. The second problem is to clarify the role of the long time behavior, especially ergodicity in the complex plane, which has been shown to hold even when the real phase space is not ergodic. We show that the ergodicity of complex orbits in the Julia set ensures the connection between arbitrary regions and thus provides an alternative to the instanton path in the non-integrable system. This fact is verified using the ultra-near integrable system [4], in which none of the visible structures inherent in non-integrability exist in classical phase space, but non-monotonic tunneling tails appear in the corresponding wave functions. The simplicity of the complex phase space allows us to explore the origin of the non-trivial tunneling tails in terms of semiclassical analysis in the time domain. In particular, it is shown that not only the imaginary part but also the real part of the classical action plays a role in generating the non-trivial tunneling tails.

Chapter 1

Introduction

The aim of this thesis is to investigate tunneling effects in systems with two or more degrees of freedom. While systems with one-degree-of-freedom are always integrable in classical mechanics, those with more than one-degree-of-freedom are generally non-integrable. The nature of quantum tunneling significantly depends on whether the corresponding classical system is integrable or not, even though tunneling effect is a purely quantum phenomenon. Clarifying this difference is the main objective of this thesis.

The tunneling effects are state transitions that are forbidden in classical physics. The type of tunneling barrier differs between integrable and non-integrable systems. In integrable systems, the barrier is only formed energetically. In this case, if the energy of a particle exceeds a potential barrier, a state transition across the barrier is possible. In non-integrable systems, however, there are regions on connected surfaces of equi-energy where state transitions are not possible. Such a barrier is called dynamical barrier and tunneling through such a type of barriers is referred to as *dynamical tunneling* [1, 5].

In non-integrable systems, the tunneling effect is known to exhibit anomalous enhancement due to the influence of chaos. Lin and Balletin [6] have reported, by using a double well potential system that in non-integrable systems, the tunneling probability increases compared to integrable systems. Bohigas and Tomsovic argued that the origin of the enhancement would be the coupling between tunneling doublets and states localized in chaotic regions. Such a mechanism is referred to as *chaos assisted tunneling* (CAT) [7, 8, 9]. Later, it was pointed out nonlinear resonances, another characteristic structures inherent in non-integrability of the system, could play the role of a significant enhancement of tunneling probability. Such a mechanism is called the *resonance assisted tunneling* (RAT) [10, 11, 12, 13, 14, 15, 16, 17].

In this thesis, we explore the origin of the enhancement observed in tunneling effects in non-integrable systems based on the complex semiclassical approach.

Chaos is a phenomenon observed in classical mechanics. Therefore, if we want to find signatures of chaos in quantum mechanics, we must somehow relate quantum mechanics to classical mechanics. Since the relation between classical and quantum mechanics has a similar mathematical structure as that between the geometrical and wave optics, it makes sense to explore the relation between classical and quantum mechanics in the short-wavelength limit. Semiclassical analysis has been developed exactly for this purpose, and it has been a standard tool in the study of *quantum chaos*. However, this is not sufficient to study the manifestation of classical chaos in quantum tunneling. This is because tunneling effect are absent in classical mechanics even in the short-wavelength limit. There are no classical counterparts of quantum tunneling. The most common strategy to deal with purely quantum phenomena would be to extend the classical mechanics into the complex plane and use the complex classical trajectories. The so-called instanton is the most widely recognized idea that is used to compute energy level splitting caused by tunneling effect [17, 18]. Here we apply the semiclassical method extended to the complex plane to study the tunneling effects in non-integrable systems [19, 20].

There are two major challenges in analyzing the complex semiclassical analyzing the tunneling effect in non-integrable systems based on the complex semiclassical theory. The first is to find the most dominant complex orbits among the candidate complex paths. In integrable systems, the complex path that appears in the evaluation of tunneling-related quantities is the instanton that runs along the imaginary time direction. In non-integrable systems, however, there are no more instanton paths; instead, an infinite number of paths could appear in the complex plane, which are inherent to nonintegrability. Therefore, it becomes necessary to sort out which complex orbits are most dominant and which are negligible in their magnitude.

The second challenge is the Stokes phenomenon [21, 22]. The main task to develop the semiclassical analysis in the complex domain is to perform the saddle point approximation of a given integral, usually expressed in the form of an infinite or multiple integral. In the saddle point analysis, it is known that not all the saddle points do not contribute in the evaluation. This is because the Stokes phenomenon happens in the complex plane and treating the Stokes phenomenon is inevitable in the complex semiclassical analysis.

In this thesis, we take a simple discrete dynamical system as a model to study quantum tunneling in non-integrable systems. A major advantage of using the discrete dynamical system is that we can make full use of recent results on complex dynamical systems in multidimensions obtained by mathematicians in the field of complex dynamical systems. In particular, Bedford and Smillie have published a series of papers establishing the foundations of polynomial diffeomorphism in the complex plane [23, 24, 25, 26]. Their results are helpful for our issues on quantum tunneling in non-integrable systems because their main statements suggest the existence of complex paths alternative to the instnaton orbit in the integrable system.

Based on mathematical results, it was found that the complex orbits that control quantum tunneling in non-integrable systems are contained in the *Julia set* and the rest of the orbits in the complex plane have no chance to contribute to the state transition due to tunneling [27]. Here the Julia set is a natural extension of the chaotic set in the real dynamics. Since the orbits in the Julia set can be approximated by stable/unstable manifolds in the complex plane [24], one can say that the tunneling transport in non-integrable systems occurs along stable/unstable manifolds [28]. Their results are remarkable in that they claim that tunneling in non-integrable systems is driven by chaotic orbits in the complex plane, which is in a sharp contrast to the complex path responsible for tunneling in integrable systems. However, there exist exponentially many orbits in the Julia set, and it is not yet clear whether they contribute equally to tunneling transitions. Therefore, the next task and one of the purposes of this thesis are to specify the most dominant complex orbit(s) among the candidates contained in the Julia set.

Dynamical tunneling is a process that proceeds in a mixture of classically forbidden and allowed processes. Semiclassical calculations can only provide transition probabilities associated with this entire process. In other words, one cannot clearly separate the contribution from the pure tunneling process in the regular regions from the process involving chaotic transport. The second task and the second objective of this thesis will be to clarify the essential difference between the nature of tunneling in completely integrable and non-integrable systems. To this end, we have to eliminate the influence of chaos as much as possible, otherwise contamination of chaotic transports and pure tunneling processes arises, which makes it difficult to extract unique signatures in tunneling owned only by non-integrable systems.

The organization of this thesis is as follows. In Chapter 2, we provide a brief background and basic notions of Hamiltonian systems. In particular, we explain the signature of the classical phase space in generic Hamiltonian systems and introduce dynamical barriers, which play a central role in tunneling effects in non-integrable systems. In Chapter 3, we show a standard treatment of quantum tunneling in terms of complex orbits in one-dimensional systems, and then give a semiclassical formulation that is used to analyze tunneling effects in the multi-dimensional system. In Chapter 4, we present mathematical results for complex dynamical systems, focusing in particular on several key theorems proved by Bedford and Smillie. It begins with an explanation of one-dimensional complex dynamical systems, followed by a detailed discussion of precise results from the Hénon map. The orbits in the Julia set are shown to be ergodic regardless of the underlying classical dynamics in the real plane. In Chapter 5, we numerically verify that some fundamental properties predicted by the theory of complex dynamical systems in multi-dimensions can actually be observed, and then investigate natures of stable/unstable manifolds since they guide the complex orbits controlling the tunneling transition in non-integrable systems. In particular, for a properly designed scattering map, we examine the complex orbits associated with the stable manifolds for the periodic orbits in the real plane, and seek the complex orbits that provide the most dominant semiclassical contribution. In Chapter 6, we investigate the ultra-near integrable system, which was recently introduced to study tunneling effects in the situaiton where the influence of chaos is minimal. We say that the system is ultra-near integrable if the system is sufficiently close to a certain integrable limit such that none of the classical invariant structures inherent in non-integrability are visible in the classical phase space, compared to the scale of the Planck cell. Here we show that the ergodicity of complex orbits in the Julia set ensures the connection between arbitrary regions and thus provide an alternative to the instanton path in the non-integrable system. The simplicity of the complex phase space in the ultra-near-integrable system allows us to explore the origin of non-trivial tunneling tails, which have been discovered in exact quantum calculations, in terms of semiclassical analysis in the time domain. The origin of the enhancement of the tunneling probability is explained on the basis of a purely semiclassical analysis. Chapter 7 summarizes the results and discusses future prospects.

Chapter 2

Hamiltonian dynamics

As mentioned in Introduction, the tunneling effect in quantum mechanics could be influenced by the corresponding classical system. Since chaos is a concept in classical mechanics, it is necessary to have a better understanding of chaos in classical mechanics in order to investigate signatures of chaos in the tunneling effect. In this chapter, we give an overview of classical mechanics of non-integrable systems. Another purpose of this chapter is to explain dynamical barriers which are formed in phase space of non-integrable systems. The tunneling effect studied in this thesis is not the one occuring when the barriers are formed eneregetically, but dynamically.

2.1 Hamiltonian dynamical systems

This section begins by introducing fundamental concepts of Hamiltonian dynamics and then proceeds with explaining the mechanism generating chaos. First, the definition of integrability of Hamiltonian systems is provided. Then, we emphasize the importance and the role of invariant sets in phase space.

2.1.1 Canonical equations and Hamiltonian flow

Let us consider a Hamiltonian $H(\boldsymbol{p},\boldsymbol{q};t)$ of N degrees of freedom where $\boldsymbol{q}=(q_1,\cdots,q_N)$ and $\boldsymbol{p}=(p_1,\cdots,p_N)$. The canonical equations of motion of the Hamiltonian system can be rewritten in the following form [29]:

$$\dot{\boldsymbol{z}} = J\nabla H. \tag{2.1}$$

where,

$$J = \begin{pmatrix} O_N & I_N \\ -I_N & O_N \end{pmatrix}, \tag{2.2}$$

I_N and O_N represent the $N \times N$ identity matrix and zero matrix, respectively. Furthermore, let us denote:

$$\boldsymbol{z} = (\boldsymbol{q},\boldsymbol{p}) \ \ (\boldsymbol{z} \in \mathbb{R}^{2N}). \tag{2.3}$$

Using the Poisson bracket, the equations (2.1) can be written as,

$$\dot{\boldsymbol{z}} = \{\cdot, H\}. \tag{2.4}$$

Here, the Poisson bracket is defined as follows:

$$\{A,B\} := \sum_i \left(\frac{\partial A}{\partial q_i}\frac{\partial B}{\partial p_i} - \frac{\partial A}{\partial p_i}\frac{\partial B}{\partial q_i} \right), \tag{2.5}$$

and

$$X_H := \sum_i \left(\frac{\partial H}{\partial p_i}\frac{\partial}{\partial q_i} - \frac{\partial H}{\partial q_i}\frac{\partial}{\partial p_i} \right), \tag{2.6}$$

is referred to as the Hamiltonian vector field, which leads to the flow of the canonical equations. The Hamiltonian remains constant along the orbits of the Hamiltonian vector field.

2.1.2 Integrable systems

Here, we introduce the integrability of Hamiltonian systems. First, let us consider differential equations in general, not limited to Hamiltonian systems. Here, we discuss differential equations in the following form [30]:

$$\dot{x}_i(t) = f_i(x_1(t), x_2(t)\cdots, x_N(t)) \ \ (i = 1,\ldots,N,\ f_i \in \mathbb{R}). \tag{2.7}$$

A differential equation or a system of differential equations is considered to be integrable if its solution can be obtained through a finite number of operations. These operations include arithmetic operations, differential operations, indefinite integral operations, inverse function operations, and solving algebraic equations. The integrability of the system of differential equations is determined by the existence of the first integral. The first integral is a function $\Phi(x_1(t), x_2(t), \cdots, x_N(t))$ defined over $\mathbb{R}^N$ that keeps a constant value along the solution orbit $x_i(t)$. For a general N-dimensional differential equation, having $N-1$ constants of motion is sufficient such that the system is integrable.

Now, let us turn to the condition for the integrability of canonical equations. Since the Hamiltonian equations of motion for N degrees of freedom is a system of differential equations with $2N$ unknown functions, one might expect that one needs to find $2N-1$ constants of motion in order to be integrable.

However, according to the Liouville-Arnold's theorem [31], it is known that canonical equations can be solved using only N constants of motion.

Theorem (Liouville-Arnold [31]). *Consider an N-dimensional Hamiltonian system H with N conserved quantities. If there exist N first integral $F_1, \ldots, F_N$, satisfying for any i, j $(i, j = 1, \cdots, N)$ that*

$$\{F_i, F_j\} = 0, \tag{2.8}$$

then the system is integrable. In this case, the orbits are confined to:

$$M_{\boldsymbol{c}} := \left\{ (\boldsymbol{q}, \boldsymbol{p}) \in \mathbb{R}^{2N} \mid F_i(\boldsymbol{q}, \boldsymbol{p}) = c_i,\ (i = 1, \ldots, N) \right\}, \tag{2.9}$$

where $\boldsymbol{c} = (c_1, \ldots, c_N)$ *is* N*-dimensional real-valued vector, and* M_c *forms the* N*-dimensional torus. Furthermore, there exists a coordinate transformation* $(\boldsymbol{q}, \boldsymbol{p}) \mapsto (\boldsymbol{I}, \boldsymbol{\theta})$*, and* $(\boldsymbol{I}, \boldsymbol{\theta})$ *are referred to as the action-angle variables. Here, the action and angular variables are defined as follows,*

$$\boldsymbol{I} = \frac{1}{2\pi} \oint_{M_c} \boldsymbol{p} \cdot d\boldsymbol{q}, \;\; \boldsymbol{\theta} = \frac{\partial G}{\partial \boldsymbol{J}} \;\; (\boldsymbol{J} := 2\pi \boldsymbol{I}), \tag{2.10}$$

G *is the generating function of the canonical transformation* $(\boldsymbol{q}, \boldsymbol{p}) \mapsto (\boldsymbol{I}, \boldsymbol{\theta})$*:*

$$G(\boldsymbol{q}, \boldsymbol{I}) = \int \boldsymbol{p}(\boldsymbol{q}_0, \boldsymbol{I}) \cdot d\boldsymbol{q}_0. \tag{2.11}$$

Here, we assumed that $\boldsymbol{I} = \boldsymbol{I}(\boldsymbol{q}, \boldsymbol{p})$ can be solved for $\boldsymbol{p}(\boldsymbol{q}, \boldsymbol{I})$. Unless otherwise specified, when we mention *integrable* in the following, it refers to the integrability in the sense of Liouville-Arnold's theorem. If the Hamiltonian system is integrable, the equations of motion in the transformed coordinates become:

$$\frac{d\theta_i}{dt} = -\frac{\partial H}{\partial I_i} = \omega_i, \;\; \frac{dI_i}{dt} = 0 \quad (i = 1, 2, \ldots, N), \tag{2.12}$$

which yield the trivial solution as $I_i = \text{const}$ and $\theta_i = \omega_i t + \alpha_i$ $(\alpha_i \in \mathbb{R})$.

In the case of a two-degree-of-freedom system, when the ratio ω_1/ω_2 of frequencies is rational, the motion is called rational rotation; when ω_1/ω_2 is irrational, the motion is called irrational rotation. The rational rotation leads to periodic orbits. On the other hand, in the case of irrational rotation, the orbit does not exactly return back to the initial point, but rather it densely moves on the torus. Moreover, for an N-degree-of-freedom system, it is a rational rotation when there exists an integer vector $\boldsymbol{k}$ satisfying the following conditions:

$$\boldsymbol{k} \cdot \boldsymbol{\omega} = 0 \; (\boldsymbol{k} \neq 0). \tag{2.13}$$

As we will discuss below, the fates of orbits under weak perturbations depending on the rationality of the motion. In the case of rational rotation, the orbit becomes periodic. In contrast, in the case of irrational rotation, it becomes quasi-periodic, as we will explain in the subsequent sections.

2.1.3 Autonomous and non-autonomous systems

Hamiltonian systems whose Hamiltonian does not explicitly depend on time are referred to as autonomous systems. In autonomous systems, the motion is confined to an energy surface $H = E$. On the other hand, Hamiltonian systems with explicit time dependence are called non-autonomous systems. Let us consider a one-degree-of-freedom non-autonomous Hamiltonian system whose Hamiltonian is denoted by $H(q, p; t)$. If the one-degree-of-freedom Hamiltonian depends periodically on time, i.e., $H(q, p; t + T) = H(q, p; t)$ with a certain period T, the system is often called a 1.5-degree-of-freedom system. Hereafter we will employ this type of Hamiltonian as a model to study the quantum tunneling effect. We can regard 1.5-degree-of-freedom Hamiltonian system as a two-degree-of-freedom autonomous system by introducing the so-called extended coordinate space [32]. Given the Hamiltonian $H = H(q, p; t)$, the canonical equations of motion read:

$$\frac{dq}{dt} = \frac{\partial H}{\partial p}, \tag{2.14}$$

$$\frac{dp}{dt} = -\frac{\partial H}{\partial q}. \tag{2.15}$$

We introduce extended coordinate space $(q_0, q_1) := (t, q)$ and parameterize the orbits by $s \in \mathbb{R}$. Considering the canonical conjugate variables (p_0, p_1) associated with (q_0, q_1), we can treat this as a two-degree-of-freedom autonomous system with variables (q_0, q_1, p_0, p_1). We then introduce new variables q_0' and q_1' as,

$${q_0}' := \frac{dq_0}{ds}, \tag{2.16}$$

$${q_1}' := \frac{dq_1}{ds} = \dot{q}_1 \frac{dq_0}{ds} = \dot{q}_1 q_0'. \tag{2.17}$$

Here dot denotes the differentiation with respect to time t. The action integral in the extended coordinate space can be expressed as:

$$\begin{aligned}\int L(q, \dot{q}; t) dt &= \int L(q_0, q_1, \frac{{q_1}'}{q_0'}) \frac{dq_0}{ds} ds \\ &= \int L(q_0, q_1, \frac{{q_1}'}{{q_0}'}) {q_0}' ds \\ &=: \int \tilde{L}(q_0, q_0', q_1, q_1') ds.\end{aligned}$$

Here, we seek the Hamiltonian associated with the Lagrangian $\tilde{L}$. The canonical momenta p_0' and p_1' are introduced by

$$p_0' = \frac{\partial \tilde{L}}{\partial q_0'} = -\frac{\partial L}{\partial \dot{q}_1} \dot{q}_1 + L = -\frac{\partial L}{\partial \dot{q}} \dot{q} + L = -H, \tag{2.18}$$

$$p_1' = \frac{\partial \tilde{L}}{\partial q_1'} = \frac{q_0'}{q_0'} \frac{\partial L}{\partial q_1} = \frac{\partial L}{\partial q}. \tag{2.19}$$

In this case, the Hamiltonian $\tilde{H}$ becomes:

$$\tilde{H} = q_0' p_0' + q_1' p_1' - \tilde{L} = (-H + \dot{q} p - L) q_0' = 0. \tag{2.20}$$

Therefore, the Hamiltonian related to the extended phase space becomes zero. The kicked rotor system employed in this thesis is a one-dimensional system subjected to a periodic external force.

2.2 Properties of non-integrable systems and invariant sets

The behavior of non-integrable systems is highly complex, but studying the invariant sets greatly helps our understanding. The invariant sets include periodic orbits, stable and unstable manifolds, among others. In the following, we explain signaures of non-integrable systems by particularly focusing on the invariant sets.

2.2.1 Kicked rotor system

Here, we consider the so-called kicked rotor system. The form of the Hamiltonian is given by

$$H(p,q,t) = T(p) + V(q)\tau \sum_{n\in\mathbb{Z}} \delta(t - n\tau). \tag{2.21}$$

Here the mass is set to $m = 1$ for simplicity, and the period of the instantaneous kick is given by τ. As mentioned above, the 1-dimesional system subjected to a periodic external driving force can be regarded as a 1.5-degree-of-freedom system. In paricular, the kicked roter system is one of the paradigm model systems, exhibiting chaotic behaviors [33]. Below, we consider the case with the kinetic term $T(p) = p^2/2$. The canonical equations of motion of the kicked rotor system is written as

$$\frac{dq}{dt} = \frac{\partial H}{\partial p} = p, \tag{2.22}$$

$$\frac{dp}{dt} = -\frac{\partial H}{\partial q} = -\frac{\partial V(q)}{\partial q} \sum_{n\in\mathbb{Z}} \tau\delta(t - n\tau). \tag{2.23}$$

By integrating the set of equations from $t = n\tau - \varepsilon$ to $(n+1)\tau - \varepsilon$, where n denotes an integer and $0 < \varepsilon < \tau$, we obtain a stroboscopic map, which is nothing but the Poincare map in this situation, as

$$f : \begin{pmatrix} q_{n+1} \\ p_{n+1} \end{pmatrix} = \begin{pmatrix} q_n + \tau p_{n+1} \\ p_n - \tau \frac{\partial V(q)}{\partial q} \big|_{q=q_n} \end{pmatrix}. \tag{2.24}$$

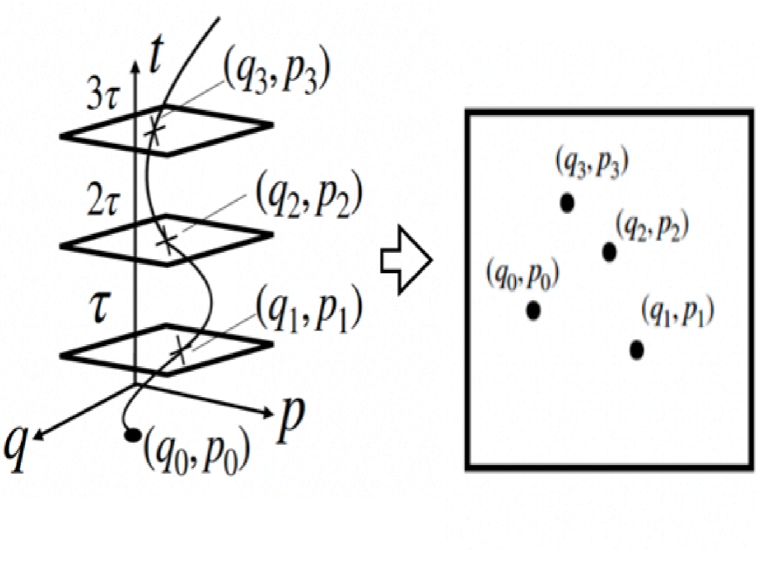

Figure 2.1: Schematic diagram of Poincaré section of the kicked rotor system (2.21) [32].

where (q_n, p_n) denotes the value of (q, p) just after each kick. Figure 2.2 plots examples of the Poincare section (see Fig. 2.1) for the case with $V(q) = k\cos q$ and $\tau = 1$, where k stands for the perturbation strength, respectively. Periodic boundary conditions both in the q and p directions are imposed.

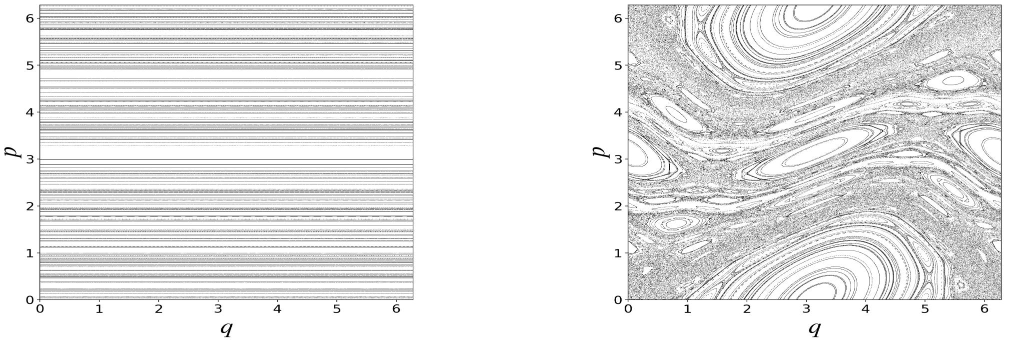

(a) $k = 0$ (b) $k = 1.0$

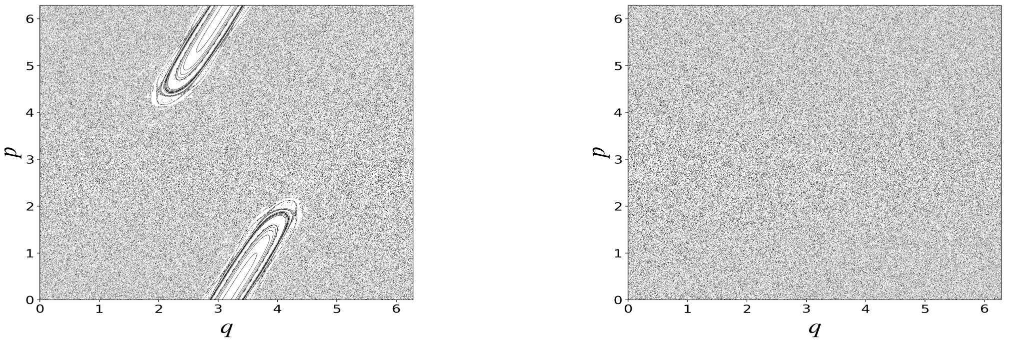

(c) $k = 4.0$ (d) $k = 10.0$

Figure 2.2: Poincaré section of the standard map.

When k is small, quasi-periodic orbits and chaotic orbits intricately intermingle in the phase space. This kind of system is called a *mixed phase space system.* As k increases, chaotic regions gradually grow, eventually filling the entire phase space.

2.2.2 Stability analysis around fixed points

In this section, we discuss the stability of the fixed point (or the periodic orbits) in the map. For the area-preserving map $f : \mathbb{R}^2 \to \mathbb{R}^2$, where $\det Df(x) = 1$ is satisfied, the type of fixed points is classified based on the eigenvalues of the Jacobian matrix $\det Df(\boldsymbol{x})$ at the fixed point (or the periodic orbits) of the map [34]:

- Elliptic (stable) fixed points (all eigenvalues are $|\lambda| = 1$ and $\lambda \neq \pm 1$)
- Parabolic fixed points (all eigenvalues are 1 or all eigenvalues are -1)
- Hyperbolic (saddle) fixed points (all eigenvalues are $|\lambda| \neq 1$)

Now, consider a hyperbolic fixed point. Let E_s and E_u be the stable and unstable vector spaces of the Jacobian matrix $Df(\boldsymbol{x})$ at the hyperbolic fixed point $\mathfrak{p}$. If we denote the vectors spanning

E_s and E_u by $\mathbf{v}_s$ and $\mathbf{v}_u$, respectively, any trajectory close to the fixed point or the periodic orbit asymptotically approaches one of these. There always exists an orbit asymptotically approaching a hyperbolic periodic orbit. Similarly, there exist such orbits for the inverse map as well. These are called the stable manifold $W^s(\mathfrak{p})$ and unstable manifold $W^u(\mathfrak{p})$, defined as follows:

$$W^s(\mathfrak{p}) = \{\boldsymbol{x} \in \mathbb{R}^2 \mid f^{(k)}(\boldsymbol{x}) \to \mathfrak{p} \text{ as } k \to \infty\}, \tag{2.25}$$

$$W^u(\mathfrak{p}) = \{\boldsymbol{x} \in \mathbb{R}^2 \mid f^{(k)}(\boldsymbol{x}) \to \mathfrak{p} \text{ as } k \to -\infty\}. \tag{2.26}$$

In the integrable system, stable and unstable manifolds coincide with each other to form the separatrix. When perturbing the system, the degeneration of the stable and unstable manifolds on the separatrix is resolved. We define homoclinic points as follow:

$$\{\boldsymbol{x} \in \mathbb{R}^2 \mid \lim_{k \to \pm\infty} f^{(k)}(\boldsymbol{x}) = \mathfrak{p} \;\; i.e. \;\; \boldsymbol{x} \in W^u(\mathfrak{p}) \cap W^s(\mathfrak{p})\}. \tag{2.27}$$

Figure 2.3(a) schematically shows the behavior of homoclinic orbits when a perturbation is applied. As is seen, the unstable and stable manifolds in Fig. 2.3(b) create intricate intersections. These intersections of stable and unstable manifolds are called homoclinic intersections, and the points of intersection are referred to as homoclinic points.

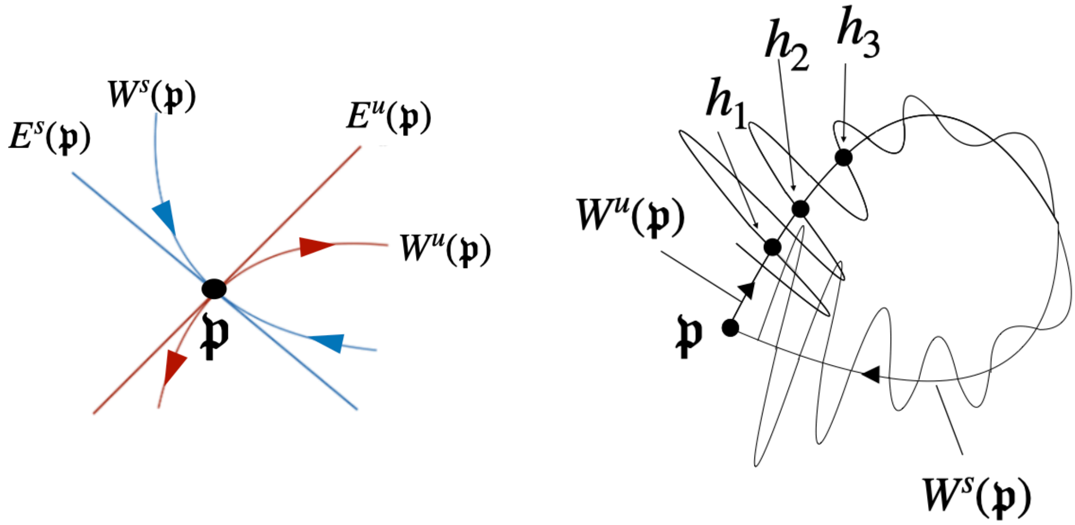

Figure 2.3: (a) Schematic diagram of stable manifold and unstable manifolds associated with a periodic point $\mathfrak{p}$. (b) Schematic diagram of homoclinic orbits. h_1, h_2, and h_3 represent homoclinic points.

From the definition of homoclinic points, forward and inverse map belong to the set $W^s(\mathfrak{p}) \cap W^u(\mathfrak{p})$, and they become homoclinic points as well. Therefore, the existence of a single homoclinic point immediately implies an infinite number of homoclinic points. As the magnitude of the perturbation increases, the number of homoclinic points generally increases, and the region of phase space occupied by the homoclinic points becomes larger, leading to the development of chaotic regions. The intersections of stable and unstable manifolds, as described above, are the origin of chaos [35]. The properties of the stable and unstable manifolds governing chaos are greatly influenced by the local properties of the nearby periodic points. Therefore, stability analysis related to periodic orbits is crucial in understanding the properties of dynamical systems.

2.2.3 Near-integrable systems and KAM tori

In this section, we explain how the mixed system in which the regular and chaotic orbits coexist in the phase space in nearly integrable systems. In the case of nearly integrable systems, the phase space is a mixture of quasi-periodic orbits and chaotic orbits. The following theorem due to Kolmogorov-Arnold-Moser (KAM) is fundamental:

Theorem (KAM [29, 31, 36])**.** *Consider the N-degree-of-freedom Hamiltonian in the following form:*

$$H(\boldsymbol{I},\boldsymbol{\theta},\varepsilon) = H_0(\boldsymbol{I}) + \varepsilon H_1(\boldsymbol{I},\boldsymbol{\theta}), \tag{2.28}$$

where $\varepsilon > 0$*. Consider the domain* $D \subset \mathbb{R}^N$*. At the point* $\boldsymbol{c} = (\boldsymbol{I},\boldsymbol{\theta}) \in D \times \mathbb{R}^N$ *in the phase space, we assume that the following non-degeneracy condition holds:*

$$\det \frac{\partial \boldsymbol{\omega}(\boldsymbol{c})}{\partial \boldsymbol{I}} \neq 0 \ \left(\boldsymbol{\omega} = \frac{\partial H_0}{\partial \boldsymbol{I}}\right). \tag{2.29}$$

ω *satisfies the Diophantine condiiton:*

$$|\boldsymbol{k}\cdot\boldsymbol{\omega}| > C/|\boldsymbol{k}^{\alpha}|, \tag{2.30}$$

where C *and* $\alpha > M (M \in \mathbb{R})$ *are positive constants, and* $\boldsymbol{k} = (k_1,\ldots,k_N)$ *represents arbitrary integer vector. In this case, in the vicinity of the invariant torus* $\boldsymbol{I} = \boldsymbol{c}$ *under the Hamiltonian vector field* X_{H_0}*, there exists an invariant N-dimensional torus under the Hamiltonian vector field* X_H *if* ε *is sufficiently small. In addition, the orbits on this torus move with the frequency vector* $\boldsymbol{\omega}(\boldsymbol{c})$*. This torus is called KAM torus. Moreover, the orbits on each KAM torus densely fill the KAM torus.*

The irrational numbers satisfying the Diophantine condition are slow to be approximated by the continuous fractional expansion. The KAM theorem claims that the quasi-periodic orbits whose frequencies are the irrational numbers satisfying the Diophantine condition are robust to the perturbation and can survive if the strength of the perturbation is weak enough.

Magnifying the region around the KAM tori, we can find island-shaped stable regions appearing [32]. Chaotic regions are extensively fragmented by countless KAM tori. In systems with such complex structures in phase space, compared to hyperbolic dynamical systems, there are fewer mathematical tools available. This is one of the reasons why Hamiltonian systems of nearly integrable nearly integrable Hamiltonian systems are difficult to handle.

2.3 Energy barriers and dynamical barriers

Quantum tunneling in 1-dimension always occurs as a transition over the energy barrier. In contrast, as explained in Introduction, dynamical tunneling is a phenomenon that occurs in phase space and appears in multi-dimensional and non-integrable systems. In non-integrable systems, even in the case where the transition is allowed energetically, it happens that the classical orbits are confined in finite regions. This is because the phase space is decomposed into (infinitely many) invariant components and the orbits are trapped by each invariant component. KAM curves are a typical example of invariant sets, and they play the role of barriers to each other.

To be more explicit, let us consider the double-well Hamiltonian with a one-dimensional double well potential first. For instance, consider a one-dimensional system with the following Hamiltonian:

$$H(q,p) = \frac{1}{2}p^2 + V(q), \tag{2.31}$$

where,

$$V(q) = (q^2 - a^2)^2. \tag{2.32}$$

Here, the potential function $V(q)$ has a local maximum at $q = 0$, and the energy barrier is formed around the local maximum. If the energy of a particle on either side of the potential well is less than the local maximum, the particle cannot move to the other side. In this sense, the barrier blocking the transition of classical particle is only formed by the potential function. We next consider a two-dimensional Hamiltonian with a double well potential [37],

$$H(q_1,q_2,p_1,p_2) = \frac{1}{2}(p_1^2 + p_2^2) + V(q_1,q_2). \tag{2.33}$$

The potential function is given by

$$V(q_1,q_2) = (q_1^2 - 1)^2 + q_2^2 + \varepsilon q_1^2 q_2^2. \tag{2.34}$$

For $\varepsilon = 0$, the Hamiltonian is separable, therefore the system is trivially integrable. On the other hand, for $\varepsilon \neq 0$, it becomes non-integrable. In Fig. 2.4, we illustrate the behavior the classical orbits whose initial energy is larger than the height of the potential barrier. In Fig. 2.4(a), the red and blue curves are the classical orbits confined in KAM tori located on either side of the potential well, whereas Fig. 2.4(b) plots a chaotic orbit wandering over both wells. The aspect of the coexistence of regular and chaotic orbits in the phase space is displayed in Fig. 2.4(c). Here, we take $q_2 = 0$ as Poincaré section Σ for this system and plot the points on Σ only when the orbits cross Σ with $p_2 > 0$. In this way, due to the presence of KAM tori, the orbits cannot move to the other side of the well even though the energy of the orbit is above the saddle point of the potential function. As can be seen, KAM tori act as barriers as the energy barrier in the one-dimensional double well system does so. Here such a kind of dynamically formed barrier is referred to as the dynamical barrier.

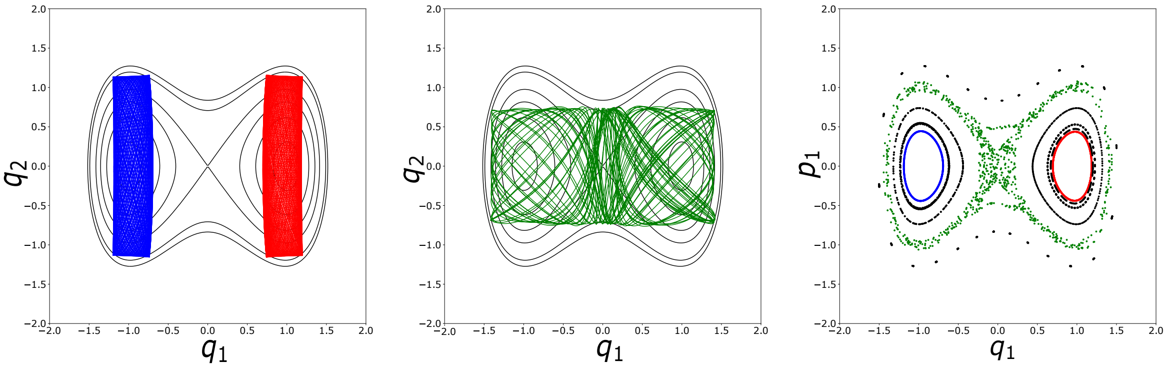

(a)

(b)

(c)

Figure 2.4: (a) and (b) The colored trajectories represent projections onto the (q_1, q_2) plane with different initial conditions for $E = 1.5$. indicate the equi-energy potential curves (2.34) (c) shows the behavior of the trajectories on the Poincaré section $\Sigma = \{(q_1, p_1) \mid (q_1, q_2, p_1, p_2) \in \mathbb{R}^4\}$.

Chapter 3

Quantum tunneling in non-integrable systems and semiclassical theory

In this chapter, we discuss the difference between integrable and non-integrable systems in terms of tunneling splitting, a manifestation of the tunneling effect. After a brief introduction to the semiclassical treatment of tunneling splitting in integrable systems, the results of previous studies of non-integrable systems are presented. tunneling splitting in integrable systems shows an exponential and monotonic decay with respect to Planck's constant, while a staircase structure appears in non-integrable systems [10, 11, 12, 13, 14, 15, 16, 17].

In order to explain why such a difference appears, we have to develop a semiclassical analysis, which is known to be a promising method to specify the manifestation of classical chaos in quantum phenomena [38]. We then formulate the time-domain semiclassical theory for discrete mapping systems, which is the main analytical tool of this thesis. Since chaos appears in the complex domain for non-integrable systems, the number of complex orbits contributing to the semiclassical propagator increases exponentially with time, but they do not have equal weights in their magnitude. Thus, the selection of orbits from the potentially contributing orbits becomes a central problem in the semiclassical analysis using the complex orbits.

3.1 tunneling effect in integrable systems

In this section, we introduce the semiclassical approach to quantum tunneling in integrable systems.

3.1.1 WKB method

Here, we review the WKB method by taking the following one-dimensional time-independent Schrödinger equation [39, 40],

$$\hat{H}\psi(q) = \left(-\frac{\hbar^2}{2}\Delta + V(\hat{q})\right)\psi(q). \tag{3.1}$$

Let us assume the wave function in the following form,

$$\psi(q) = A\exp\left(\frac{\mathrm{i}}{\hbar}S\right), \tag{3.2}$$

where S represents the action. Expanding S with respect to $\hbar$, we have

$$S = S_0 + \frac{\hbar}{\mathrm{i}}S_1 + \left(\frac{\hbar}{\mathrm{i}}\right)^2 S_2 + \cdots . \tag{3.3}$$

Substituting (3.2) with the expansion (3.3) into Eq. (3.1), we obtain the relation,

$$\frac{S'^2}{2} - \frac{i\hbar S''}{2} = E - V(q). \tag{3.4}$$

The 0th and 1st order terms in $\hbar$ respectively lead to

$$\frac{S_0'^2}{2} = E - V(q), \quad S_0 S_1' + S_0''/2 = 0. \tag{3.5}$$

Solving these differential equations, we obtain,

$$S_0 = \pm\int \sqrt{2(E - V(q))}dq = \pm\int pdq, \quad S_1 = \ln p. \tag{3.6}$$

Here, $\sqrt{2(E-V(q))}$ represents the classical momentum p, and $\int pdq$ is the generating function $G(q,E)$ for the canonical transformation from the coordinates $(q,p) \mapsto (E,\theta)$, where θ is a pair of canonical conjugate variables of E. Suppose that the energy E of the particle satsfies $E > V(q)$ for $q < q^t$ and $E \leq V(q)$ for $q \geq q^t$, then the WKB wave function at a position $q \geq q^t$ is expressed as,

$$\psi(q) \simeq \frac{C_1}{\sqrt{|p|}}\exp\left(-\frac{1}{\hbar}\left|\int_{q^t}^{q} pdq\right|\right), \tag{3.7}$$

where C_1 is a normalization constant.

Consider the energy splitting of a double well potential Eq. (2.32). The following discussion is based on [39]. Here we assume the situation where the ground and the first excited state energies, E_0^+, E_0^-, are nearly degenerated and they form a doublet. If we denote the wave functions corresponding to these two levels by ψ_0^+ and ψ_0^-, respectively. Due to the symmetry of the potential, we find that

$$\begin{aligned}
\psi_0^+(q) &\simeq \frac{1}{\sqrt{2}}(\psi_0(q) + \psi_0(-q)), \\
\psi_0^-(q) &\simeq \frac{1}{\sqrt{2}}(\psi_0(q) - \psi_0(-q)),
\end{aligned}$$

$\psi_0(q)$ represents the local WKB state. Consider the continuity and differentiability conditions at the point $q = 0$,

$$\psi_0^+(0) = \sqrt{2}\psi_0(0), \ \ \psi_0^-(0) = 0, \ \ \psi_0^{+\prime}(0) = 0, \ \ \psi_0^{-\prime}(0) = \sqrt{2}\psi_0'(0). \tag{3.8}$$

Here, we consider the normalization condition,

$$\int_0^\infty \psi_0(q)\psi^\pm(q)dq \approx \int_0^\infty |\psi_0(q)|^2 dq = 1/\sqrt{2}. \tag{3.9}$$

Schrodinger's equations for ψ_0 and $\psi_0^\pm$ are

$$\left(-\frac{\hbar^2}{2}\frac{d^2}{dq^2} + V(q)\right)\psi_0(q) = E_0\psi_0(q), \tag{3.10}$$

$$\left(-\frac{\hbar^2}{2}\frac{d^2}{dq^2} + V(q)\right)\psi_0^\pm(q) = E_0^\pm\psi_0^\pm(q). \tag{3.11}$$

Multiplying the two equations above yields,

$$\frac{2}{\hbar^2}(E_0^\pm - E_0)\psi_0(q)\psi^\pm(q) = \psi_0(q)\psi_0^{\pm\prime\prime}(q) - \psi_0^\pm(q)\psi_0''(q). \tag{3.12}$$

Integrating both sides of this equation from 0 to ∞, we obtain,

$$\begin{aligned}\frac{\sqrt{2}}{\hbar^2}(E_0^\pm - E_0) &= \int_0^\infty (\psi_0(q)\psi_0^{\pm\prime\prime}(q) - \psi_0^\pm(q)\psi_0''(q))dq \\ &= [\psi_0\psi_0^{\pm\prime} - \psi_0^\pm\psi_0']_0^\infty - \int_0^\infty (\psi_0'(q)\psi_0^{\pm\prime}(q) - \psi_0^{\pm\prime}(q)\psi_0'(q))dq. \end{aligned}\tag{3.13}$$

From Eq. (3.8), we have

$$E_0^+ - E_0 = -\hbar^2\psi_0(0)\psi_0'(0), \tag{3.14}$$

$$E_0^- - E_0 = \hbar^2\psi_0'(0)\psi_0(0), \tag{3.15}$$

and we obtain the following equation

$$\Delta E := E_0^- - E_0^+ \simeq 2\hbar^2\psi_0'(0)\psi_0(0). \tag{3.16}$$

The eigenfunction and its derivative in the classical forbidden region is evaluated semiclassically as (3.7). Using Eq. (3.7) and (3.16), the tunneling splitting is semiclassically expressed as

$$\Delta E \approx A\exp\left(-\frac{S}{\hbar}\right), \tag{3.17}$$

where the amplitude factor A and the classical action S are respectively given as

$$A = \frac{\omega\hbar}{\pi}, \quad S = \int_{-q^{\mathrm{t}}}^{q^{\mathrm{t}}} |p(q)|dq. \tag{3.18}$$

Here, $\omega := \frac{2\pi}{T}$, where T represents the period of classical orbit on the energy surface E_0.

3.2 tunneling effect in non-integrable system

As mentioned in 2.1.2, systems with more than two degrees of freedom are generally non-integrable systems. We can expect that the quantum tunneling reflects the non-integrability of the system, even though it is a purely quantum phenomenon. In this section, we present previous studies on tunneling effects in non-integrable systems, especially focusing on the nature of tunneling splittings as discussed before for the integrable system.

In this section, we will discuss the quantum tunneling effect in non-integrable systems. First, using a double well potential, and then considering the quantum tunneling effect using the kicked rotor system discussed in 2.2.1.

In integrable systems, the tunneling tail exhibits exponential decay. However, in non-integrable systems, the behavior of the tunneling tail is entirely different. This phenomenon becomes evident by observing tunneling splitting vs $1/\hbar$-plot [41]. In the following, quantum calculations are performed to observe the increase in tunneling probability. Here, we consider the kicked rotor system.

$$\hat{H} = \frac{\hat{p}^2}{2} + V(\hat{q})\tau \sum_n \delta(t - n\tau). \tag{3.19}$$

Here we consider the case with $V(\hat{q}) = -k\cos(2\hat{q})$ in Ref. [42]. The Poincaré section for this map is illustrated in Figs. 3.1.

In the following, let $T(\hat{p}) = \hat{p}^2/2$. The time evolution of the quantum map is given by the unitary operator

$$\hat{U} = \exp\left(-\frac{\mathrm{i}}{\hbar}V(\hat{q})\tau\right)\exp\left(-\frac{\mathrm{i}}{\hbar}T(\hat{p})\tau\right). \tag{3.20}$$

Let u_k be the eigenvalue of the unitary operator $\hat{U}$, and let $|\Psi_k\rangle$ be the corresponding eigenvector. From the Floquet theory [43], the following solution exists.

$$\hat{U}\,|\Psi_k\rangle = u_k\,|\Psi_k\rangle \tag{3.21}$$

where $u_k = \exp\left(-\mathrm{i}\frac{E_k}{\hbar}\tau\right)$. Here, $|\Psi_k\rangle$ and E_k are referred to as quasi-eigenstates and quasi-eigenenergies, respectively.

Since the potential function is symmetric with respect to the origin $q = 0$, the grand state $|\Psi_0\rangle$ and the first exited state $|\Psi_1\rangle$ form a double, and the associated quasi-energies E_0 and E_1 are nearly degenerate, leading to a tunneling splitting $\Delta E := |E_1 - E_0|$. As mentioned above, the tunneling splitting measures the magnitude of tunneling between two wells. In Fig. 3.2, we compare the tunneling splittings obtained for the situation almost close to the integrable limit with the non-integrable system. As predicted, the tunneling splitting for the former case shows a simple exponential dependence, while that for the non-integrable parameter case exhibits a staircase profile accompanied by a series of spiky peaks. The origin for the non-monotonic behavior found in non-integrable systems has closely been analyzed in [42, 44]. The signatures of tunneling in non-integrable systems are so different from those in integrable systems. Such a sharp contrast of tunneling splittings is well recognized on a phenomenological level, but a semiclassical understanding for such characteristic profile is still lacking.

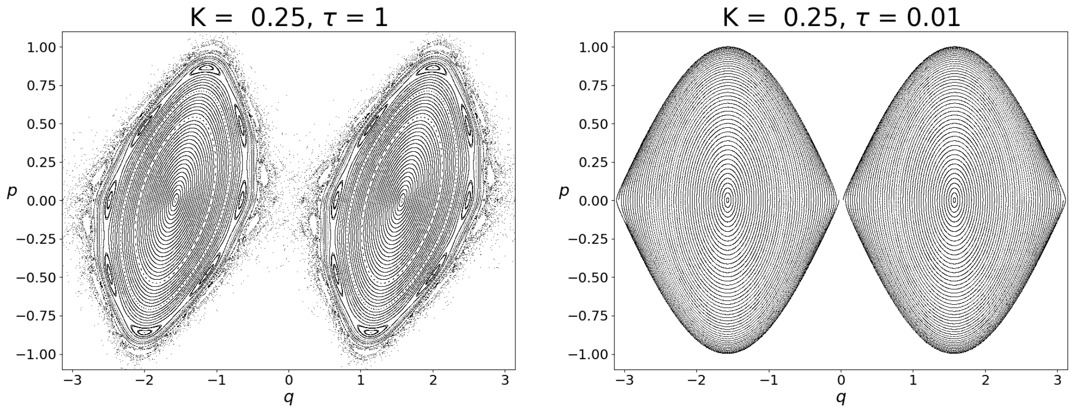

(a) (b)

Figure 3.1: The phase space for $k = 0.25$ of the map (2.24) with $V(q) = \cos(2q)$. (a) shows $\tau = 1$. Figure (b) shows the case $\tau = 0.01$.

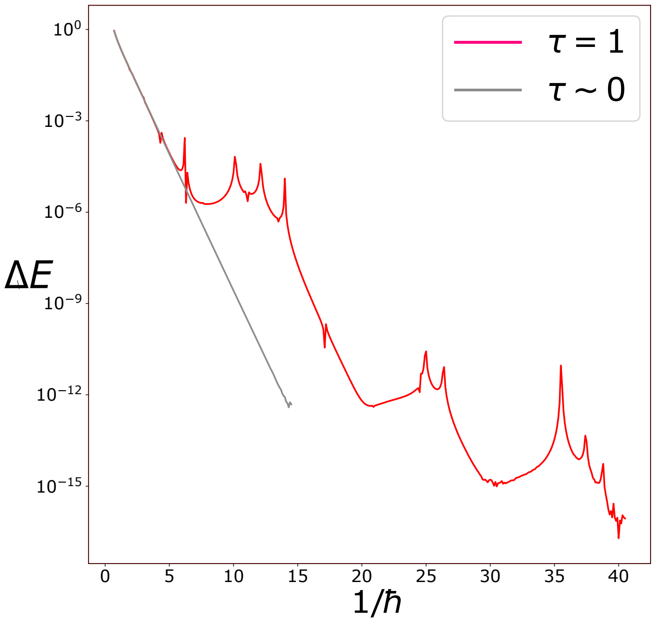

(a)

Figure 3.2: (a) tunneling splitting ΔE vs $1/\hbar$. The red curve corresponds to the case $\tau = 1$, while the gray curve represents the case with $\tau \simeq 0$.

3.3 Complex semiclassical theory and tunneling effects

Since quantum tunneling is a purely quantum phenomenon, we cannot find a counterpart in classical mechanics as it stands. However, as shown in section 4.3, it is possible to describe a purely quantum phenomenon by extending classical dynamics to the complex plane. Technically, this could be done by applying semiclassical theory, which is an approximation of quantum mechanics in terms of classical mechanics.

3.3.1 Semiclassical theory in the energy and time domains

As classical quantizations, quasi-periodic orbits appear at most in the phase space for integrable systems, one can apply the Bohr-Sommerfeld quantization condition for one-dimensional systems and the Einstein-Brillouin-Keller quantization for multi-dimensional integrable systems [2]. On the other hand, for non-integrable systems, the orbits in the phase space are very complex, and it is difficult to develop classical quantization condition in the same way as in integrable systems. In strongly chaotic systems, the Gutzwiller trace formula connects the eigenvalue sequence of the quantum systems to the set of the periodic orbits in the corresponding classical systems [45, 46]. However, even in strongly chaotic systems, one can at most find the sequence of eigenvalues, and have no way to access individual eigenfunctions within semiclassical theory. The situation is even worse in mixed systems where regular and chaotic regions coexist in a single phase space: one cannot provide the semiclassical formula not only for eigenfunctions but also for eigenvalues. What one can do is to develop the semiclassical analysis in the time domain.

3.3.2 Semiclassical propagator

Below, we introduce a formulation in the semiclassical analysis in the time domain. To do this end a semiclassical propagator is derived by applying the stationary or saddle-point approximation to the fully quantum propagator. In this section, we proceed with the kicked rotor system, which was also used in the previous chapter. We will first explain the discrete-time path integral, and then perform a stationary or saddle-point approximation for the propagator to derive the semiclassical propagator. Here, let us assume that the Hamiltonian for the quantum system is given as (3.19), With a perturbation parameter τ, let $\hat{U}$ be the time-evolution operator (3.20), and $|\psi_n\rangle$ be the wave function of the system at time $n\tau$. The quantum propagator in the discrete path integral form is

$$\langle q|\hat{U}^n|q_0\rangle = \int \cdots \int dq_1 dq_2 \cdots dq_{n-1} \langle q|\hat{U}|q_{n-1}\rangle \cdots \langle q_1|\hat{U}|q_0\rangle . \tag{3.22}$$

where $(q,p) := (q_n, p_n)$. Inserting the complete set for momentums we find that,

$$\begin{aligned}
\langle q|\hat{U}^n|q_0\rangle &= \int dq_1 \cdots dq_{n-1} \int dp_1 \cdots dp_{n-1} \\
&\times \prod_{j=0}^{n-1} \langle q_{j+1}| e^{-\frac{\mathrm{i}}{\hbar}T(p_{j+1})\tau} |p_{j+1}\rangle \langle p_{j+1}| e^{-\frac{\mathrm{i}}{\hbar}V(q_j)\tau} |q_j\rangle \\
&= \left(\frac{1}{2\pi\hbar}\right)^n \int \prod_{j=0}^{n-1} dq_j dp_j \\
&\times \exp\left[\frac{\mathrm{i}}{\hbar}\sum_{j=0}^{n-1}\left\{(q_{j+1}-q_j)p_{j+1}/\tau - T(p_{j+1}) - V(q_j)\right\}\tau\right] \\
&= \left(\frac{1}{2\pi\hbar}\right)^n \int \prod_{j=0}^{n-1} dq_j dp_j \exp\left(\mathrm{i}\frac{S_n(q_0,q)}{\hbar}\right), \qquad (3.23)
\end{aligned}$$

where,

$$S_n(q_0,q) = \sum_{j=0}^{n-1}\left[(q_{j+1}-q_j)p_{j+1}/\tau - T(p_{j+1}) - V(q_j)\right]\tau. \qquad (3.24)$$

The stationary or saddle-point approximation yields the following expression [47]:

$$\langle q|\hat{U}^n|q_0\rangle \simeq \sum_{\gamma} A_n^{(\gamma)}(q_0,q) \exp\left\{\frac{\mathrm{i}}{\hbar}S_n^{(\gamma)}(q_0,q) + \mathrm{i}\frac{\pi}{2}\mu^{(\gamma)}\right\}, \qquad (3.25)$$

where $A_n^{(\gamma)}(q_0,q) = \sqrt{\left|\det \frac{\partial^2 S_n^{(\gamma)}}{\partial q_n \partial q_0}\right|}$, $S_n^{(\gamma)}(q_0,q)$ and $\mu^{(\gamma)}$ denote the amplitude factor associated with the stability of each orbit γ, the corresponding classical action, and the Maslov index, respectively. The semiclassical propagator is evaluated by summing over all possible classical orbits γ which start with $q_0 = \alpha$ and end up with $q = \beta$. Note that initial and final momenta α and β should be real-valued since they are observables.

3.3.3 Time-domain complex semiclassical theory

As previously stated, the transition between different KAM tori is forbidden in the real domain. Therefore, if we apply the semiclassical theory for describing tunneling effects, it is inevitable to extend semiclassical theory to the complex plane. In integrable systems, the instanton orbit is the only complex path that describe tunneling effects, and the transition occurs only between the states with the same energies.

On the other hand, in non-integrable systems, instanton orbits are fragmented by chaos in the complex domain. Moreover, due to chaos in the complex domain, multiple complex orbits could contribute to semiclassical propagator [19, 20]. This is one of the major difficulties of time-domain semiclassical theory [19, 20].

However, the contributions of these orbits to the propagator are not equally weighted, and their magnitudes strongly depend on the nature of the orbits. The governing factor of the contribution is the imaginary action Im S along the orbits [19]. Since the imaginary action appears in the exponent of each contribution, the orbits with larger imaginary actions have negligible weights compared to those with smaller imaginary actions [19, 20, 48]. Therefore, our task is to find the complex path(s) with the minimal imaginary action out of the candidates complex paths satisfying the boundary conditions. This will be the main issue in the subsequent sections. The magnitude of the imaginary action must reflect the behavior of the orbits in the complex plane.

In the next chapter we review recent results on complex dynamical systems in two dimensions. Based on these, an important statement about the candidates of complex orbits that contribute to the semiclassical propagator is obtained.

Chapter 4

Complex dynamics and tunneling effect

As mentioned in the previous section, in evaluating the semiclassical propagtor for non-integrable systems, an infinite number of complex orbits many complex orbits could appear in the sum. The aim of this chapter is to give a fundamental result of the theory of complex dynamical systems, which will be used in the semiclassical analysis of quantum tunneling in non-integrable systems. To this end, we first introduce results on the complex dynamics in two dimension, especially polynomial maps, developed by Bedford and Smillie. For one-dimensional complex dynamics, it is rather easy to see that chaotic behavior appears on the Julia set, which is defined as the boundary between bounded and escaping orbits in the complex plane. On the other hand, in multi-dimensional complex dynamics, the techniques used to analyze one-dimensional complex dynamics cannot straightforwardly be applied. Instead, the so-called potential theoretic approach becomes a powerful tool and is used to study asymptotic behaviors of the dynamics [23, 24, 25, 26]. An important result of Bedford and Smillie is that the dynamics is mixing and thus ergodic independent of the dynamics in the real plane. In other words, orbits in the complex plane can reach arbitrary regions of phase space, even though the real classical phase space is disjointed into separate invariant components. Ergodicity in the complex plane will be a key property when one develops the semiclassical theory of tunneling in non-integrable systems. The explanation of complex dynamical systems in this chapter is based on [49].

4.1 One-dimensional complex dynamical systems

As a preparation for dealing with two variables complex dynamical systems, we first present the results for one-dimensional polynomial complex dynamical systems [50, 51]. The main focus of this section is the classification of orbits in one dimensional maps. The Fatou set consists of orbits that behave regularly, while the orbits in the Julia set, which is the complement of the Fatou set, exhibit chaotic behaviors. Here, for simplicity, we consider a class of polynomial maps in one dimension:

$$P(z) := z^d + a_1 z^{d-1} + \cdots + a_d \quad (d \geq 2).$$

We classify the types of orbits according to their behavior in the limit of time going to infinity:

$$I := \{z \in \mathbb{C} \mid \lim_{k\to\infty} |P^{(k)}(z)| \to \infty\}, \tag{4.1}$$

$$K := \{z \in \mathbb{C} \mid \lim_{k\to\infty} |P^{(k)}(z)| < \infty\}. \tag{4.2}$$

where I and K are called the set of escaping points and the filled Julia set of P, respectively. The Julia set is defined as the boundary of the filled Julia set K,

$$J := \partial K. \tag{4.3}$$

Additionally, the Fatou set is defined as:

$$F := \overline{\mathbb{C}} \backslash J \ \ (\overline{\mathbb{C}} := \mathbb{C} \cup \{\infty\}). \tag{4.4}$$

The orbits on the Fatou set, the complement of the Julia set, are either stable periodic orbits or sets of orbits that diverge to infinity. Thus, orbits on the Fatou set move monotonically and so they show regular behaviors.

An example of a one-dimensional complex dynamical system that exhibits non-trivial behavior is the following map P [49]:

$$P : z \mapsto z^2. \tag{4.5}$$

For this map, we can easily find that $I = \{|z| > 1\}$, $K = \{|z| < 1\}$, and $J = \{|z| = 1\}$. It is also easy to confirm that the orbits in the Julia set J satisfy the definition of chaos in the sense of Devaney [52]: (i) the density of periodic orbits, (ii) topological transitivity, and (iii) sensitivity to initial conditions.

4.1.1 Potential theory for one dimensional complex dynamical systems

We will examine the properties of the Julia set based on subharmonic potential theory [53]. First, the behavior of the dynamical system around $z = \infty$ will be explained.

Theorem 1 (Böttcher's Theorem [54])**.** *For a sufficiently large positive $R \in \mathbb{R}$, there exists a function defined in the region $V = |z| > R$ in the following form:*

$$\varphi(z) = z + b_0 + \frac{b_1}{z} + \cdots, \quad (b_i \in \mathbb{C} \ \ (i = 0, 1, \ldots)) \tag{4.6}$$

and satisfies,

$$\varphi(P(z)) = (\varphi(z))^d, \ (d \in \mathbb{N}, \ d \geq 2). \tag{4.7}$$

This function $\varphi(z)$ is called the Böttcher function. We then define the Green function as,

$$G(z) := \log|\varphi(z)|. \tag{4.8}$$

Since the Green function $G(z)$ is defined using the Böttcher function, it is defined around $z = \infty$. This Green function $G(z)$ can be explicitly written as follows:

$$G(z) := \lim_{n\to\infty} \frac{1}{d^n} \log^+ |P^n(z)|, \tag{4.9}$$

where $\log^+ t = \max\{0, \log t\}$. Here, $G(z)$ is also defined around $z = \infty$. Here, we discuss the properties of subharmonic and harmonic functions. A harmonic function is defined as a function Θ such that $\Delta\Theta(z) = 0$. Subharmonic functions are known as a class of functions that weaken the conditions of harmonic functions. We now explain subharmonic functions in $\mathbb{C}$ [53, 55]. A sub-harmonic function is a function $u(z)$ with the following properties. Let $U \in \mathbb{C}$ and $u : U \to \mathbb{R}$, and suppose that

1. $u(z)$ is an upper semi-continuous function.
2. Consider a disk $D \subset U$. For any harmonic function $h : D \to \mathbb{R}$ that satisfies $u = h$ on ∂D, it holds that $u(z) \leq h(z)$ on D.

If u is a subharmonic function, the following condition is satisfied for any arbitrary $z_0 \in \mathbb{C}$

$$u(z_0) \leq \frac{1}{2\pi} \int_0^{2\pi} u(z_0 + re^{i\theta}) d\theta. \quad (r \in \mathbb{R}) \tag{4.10}$$

This implies that the value of $u(z)$ around z_0 is always less than or equal to the function at that point. The equality holds in the case where f is a harmonic function. It is known that subharmonic functions, except for constant functions, satisfy the maximum principle, meaning that they attain their maximum values on the boundary of the set where they are defined. Let us define $\Delta G(z) = 0$ at $z = \infty$. Furthermore, by definition of the Green function, $G(z) = 0$ follows at points other than $z = \infty$. $G(z)$ is shown to be a subharmonic function on $\mathbb{C}$. The Green's function takes values only on the Julia set [49].

4.1.2 Complex equilibrium measure

Consider the following function $\mu(z)$ induced from the Green function $G(z)$,

$$\mu(z) = \frac{1}{2\pi} \Delta G(z). \tag{4.11}$$

Eq. (4.11) is analogous to the Poisson equation in electromagnetism, where $G(z)$ corresponds to the electrostatic potential and $\mu(z)$ to the charge distribution. In the Poisson equation, the potential function is determined by a given charge distribution. On the other hand, in Eq. (4.11), the surface charge distribution $\mu(z)$ is determined by the given potential $G(z)$.

The following Brolin's theorem [56] states that $\mu(z)$ is the complex equilibrium measure and has ergodic properties at the points of the Julia set.

Theorem 2 (Brolin [56]).
1. *For any point $a \in \mathbb{C}$, $\mu_n = \frac{1}{d^n} \sum_{z_0 \in P^{-n}(a)} \delta(z - z_0) \to \mu(z)$ as $n \to \infty$.*
2. $\operatorname{supp} \mu(z) = J$.
3. *μ is preserved under the mapping P and is strongly mixing.*

The statement 1 implies that μ_n converges to μ. The statement 2 indicates that the charge is distributed along the boundary of K. Considering the analogy with electromagnetism, the

Green function $G(z)$ determines the shape of the perfect conductor as K. Similar to the charge distribution on the surface of a perfect conductor, it converges to the boundary of the filled Julia set K. The statement 3 indicates that the orbits on the set J exhibit ergodic behavior. Here, strong mixing is defined in a probability space $(X, \mathscr{B}, \mu)$ as the condition where for any $A, B \in \mathscr{B}$, $\lim_{n\to\infty} \mu(f^{-n}A \cap B) = \mu(A)\mu(B)$ holds. The mixing of μ immediately leads to the ergodicity of the Julia set J.

4.2 Two-dimensional complex dynamical systems

As explained above, in one-dimensional complex dynamics one can see that chaos appears in the Julia set. We now turn our focus toward the complex dynamics in two dimensions. Below, we will introduce some recent results on the two-dimensional complex dynamics obtained by Bedford and Smillie [23, 24, 25, 26]. Their results claim that the Julia set derived based on the potential theoretic arguments has similar properties shown in that in the one dimensional case.

4.2.1 Two-dimensional complex dynamical systems

The Hénon map has originally been introduced to provide a minimal two-dimensional map in the real plane [57]. One of the canonical form of the Hénon map is expressed by

$$\mathscr{H} : \begin{pmatrix} x' \\ y' \end{pmatrix} = \begin{pmatrix} y \\ y^2 - bx + a \end{pmatrix}, \tag{4.12}$$

where a and b denote the nonlinearity parameter and the Jacobian of the map, respectively. According to Friedland-Milnor's theorem, polynomial automorphisms can be classified into (i) elementary map (ii) affine map (iii) Hénon map, and arbitrary two dimensional copmlex polynomial maps can be constructed by combinations of these. Of these three cases (i)-(iii), only the Hénon map generates chaos [58]. Hereafter, we focus on the case with $|b| = 1$, that is the area-preserving case. Note that via the affine transformation $(x, y) = (q-1, p)$, the map (4.12) is reduced to the form of Eq. (2.24) with potential function $V(q) = -\frac{1}{3}q^3 + cq$, where c is a real constant.

The Hénon map system exhibits various behaviors depending on the nonlinear parameter a. For $a \gg 1$, the system satisfies the conditions of a topological horseshoe and becomes conjugate to a symbolic dynamical system [59]. As the parameter a decreases, the horseshoe structure is broken [60]. Below, we discuss results that are independent of the value of parameter a and the map of the real plane is either a mixed or hyperbolic.

Similar to one dimensional complex dynamical systems, two dimensional complex dynamical systems are also distinguished by their behavior as $n \to \infty$. The set $I^{\pm}$ of escaping points and the filled Julia set $K^{\pm}$ are defined as follows [61] as

$$I^{\pm} = \{(x, y) \in \mathbb{C}^2 \mid \lim_{k\to\pm\infty} \|\mathscr{H}^{(k)}(x, y)\| \to \infty\}, \tag{4.13}$$

$$K^{\pm} = \{(x, y) \in \mathbb{C}^2 \mid \lim_{k\to\pm\infty} \|\mathscr{H}^{(k)}(x, y)\| < \infty\}. \tag{4.14}$$

where the norm in $\mathbb{C}^2$ is defined as

$$\|\boldsymbol{x}\| = \sqrt{|x|^2 + |y|^2}, \quad (\boldsymbol{x} = (x, y) \in \mathbb{C}^2). \tag{4.15}$$

The Julia set is similarly defined [61]:

$$J^{\pm} = \partial K^{\pm}, \tag{4.16}$$

$$J = J^{+} \cap J^{-}. \tag{4.17}$$

4.2.2 Bedford-Smillie theorem and ergodicity of complex domain

In this section, we will introduce a couple of key theorems for two-dimensional complex dynamical systems obtained by Bedford and Smillie. The current convergence theorem, which is a central result of their analyses, and the series of theorems derived from it hold not only in the hyperbolic parameter loci but also in non-hyperbolic situations.

In preparation for the Bedford-Smillie theorem, we briefly explain pluri-potential theory in two dimensions. First, we need to introduce currents, which are essential ingredients in discussing pluri-potential theory. Consider the set of (p,q)-forms on a compact support $\Omega \subset \mathbb{C}^2$ [49, 55]:

$$\mathscr{D}^{p,q}(\Omega) := \left\{ \sum_{|I|=p,|J|=q} u_{I,J} dz_{i_1} \wedge \cdots \wedge dz_{i_p} \wedge d\bar{z}_j \wedge \cdots \wedge d\bar{z}_{j_q} \;\middle|\; u_{I,J} \in C^{\infty}(\Omega) \right\}. \tag{4.18}$$

Here, an element φ of $\mathscr{D}^{p,q}(\Omega)$ is called a test form, and $\mathscr{D}^{p,q}(\Omega)$ is the space of test forms, expressing the dual space of test forms as $(\mathscr{D}^{p,q}(\Omega))'$, and an element of $(\mathscr{D}^{p,q}(\Omega))'$ as T:

$$T : \mathscr{D}^{p,q}(\Omega) \to \mathbb{C} \tag{4.19}$$

where T is called a (q,p)-current. Here, we introduce the $(1,1)$-form operator dd^c as follows.

$$dd^c := 2\mathrm{i} \sum_{j,k}^{2} \frac{\partial^2}{\partial z_j \partial \bar{z}_k} dz_j \wedge d\bar{z}_k. \tag{4.20}$$

This is known as the *Monge-Ampère operator* [53, 62], which is an analog of the Laplacian in the one-dimensional case. Similar to the one-dimensional case, we define the Green function $G(x,y)$ for $\mathbb{C}^2$ as follows:

$$G(x,y) := \lim_{n \to \infty} \frac{1}{2^n} \log^{+} ||\mathscr{H}^{\pm n}(x,y)||. \tag{4.21}$$

Since the Hénon map includes the quadratic term y^2, the normalization factor $\frac{1}{2^n}$ is put in the right hand side of (4.21). This Green function belongs to a class of functions known as pluri-subharmonic functions. The definition of pluri-subharmonic function is that the functions on any complex linear curves in $\mathbb{C}^2$ are subharmonic [53]. Corresponding to the Poisson equation (4.11) in one dimensional complex dynamical systems, introduce

$$\mu^{\pm} := \frac{1}{2\pi} dd^c G^{\pm}, \tag{4.22}$$

where $\mu^{\pm}$ represent what are known as positive currents. A current is a differential form with distributions as coefficients. For these $\mu^{\pm}$, Bedford and Smillie proved the following:

Theorem 3 (Bedford-Smille [23])**.**

$$\mathrm{supp}\,\mu^{\pm} = J^{\pm}. \tag{4.23}$$

It is important to note that $\mu^{\pm}$ are not complex equilibrium measures. Therefore, we cannot discuss properties like mixing or ergodicity of Julia sets for $\mu^{\pm}$. Instead, we introduce a $(2,2)$-form given by [53, 63]

$$\mu := \mu^{+} \wedge \mu^{-}. \tag{4.24}$$

It has been shown that this serves as an invariant measure in the Hénon map corresponding to the one-dimensional case. Then, we focus on the support of μ:

$$J^{*} = \mathrm{supp}\mu. \tag{4.25}$$

Here, J^{*} is called the potential theoretic Julia set.

Theorem 4 (Convergence theorem of currents [24])**.** *For any algebraic variety M, there exists a constant $c > 0$ that satisfies the following equation:*

$$\lim_{n\to\infty} \frac{1}{2^n}[\mathscr{H}^{\mp n}M] = c\mu^{\pm}. \tag{4.26}$$

Here, the current of integration is defined as follows. Let $\varphi \in \mathscr{D}^{1,1}(\Omega)$ $(M \subset \Omega \subset \mathbb{C}^2)$, and $\hat{M}$ be a regular point on M. $[M]$ is defined as

$$\int_{\hat{M}} \varphi \circ i, \tag{4.27}$$

where i is the inclusion map $i : \hat{M} \hookrightarrow \mathbb{C}^2$. From current convergence theorem and Eq. (4.23), we can conclude that any manifold iterated by the forward (resp. backward) map tends to the forward (resp. backward) Julia set is guaranteed. Furthermore, the following important theorems are deduced from this current convergence theorem.

Theorem 5 (Bedford-Smillie [23, 24, 25, 26])**.**
1. *For any unstable periodic points $\mathfrak{p}$, $\overline{W^s(\mathfrak{p})} = J^+$ and $\overline{W^u(\mathfrak{p})} = J^-$*
2. *The measure μ is mixing and hyperbolic.*
3. $\overline{\{\text{unstable periodic points}\}} = J^{*}$

Here, the stable and unstable manifolds for a periodic point $\mathfrak{p}$ of period n are defined as:

$$W^s(\mathfrak{p}) = \{\mathfrak{p} \in \mathbb{C}^2 \mid \mathscr{H}^{(nk)}(\mathfrak{p}) \to \mathfrak{p} \;\; (k \to \infty)\}, \tag{4.28}$$
$$W^u(\mathfrak{p}) = \{\mathfrak{p} \in \mathbb{C}^2 \mid \mathscr{H}^{(-nk)}(\mathfrak{p}) \to \mathfrak{p} \;\; (k \to \infty)\}. \tag{4.29}$$

The statements given in Theorem 5 hold regardless of the perturbation parameter a of the Hénon map. Therefore, they can be applied even in the case where mixed phase space is realized. Note that these theorems only hold for uniformly hyperbolic systems when the dynamics are restricted to the real domain. From theorem 5-2, we can deduce that the dynamics can be chaotic in the complex domain due to the topological transitivity of the set J^{*}. It is important to note that numerical observations are usually made by iterating the orbits, so that the filled Julia set K

or the Julia set J is more directly accessible than the potential-theoretic Julia set J^*. It is known that $J^* = J$ holds if the Hénon map is uniformly hyperbolic [23], but the best known result in the non-hyperbolic situation is that

$$J^* \subset J. \tag{4.30}$$

If the two sets do not coincide, then it is possible that there are points in the set J such that they do not have ergodicity. Therefore it is important to see the relation between the sets J and J^* in the case where uniform hyperbolicity does not hold. If they represent the same set, it turns out that the orbits in the complex plane can reach everywhere in the Julia set. In section 6.3.3, we will present a numerical result for the Hénon map suggesting that $J^* = J$ is a reasonable hypothesis even in mixed situations.

On the other hand, the third statement of the above theorem helps a lot in our understanding of the dynamics in the complex plane. To explain what the properties $\overline{W^+(\mathfrak{p})} = J^+$ or $\overline{W^-(\mathfrak{p})} = J^-$ mean, let us consider the situation where the mixed phase space appears in the real phase space, and two distinct unstable periodic points, say $\mathfrak{p}$ and $\mathfrak{p}'$, are located in the real plane but separated by KAM curves. Obviously, two chaotic regions in the vicinity of $\mathfrak{p}$ and $\mathfrak{p}'$ do not communicate with each other within the real dynamics. However, the above theorem guarantees that there exists an orbit initially put in a neighborhood of $\mathfrak{p}$ can access a neighborhood of $\mathfrak{p}'$ through the complex plane. To see this, we first recall that $W^s(\mathfrak{p})$ and $W^u(\mathfrak{p}')$ are different invariant sets when $\mathfrak{p} \neq \mathfrak{p}'$, which shows that the forward Julia set J^+ contains points other than the points in the stable manifolds. Suppose here that an initial condition $\mathfrak{q}$ is chosen in such a way that $\mathfrak{q} \in J^+$ but $\mathfrak{q} \notin W^s(\mathfrak{p})$. Since $\overline{W^+(\mathfrak{p})} = J^+$, the iterated point of $\mathfrak{q}$ comes close to and passes by $\mathfrak{p}$. However, at the same time since $\mathfrak{q} \in J^+ = \overline{W^-(\mathfrak{p})}$, the point $\mathfrak{q}$ also approaches $\mathfrak{p}'$. The initial point $\mathfrak{q}$ should be complex; otherwise, the orbit can move only in a region bounded by KAM curves. In this way, one can see that the regions around unstable periodic points, even though they are separated by KAM curves in the real plane, are connected through the complex space.

4.2.3 Interior points of the filled Julia set and Siegel ball

If the sets $K^\pm$ have no interior points, then $\mathrm{vol}(K) = \mathrm{vol}(K^+ \cap K^-) = 0$ immediately follows. Here $\mathrm{vol}(K^\pm)$ denotes the four-dimensional volume (Lebesgue measure) of $K^\pm$ in $\mathbb{C}^2$. In this case, by definition, $K^\pm = J^\pm$ and $K = J$ holds. This means that all orbits that remain in a finite region, including KAM curves, are contained in J. Therefore, if $J^* = J$ holds even for mixed systems, KAM curves turn out to be contained in the set with hyperbolicity and mixing property.

If the Jacobian determinant of the Hénon map is not unity, *i.e.*, $|b| \neq 1$, rigorous results are known: (i) $\mathrm{vol}(K^+) = 0$ for $|b| > 1$ and (ii) $\mathrm{vol}(K^+) = 0$ or ∞ for $|b| < 1$ [63]. The inverse of the Hénon map is also the Hénon map with Jacobian determinant $1/|b|$, so the above results hold for the four-dimensional volume of K^- with Jacobian determinant $1/|b|$. On the other hand, for $|b| = 1$, which is our main concern, a rigorous result only tells us that $\mathrm{vol}(K^\pm) < \infty$.

As explained below, some speculation on the linearization around an elliptic fixed point suggests that $\mathrm{vol}(K) = 0$. It is well known that rotational domains appear when linearization around a neutral fixed point is achieved in the case of one-dimensional maps [64, 65]. Neutral fixed points are those points for which the associated stability is unity, *i.e.*, neither attracting nor repelling. When a neutral fixed point is linearizable, the so-called *Siegel disk* appears around the neutral fixed point [66]. Siegel disks occupy a positive area in $\mathbb{C}$, and so the filled Julia set K has a positive interior if the Siegel disk appears.

Linearization around a fixed point is also an issue in higher-dimensional complex maps. In the standard procedure for finding a transformation that provides linearization, the so-called *non-resonant condition* is required when constructing the perturbation expansion around the fixed point [64]. However, for the eigenvalues of the linearized matrix around an elliptic fixed point in the area-preserving map, there always appears a pair of eigenvalues $e^{i\kappa}$ and $e^{-i\kappa}$ with $\kappa \in \mathbb{R}$, which obviously violates the non-resonant condition. Therefore, it is impossible to proceed along with the standard procedure of linearization, and thus there is no chance to have Siegel balls, the higher-dimensional version of Siegel disks, around an elliptic fixed point.

4.3 Semiclassically contributing complex orbits and Julia sets

We have so far overviewed the fundamental properties of the two-dimensional polynomial complex map. Based on these facts, we next ask how signatures of two-dimensional complex dynamics manifest themselves in quantum tunneling, especially in the mixed system. As shown in section 3.3.2, the semiclassical approximation is performed by evaluating the multiple integral (3.23) using the saddle point method. The resulting semiclassical formula takes the form given by (3.25). The semiclassical propagator is evaluated by summing over all possible classical orbits which start with $q_0 = \alpha$ and end up with $q = \beta$. Note that initial and final positions α and β should be real-valued since they are observables. The set of points contributing to the semiclassical sum (3.25) is thus expressed as

$$\mathscr{M}_n = \mathscr{A} \cap f^{-n}\mathscr{B}, \tag{4.31}$$

where,

$$\mathscr{A} = \{(p,q) \in \mathbb{C}^2 \mid q_0 = \alpha \in \mathbb{R}\}, \quad \mathscr{B} = \{(p,q) \in \mathbb{C}^2 \mid q = \beta \in \mathbb{R}\}. \tag{4.32}$$

The support of the quantum states is given in general as a one-dimensional manifold in the two-dimensional real phase space. Depending on the situation, the support may be partially contained in the regular region and partially in the chaotic region, or can be completely inside the regular region in mixed phase space. Under such a generic setting, the following result has been obtained based on mathematical results for two-dimensional complex maps explained in section 4.2 [23, 24, 25, 26].

Theorem 6 ([48, 67, 68])**.** For the Hénon map $\mathscr{H}$, if the topological entropy on $\mathbb{R}^2$ is positive, then

$$J^+ \subset \overline{\mathscr{C}} \subset K^+ \tag{4.33}$$

holds. Here,

$$\mathscr{C} := \{(q,p) \in \mathscr{M}_\infty \mid \mathrm{Im}\, S_n(q,p) \text{ converges absolutely at } (q,p)\}, \tag{4.34}$$

and the set $\mathscr{M}_\infty$ is defined as

$$\mathscr{M}_\infty := \bigcup_{b \in \mathbb{R}} \lim_{n \to \infty} \mathscr{M}_n^{*,\beta}, \tag{4.35}$$

where,

$$\mathscr{M}_n^{*,\beta} := \{(q,p) \in \mathbb{C}^2 | p_n = \beta \in \mathbb{R}\}. \tag{4.36}$$

Here $\overline{X}$ indicates the closure of X.

Below we explain what this theorem tells us in the description of tunneling and to what extent complex orbits contributing to tunneling transport can be specified. First, we note that the positivity of the topological entropy in the real plane is required so that one has unstable periodic orbits in the real plane. As is numerically demonstrated, the Hénon map is expected to have chaotic regions and so unstable periodic orbits as well unless the nonlinear parameter a is negatively large. Note that for sufficiently large negative values of a, the elements of the filled Julia set K are empty in the real plane, and the above theorem excludes such a situation. It is by no means non-trivial to prove the positivity of the topological entropy in the real plane when the phase space is a mixture of regular and chaotic components. We thus assume the positivity of the topological entropy in the situation we are mainly concerned with.

The set $\mathscr{M}_\infty$ is introduced to represent the boundary conditions imposed to initial and final states. The supports for initial and final states are one-dimensional curves, either in the real or complex plane. On the other hand, if we fix the initial and final data, the obtained classical orbits contributing to the semiclassical sum depend explicitly on the values of α and β, which cannot be compatible with any invariant sets of the system. Therefore we have to prepare a setting that allows α and β to take arbitrary values.

The most relevant condition specifying the set $\mathscr{C}$ is the absolute convergence of Im $S_n(q,p)$. When the imaginary action Im S_n is not absolutely convergent as $n \to +\infty$, the following two situations are possible: Im $S_n \to +\infty$ or Im $S_n \to -\infty$. The former type of orbits is negligible, but the latter cannot be excluded in the sense of magnitude. However, the divergence of Im $S_n \to -\infty$ is obviously unphysical, and those orbits should be excluded from the semiclassical contribution. Here we only mention that the Stokes phenomenon automatically dissolves this issue and the orbits of the latter type are to be removed as a result of the Stokes phenomenon [22, 69].

We make a couple of technical remarks. The above theorem applies rigorously to the Hénon map or multiple compositions of Hénon maps at most. This constraint comes from the fact that rigorous results on complex dynamics in two dimensions are limited to the Hénon map, as explained in section 4.2 [23, 24, 25, 26].

This might be a restriction when one considers another class of systems such as the standard map, or the scattering map introduced below. In this respect, there are encouraging works, showing that similar behaviors are observed in the standard and semistandard map as well [70, 71]. In the next section, we also use a map containing transcendental functions in the form of iteration and show that the phenomena numerically found in the Hénon map are similarly observed.

The second technical remark is that the p-representation is assumed both in the initial and final states. Such a setting is also not necessary and could be replaced with more general representations. This is because the proof of the theorem fully makes use of the convergent theory of currents, which is briefly introduced in section 4.2.2. The convergent theorem applies for any algebraic varieties, which cover a wide class of manifolds supporting the quantum states.

As mentioned above,we can expect that $K^+ = J^+$ holds. If this is indeed the case, it turns out that the final statement becomes simpler: $\overline{\mathscr{C}} = J^+$. This shows that the orbits whose imaginary action is bounded are dense in the forward Julia set J^+. In other words, we do not need to take into account the orbits outside J^+ when we want to find the orbits contributing to the semiclassical propagator. In this sense, we can say that the Julia set controls tunneling transport.

Chapter 5

Dynamical tunneling and complex stable manifolds

The theorem stated in the previous chapter substantially narrows the candidate orbits and suggests that one should find out the contributing complex orbits from the set J^+ at least. However, the absolute convergence of imaginary action is a necessary condition, but not sufficient. Furthermore, the set J^+ still contains exponentially many orbits, thereby the candidate orbits are not so sharply specified yet.

To explain this more precisely, we recall that the property $\overline{W^s(\mathfrak{p})} = J^+$ holds for any unstable periodic orbits $\mathfrak{p}$. We can say further that if $K^+ = J^+$ holds, $\overline{\mathscr{C}} = \overline{W^s(\mathfrak{p})}$ follows. Although this does not mean $\mathscr{C} = W^s(\mathfrak{p})$, it is nevertheless true that the set $\mathscr{C}$ can well be approximated by $W^s(\mathfrak{p})$. In addition, infinitely many unstable periodic orbits are expected to exist even in the mixed phase space, and the stable manifold $W^s(\mathfrak{p})$ of any $\mathfrak{p}$ runs close to the orbits in $\mathscr{C}$. Hence, the set $\mathscr{C}$ must contain infinitely many orbits, each of which is associated with the stable manifold $W^s(\mathfrak{p})$.

On the other hand, the weight of each contribution in the semiclassical sum (3.25) is mainly governed by the imaginary part of the action, so not all of the complex orbits are equally contributing. The orbits with larger imaginary action are negligible in amplitude compared to those with smaller imaginary action. To specify the orbits, which are dominant or even most dominant in the semiclassical sum, we need more detailed information on the dynamics. In this chapter, we explore this issue by introducing a more appropriate system for the investigation.

5.1 Intersection of complex stable manifolds in the real plane and the initial manifold

We here consider the scattering map introduced in [72]:

$$f : \begin{cases} q_{n+1} = q_n + p_n \\ p_{n+1} = p_n - V'(q_n), \end{cases} \tag{5.1}$$

where,

$$V(q) = V_\kappa(q) + V_\varepsilon(q), \tag{5.2}$$

$$V_\kappa(q) = -\frac{\kappa}{16}\exp\left(-8q^2\right), \tag{5.3}$$

$$V_\varepsilon(q) = -\varepsilon\left[\mathrm{erf}(\sqrt{8}[q-q_b]) - \mathrm{erf}(\sqrt{8}[q+q_b])\right]. \tag{5.4}$$

with,

$$\varepsilon = \frac{\kappa\sqrt{\pi}}{2\sqrt{8}} q_f \frac{\exp(-8q_b)[2q_f - q_b]}{1-\exp\left(-32q_f q_b\right)}. \tag{5.5}$$

The parameters κ and ε control the strength of the perturbation and the depth of the central well around the origin, respectively. The parameter q_f specifies the position of the fixed points and the width of the potential well can be adjusted with q_b. The potential profile and a typical phase space portrait when mixed phase space is realized are displayed in Fig. 5.1. Note that for sufficiently large values of κ with some conditions on other parameters, we can rigorously show that the map [72] is uniformly hyperbolic [73]. On the other hand, for a moderate parameter region, regular regions coexist with chaotic orbits as seen in Fig. 5.1.

The reason for taking the scattering map introduced above, not for taking the Hénon map or standard map, is twofold. First, it provides a more natural scattering setting than the Hénon map. The Hénon map gives the area-preserving map with a cubic potential, so it also realizes a scattering situation. However, since the potential function drops to zero as q goes to infinity, the scattered orbits are accelerated, not approaching the motion with a constant speed, which would not be a natural setting for the scattering problem. On the other hand, for the scattering map introduced here, the orbit tends to a free motion asymptotically in classical mechanics and a plane wave in quantum mechanics.

The reason for not using the standard map is to avoid difficulties arising from quantum localization in the chaotic sea. The complex orbits assume a kind of amphibious character, and the orbits responsible for tunneling transports are correlated in the chaotic sea to create dynamical localization [74]. This happens in the standard map because a large chaotic region leading to dynamical localization is extended in the momentum direction. To minimize the effect of quantum localization, which necessarily brings the coupling of non-trivial quantum effects such as quantum tunneling and localization, we adopt a scattering setting.

5.2 Propagator and the initial manifold

For the time-evolution propagator, we consider the propagator in the form as shown in chapter 3

$$\langle q|U^n|I\rangle = \int\cdots\int\prod_j dq_j\prod_j dp_j \exp\left(\mathrm{i}\frac{S_n(I,q)}{\hbar}\right). \tag{5.6}$$

Here, I represents the action variable mimicking the regular region shown by a red ellipse in Fig. 5.1(b). The action $S_n(I,q)$ is explicitly written as

$$S_n(I,q) = \sum_{j=1}^{n}\left\{(q_j - q_{j-1})p_j - \frac{p_j^2}{2} - V(q_{j-1})\right\} + G(q_0,I), \tag{5.7}$$

where $G(q_0, I)$ represents the generating function leading to the transformation from the original coordinate (q_0, p_0) to the action-angle variable (I, θ):

$$G(q_0, I) = \int p_0(q_0', I) dq_0'. \tag{5.8}$$

Here the function $p_0(q_0, I)$ is obtained by solving the condition $I(q_0, p_0) = 1/2\sqrt{\lambda_1 \lambda_2}$, which specifies the position of the initial manifold. The initial manifold is determined by fitting a ellipse,

$$c_{11}q^2 + c_{12}qp + c_{22}p^2 = 1, \tag{5.9}$$

to the orbits numerically generated from an initial point inside the KAM region. The length of major and minor axes of the ellipse is respectively expressed as $1/\sqrt{\lambda_1}$ and $1/\sqrt{\lambda_2}$, where λ_1 and $\lambda_2 (\lambda_1 < \lambda_2)$ are the eigenvalues of the matrix c_{ij}. The rotating angle of the ellipse is given by $\phi = \tan^{-1}(v_{12}/v_{11})$, where (v_{11}, v_{12}) is the eigenvector associated with λ_1. The generating function $G(q_0, I)$ is then written using the angle variable θ, which is conjugate to the action variable I, as

$$G(q, I) = \frac{1}{2\sqrt{\lambda_1 \lambda_2}} \left(\theta + \frac{1}{2} \sin 2\theta \cos 2\varphi \right) - \frac{1}{8} \left(\frac{1}{\lambda_1} + \frac{1}{\lambda_2} \right) \cos 2\theta \sin 2\varphi. \tag{5.10}$$

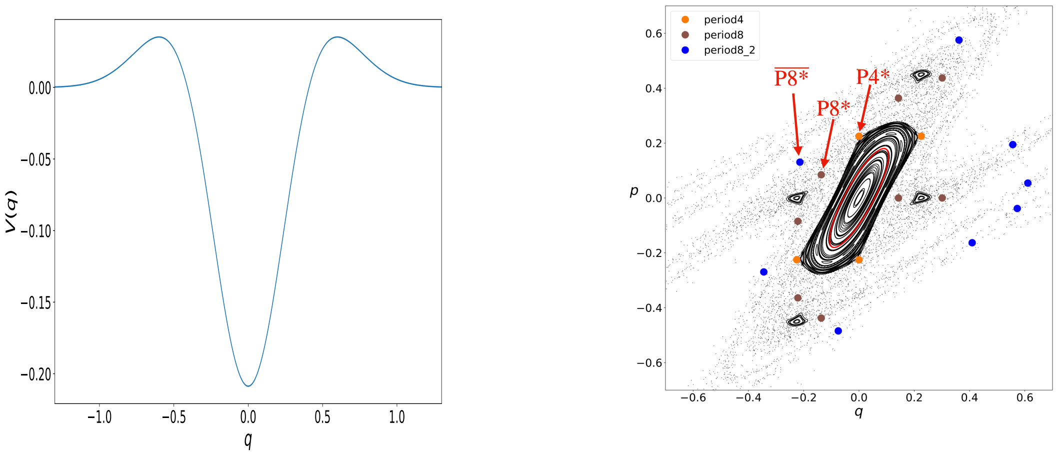

(a)

(b)

Figure 5.1: (a) The profile of the potential function given by (5.2). (b) The phase space for the scattering map with $\kappa = 3.0$, $q_f = 1.2$, and $q_b = 1.0$. The periodic point labeled by $P4^*$ is the target periodic point whose associated stable manifold provides the minimal imaginary action, and the imaginary action associated with the periodic point $P8^*$ is almost the same as the one with $P4^*$ (see text). The periodic point labeled by $\overline{P8^*}$ is the one whose associated imaginary action is much larger than the ones with the periodic points $P4^*$ and $P8^*$ (see text). The red curve in the KAM region represents the initial manifold taken to calculate imaginary actions.

The initial manifold specified by the action variable I is complexified by extending the angle variable to the complex plane as $\theta = \xi + \mathrm{i}\eta$. The complexified initial manifold is locally two-dimensional, and has a cylindrical shape, as in the case of the complex KAM curve depicted in Fig. 5.1(b).

5.3 Periodic points of the scattering mapping system

The first task in order to seek the most dominant complex paths guided by stable manifolds is to find the unstable periodic orbits in the chaotic sea. Systematic methods are not known allowing for complete enumeration of periodic orbits in two-dimensional area-preserving maps. For the Hénon map, the method proposed by Biham and Wenzel works well in the region where the map satisfies the horseshoe condition [75]. In this case, a generating function whose extrema provide periodic orbits is expressed in terms of binary symbols associated with the complete horseshoe, but it is difficult to apply it to the case where regular and chaotic orbits coexist.

Here we employ the method developed by Davidchack and Lai [76]. The method combines the idea proposed by Schmelcher and Diakonos [77] with the Newton method. (See more details in appendix A.) In any method, some tunings based on trial-and-error tests are needed for the choice of initial guesses and the step width for the iteration since the basin of attraction of the iteration for each periodic orbit is not known in advance. We have compared the two methods for the choice of initial guesses; the one suggested in [76], and the random sampling in which initial guesses are distributed randomly in the phase space. As shown in Fig. 5.2(b) and (c), we have obtained overall satisfactory results, although a periodic orbit with period 7 is missing in the first method. This is because the first method uses the periodic orbits with period $m-1$ and $m+1$ for the initial guesses, but periodic orbits with successive periods are not necessarily close with each other especially in the KAM region. The location of unstable periodic orbits up to period 8 is finally obtained as shown in Fig. 5.2. Note that the periodic orbits with periods 2 and 3 do not exist in the real plane. This fact can be confirmed as well in terms of the method of symmetry lines [78].

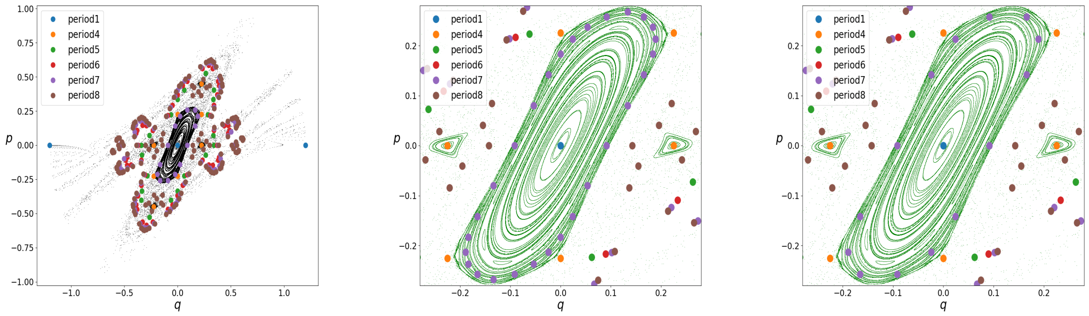

(a) (b) (c)

Figure 5.2: (a) Periodic orbits up to period 8 for the scattering map with $\kappa = 3.0, q_f = 1.2$, and $q_b = 1.0$. (b) Periodic orbits up to period 8, for which initial guesses are distributed randomly in the phase space. (c) Periodic orbits up to period 8, for which the periodic orbits with period $m-1$ and $m+1$ are taken as initial guesses. Note that a periodic orbit with period 7 is missing in case (c), compared to case (b), but the other ones are common in the two results.

5.4 Comparison of the magnitude of the imaginary part of the action along complex orbits

Below, we explain the reason why it is sufficient to compare the imaginary part of the action for complex orbits associated with periodic orbits in the real plane. Suppose that the complexified stable manifold $W^s(\mathfrak{p})$ of a certain periodic orbit $\mathfrak{p} \in \mathbb{R}^2$ intersects with the initial manifold I at a certain point, say $z(\mathfrak{p}) \in W^s(\mathfrak{p}) \cap I$. Recall that intersections between locally two-dimensional manifolds are isolated points in the four-dimensional space in general. As also anticipated from the result in section 4.3, the complexified stable manifold $W^s(\mathfrak{p})$ intersects with the manifold I, possibly infinitely many times, due to the entanglement in the complex plane. Consider the points contained in a small neighborhood of $z(\mathfrak{p})$ in the initial manifold I, and observe how the orbits contained in the neighborhood behave in time. Since the central point $z(\mathfrak{p})$ is a point on the stable manifold $W^s(\mathfrak{p})$, it approaches the periodic point $\mathfrak{p}$ as the number n of iteration gets large. If the size of the neighborhood is sufficiently small, the points in the neighborhood move in the region close to the stable manifold $W^s(\mathfrak{p})$ and approach $\mathfrak{p}$ as well. But these points pass by $\mathfrak{p}$ and eventually move away from $\mathfrak{p}$ because they are not the points exactly on the stable manifold $W^s(\mathfrak{p})$. After leaving p, these points move along the unstable manifold $W^u(\mathfrak{p})$. Suppose that a complex stable manifold $W^s(\mathfrak{p})$ extending from a periodic point $\mathfrak{p}$ on the real surface intersects an initial manifold I at a point. The complexified stable manifold is locally two-dimensional. The intersection between two 2-dimensional surfaces in a 4-dimensional space is generally a point. Let $z(\mathfrak{p})$ denote this point, which is contained in $W^s(\mathfrak{p}) \cap I$. Here, the complexified stable manifold $W^s(\mathfrak{p})$ may have infinite intersections with the manifold I due to the entanglement in the complex domain. Now notice that there should exist a one-dimensional curve in the neighborhood of $z(\mathfrak{p})$ in the initial manifold I such that the points in the curve, say $\mathscr{L}$, come close to the point $\mathfrak{p}$ as well, and then they move along the unstable manifold in the real plane, i.e., $W^u(\mathfrak{p}) \cap \mathbb{R}$. In other words, a point in the curve $\mathscr{L}$ taken to be sufficiently close to $z(\mathfrak{p})$ moves along $W^u(\mathfrak{p}) \cap \mathbb{R}$ for large n. Obviously, the closeness of the initial point to $z(\mathfrak{p})$ controls the closeness of the orbits from the real plane after passing by $\mathfrak{p}$. In addition, as proved in [73, 79], for the scattering map considered here, there exists a scattering region in which the motion becomes monotonic and diverges to infinity. Therefore, after approaching $\mathfrak{p}$ along the stable manifold $W^s(\mathfrak{p})$ the orbits do not gain imaginary actions because they almost behave as the real orbits. Since the final point q of the propagator $\langle q | U^n | I \rangle$ should be real-valued, the orbits first approaching the periodic orbit $\mathfrak{p}$ and then moving close to the real plane are expected to contribute to the final semiclassical sum. Consequently, to evaluate the tunneling probability from the initial state supported by the initial manifold to the scattering region, it is sufficient to evaluate imaginary actions of complex orbits moving along stable manifolds for the periodic orbits situated in the real plane.

5.5 Imaginary actions and dominant complex orbits

Having the data of periodic orbits in the real plane, we explore what determines the magnitude of the imaginary action of each orbit. Recall that the action is given as a sum over iterated variables, so we might expect that the faster the orbit reaches the real plane, the smaller the imaginary action is gained in its itinerary. To find the orbits approaching the real plane within a short time, it might be reasonable to focus on the stability of the target periodic orbit. Here, the target periodic orbit is referred to as the periodic orbit in the real plane to which the orbits on the complex stable manifolds tend from the initial manifold. This is because the orbits are attracted by the periodic orbit with large instabilities. We test this hypothesis for the periodic orbits obtained here.

Fig. 5.3 plots the imaginary action of the orbits along the stable manifolds as a function of the stability of the target periodic orbit. Note that the periodic orbit with period m has m periodic points, and the locations of intersections between the initial manifold I and the stable manifold $W^u(\mathfrak{p})$ emanating from each periodic point $\mathfrak{p}, f(\mathfrak{p}), \dots, f^m(\mathfrak{p})$ differ from each other, and each has their own imaginary action, whereas we use the stability exponent attached to the periodic orbit $\mathfrak{p}$, not to each periodic point, in the horizontal axis. Thus, for the same stability exponent there appear several plots, each of which belongs to the same periodic orbit.

Clearly, the hypothesis linked to the stability of periodic orbits does not work. Instead, the overall trend is the opposite. We should also note that within the same periodic orbit imaginary actions depend on which periodic point the orbit from the initial manifold approaches. As mentioned above, this is because the positions of intersection points in the initial manifold are different even though the stable manifold emanates from the same periodic orbit.

The next hypothesis is that the position on the initial manifold matters: the larger $|\eta| = |\text{Im }\theta|$ is, the smaller the imaginary action is gained in its itinerary. This hypothesis also comes from the observation that the action is evaluated by summing over iterated variables and an initial large value of the imaginary part might control the imaginary action. We check this hypothesis and find that, as presented in Fig. 5.3(b), it does not necessarily work for all the periodic orbits, but there exist several groups of periodic orbits, within each of which the hypothesized rule

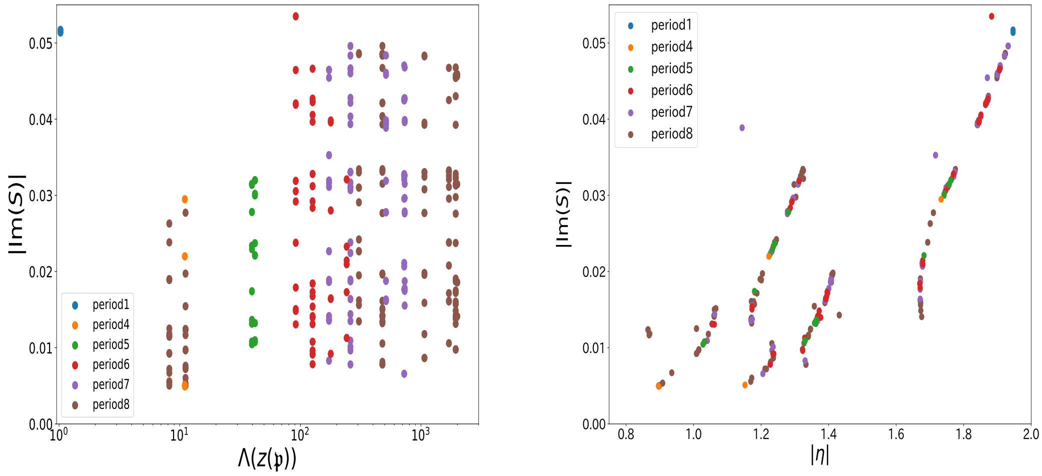

(a) (b)

Figure 5.3: The absolute value $|\text{Im } S|$ of imaginary actions versus (a) the stability exponent $\Lambda(z(\mathfrak{p}))$, and (b) the imaginary part $|\eta| = |\text{Im }\theta|$ of the initial condition. the hypothesis linked to the stability of periodic orbits does not work (see text). The stability exponent $\Lambda(z(\mathfrak{p}))$ is the larger eigenvalue of the linearized matrix $Df^m(\mathfrak{p})$ where m denotes the period. The initial manifold is given with $c_{11} = 311.31, c_{12} = -161.10, c_{22} = 108.57$.

works quite well. Here the group is referred to as the sequence of points and is shown in different colors in Fig. 5.4(a).

5.6 Characteristics of dominant orbits

The origin of forming the groups seen in Fig. 5.3(b) can be identified by plotting the position of intersections in the initial manifold I. As mentioned, the position in the initial manifold is specified by the coordinate $\theta = \xi + i\eta$. As shown in Figs. 5.4(a) and (b), the intersection points in each group are close to each other and form a sequence around the corresponding spot in the (ξ, η)-plane. As expected, the orbits whose initial conditions are close to each other in the (ξ, η)-plane follow a similar itinerary at an initial stage of iteration, but spreads over the entire real phase space after being close to the real plane finally, as shown in Fig. 5.4(c). One typical example is the periodic orbits with period 4 and period 8, whose locations in the real plane and in the (ξ, η)-plane are indicated in Figs. 5.1(b) and 5.4(d), respectively. The initial positions of these points are very close in the initial (ξ, η)-plane, so they take almost the same path in the complex plane, as shown in Fig. 5.5(a)-(c). After reaching the real plane, they separate with each other to approach each target periodic orbit, whose location is indicated in Fig. 5.1(b). Other orbits behave similarly; the initial conditions are localized to form a spot in the (ξ, η)-plane, but the final destinations shown in Fig. 5.4(b) are scattered in the real plane. Since the imaginary action is almost determined by the initial itinerary in the complex plane, the associated imaginary actions take almost the same value if the initial locations are close to each other, which is shown below.

We now point out an important characteristic of the most dominant complex orbits. As shown in Fig. 5.3(b), the orbit along the stable manifold associated with a periodic point with period 4 provides the minimal imaginary action. As marked in Figs. 5.1(b), this periodic orbit in the real plane is located close to the regular region. In other words, the complex orbits with smaller imaginary actions approach the sticky zone of the KAM region. As a result of this fact, the itinerary in the complex plane exhibits a pattern that is different from those observed in typical orbits approaching the periodic orbits in the chaotic region far away from the KAM region.

Figs. 5.5(a)–(c) display the behavior of the orbit in the complex plane approaching the periodic orbit with period 4. As clearly seen from Fig. 5.5(c), the orbit does not monotonically tend to the target periodic orbit, but it once goes under the real plane and then it goes up again. It finally approaches the corresponding periodic orbit in the real plane. Note that the orbit cannot behave in this way unless the orbit is temporally trapped by some invariant objects such as periodic orbits in the complex plane. The non-monotonicity, therefore, originates from chaos in the purely complex plane. In other words, the trajectory of the orbits dominantly controlling the tunneling transition is affected by the presence of complex chaos. The reason why one can say that chaos plays a role in the complex plane is that, as explained in detail in section 4.2.2, the dynamics in the complex plane is controlled by the Julia set J, which is the invariant set generating chaos. In particular, in the area-preserving map, there are several reasons to believe that the orbits that do not diverge to infinity are all contained in the Julia set. The behavior of the imaginary action is similar: it does not monotonically converge to a final value as a function of the time step, but, as displayed in Fig. 5.6(a), it once drops and then converges to a fixed value. This implies that cancellation of the imaginary action undergoes in time. Such a signature is common to other orbits leaving the initial manifold with smaller values of $|\eta|$.

In contrast to the orbits with smaller imaginary actions, the orbits tending to the periodic orbits far away from the regular region behave quite differently. As shown in Figs. 5.5(d)–(f), an orbit leaving in a deeply imaginary domain straightforwardly approaches the real plane and is strongly attracted by the associated periodic orbit. An example of such an orbit is shown by $\overline{P8*}$ in Fig. 5.1(b). Reflecting such behavior, the imaginary action also monotonically and rapidly converges to a final value as presented in Fig. 5.6(b).

So far, the role of chaos in the complex plane has not been explored in the issue of tunneling. In previous studies by Shudo and Ikeda [19, 20, 28, 48, 67, 68, 80], we have shown that the

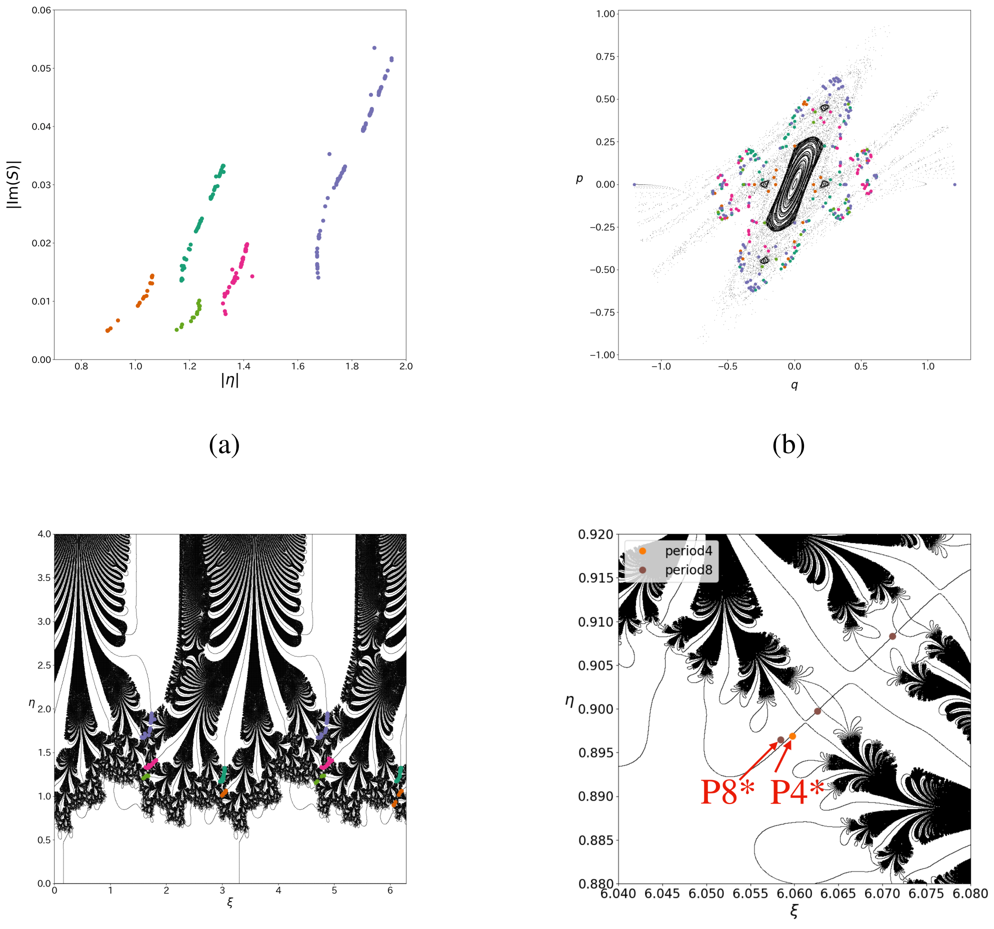

(a) (b)

(c) (d)

Figure 5.4: (a) The same plot as shown in Fig. 5.3, but the dots belonging to different groups are distinguished by different colors. (b) The target periodic points in the real plane where the groups in (a) are shown using the same colors. (c) The groups in (a) are shown in the initial value plane $\theta = \xi + i\eta$ using the same colors. The black curves represent the set $\bigcup_{\beta\in\mathbb{R}} \mathscr{M}_n = \bigcup_{\beta\in\mathbb{R}}\{(\xi,\eta)\in\mathbb{R}^2 | q_n(\theta=\xi+i\eta,I)=\beta\}$ of initial conditions, which contribute to the semiclassical propagator. (d) A magnification of (c). The intersections associated with the orbits (period 4 and 8) providing the minimal imaginary actions are shown by the arrows. These respectively converge to the periodic points marked in Fig. 5.1(b).

complex orbits are responsible for the tunneling transition between the regions dynamically disconnected within the classical dynamics, and the scenario proposed there was that chaos in the real plane attracts the complex orbits that reproduce tunneling tails. It has not been clear whether chaos in the complex plane plays a positive role. If the dominant complex orbit turns out to be the type of the orbits presented in Figs. 5.5(d)–(f), it turns out that only the nature of invariant sets in the real plane matters in the tunneling transition. However, what is found here is that chaos in the complex plane determines the tunneling transition and plays an essential role.

It should also be noted that the dominant complex orbits are attracted by the sticky region around the KAM region. This scenario reminds us of the works of Doron and Frischat [81, 82]. The authors have emphasized the importance of the coupling with what they called the beach state, which is nothing but the sticky region of the KAM region. Our observation could be a piece of evidence justifying the scenario proposed there. Further analysis is strongly desired to clarify why the orbits landing on the sticky region are temporarily trapped by invariant sets in the complex plane.

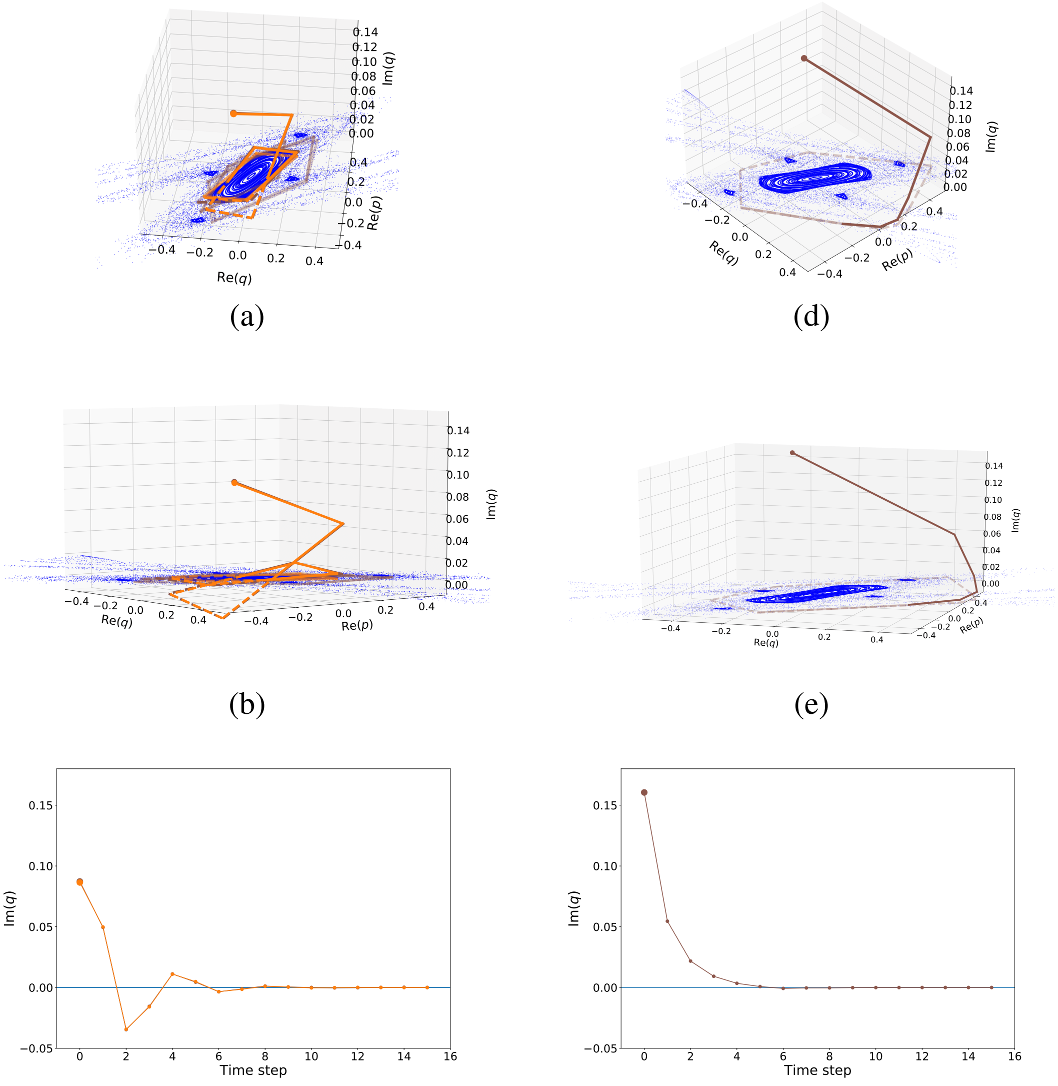

(a) (d)

(b) (e)

(c) (f)

Figure 5.5: (a) and (b) Itineraries of the orbits tending to the periodic points $P4^*$ and $P8^*$ indicated in Fig. 5.1(b). (b) is the same plot as (a) but from a different angle. (c) Im q_n for the same orbit shown (a) and (b) tending to the periodic points $P4^*$ and $P8^*$ plotted as a function of the time step. (d) and (e) Itineraries of an orbit approaching the periodic point $\overline{P8^*}$ located in the chaotic sea and far from the regular region, shown in Fig. 5.1(b). (f) Im q_n for the same orbit shown in (d) and (e) plotted as a function of the time step.

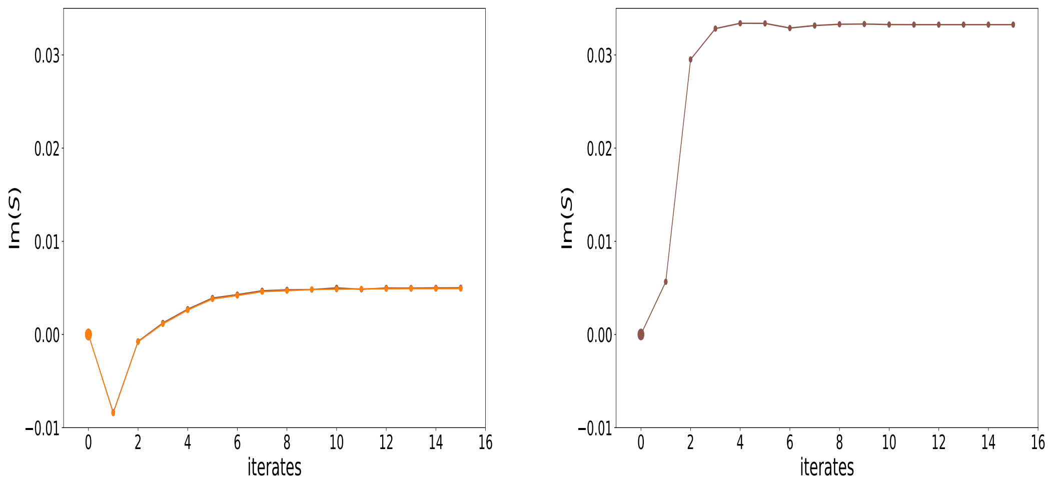

(a) (b)

Figure 5.6: The partial sum of the imaginary action summed up to given time steps for (a) the orbits tending to the periodic points $P4^*$ and $P8^*$, and (b) an orbit approaching the periodic point $\overline{P8^*}$ located in the chaotic sea.

Chapter 6

Ergodicity of complex dynamics and quantum tunneling in non-integrable systems

As mentioned in chapter 4, the problem of how to sort out the most dominant set of complex paths from potential candidates whose number grows exponentially with time or, in some classes of systems, infinitely many even within a finite time. This has been partially solved based on the results in the theory of complex dynamical systems [23, 24, 25, 25, 26, 63]. The results show that the orbits contained in the Julia set control the dynamical tunneling and the rest of the orbits have no chance to contribute [48, 67, 68]. This finding would be suggestive for our central question, *i.e.*, the essential difference of tunneling between integrable and non-integrable systems, since it is known that chaotic behavior is observed only in the Julia set [23, 24, 25, 25, 26, 63], which in turn implies that tunneling transport is driven by chaotic orbits in the complex plane.

As made in the previous chapter, further analysis has allowed a more detailed identification of the complex orbits that are most dominant in the Julia set [27]. This can be achieved by using a theorem that asserts that stable (or unstable) manifolds for any unstable periodic point are dense in the forward (resp. backward) Julia set [23, 24, 25, 25, 26]. The complex orbits that produce the tunneling transport are guided by stable manifolds associated with unstable periodic orbits in the real chaotic sea [28, 48, 67, 68]. In chapter 5, it was found that the orbits tending to the sticky zone around the KAM region provide the most dominant contribution in the semiclassical sum.

We should point out that there is a drawback to the time-domain semiclassical analysis: dynamical tunneling is a process that proceeds in a mixture of classically forbidden and allowed processes. Time-domain semiclassical calculations can only provide transition probabilities associated with this entire process. In other words, one cannot clearly separate the contribution from the pure tunneling process in the KAM regime from the process involving chaotic transport. The complexified stable manifold mechanism assumes the periodic orbits in the chaotic sea, and thus the second half of the process is inevitably influenced by the transport in the chaotic sea.

The main objective of this chapter is to elucidate the mechanism of tunneling transport within the KAM region using the complex path approach. To eliminate the influence of chaotic regions, we will prepare a system sufficiently close to a certain integrable limit. By doing so, we suppress the complexified stable manifold mechanism as much as possible. Nevertheless, we can observe that dynamical tunneling occurs, and the complex paths carry the tunneling amplitude as shown in this work.

To realize the situation where the influence of chaos is minimal, we consider an *ultra-near integrable system*, which was introduced in Ref. [4]. We say that the system is ultra-near integrable if the system is sufficiently close to a certain integrable limit such that none of the classical invariant structures inherent in non-integrability are visible in the classical phase space, compared to the scale of the Planck cell. Obviously, by definition, all the scenarios proposed so far to describe dynamical tunneling in non-integrable systems, such as chaos-assisted tunneling (CAT) [7, 83, 84] or resonance-assisted tunneling (RAT) [10, 11], could not be applied, since they all assume chaotic regions or nonlinear resonances in the size of the Planck cell.

6.1 tunneling tails for ultra-near integrable systems

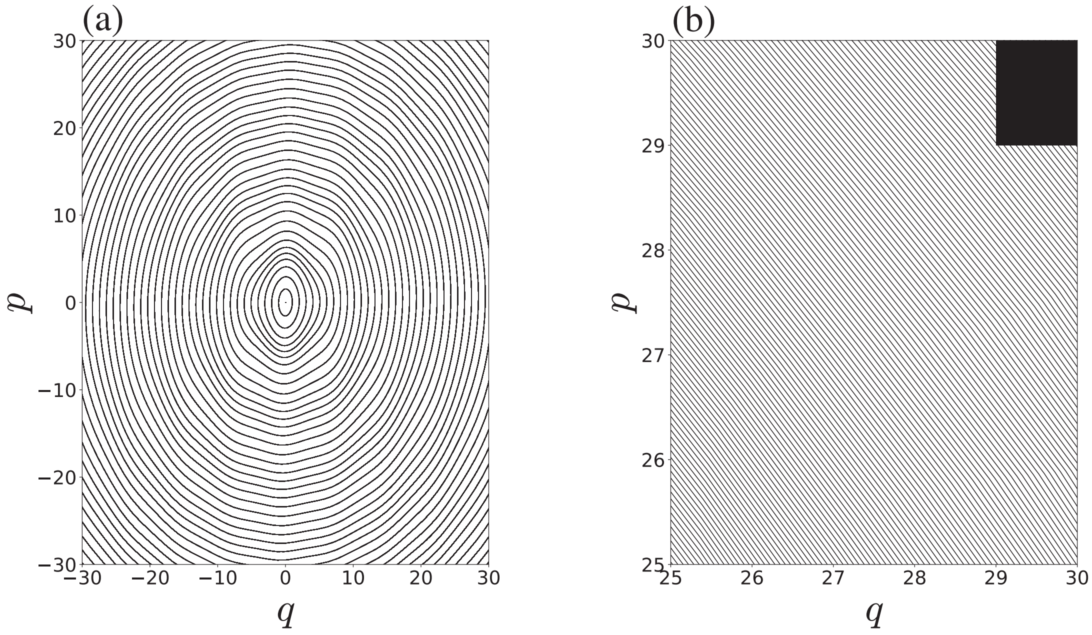

Figure 6.1: (a) Phase space profile of the classical map (2.24). The parameters of the potential function (6.1) are set to $\varepsilon = 1.0$, $\tau = 0.05$ and $\lambda = 1.2$. The plot (b) is a magnification of the plot (a). The black box put in the upper-right conner represents the Planck cell with $\hbar = 1$.

6.1.1 Classical and quantum map

As a model of non-integrable systems, we consider the periodically kicked rotor (2.21). The angular frequency for the periodic driving is given by $\Omega = 2\pi/\tau$. As usual, the classical time evolution from n-th to $(n+1)$-th kick is expressed as (2.24). In the limit of $\tau \to 0$, the classical map f tends to a continuous time flow system generated by the one-dimensional Hamiltonian $\mathscr{H}(p,q) = T(p) + V(q)$.

Time evolution of the corresponding quantum system is described by the unitary operator (3.20), which will be referred to as the quantum map hereafter. The eigenvalue equation for the quantum map is given by (3.21). The eigenvalues are distributed on the unit circle, which reflects the time-periodicity of the Hamiltonian (2.21). Here we assign the quantum number of quasi-eigenstates in the ascending order of the eigenvalues for the one-dimensional continuous Hamiltonian $\mathscr{H}(q,p)$.

6.1.2 Classical phase space for ultra-near integrable systems

Below, we consider the case with the kinetic term $T(p) = p^2/2$ and take the following potential function

$$V(q) = \frac{1}{2}q^2 - 2\varepsilon \cos\left(\frac{q}{\lambda}\right), \tag{6.1}$$

where λ and ε are the parameters specifying the length of modulation and the perturbation strength to the harmonic term, respectively. Recall that a similar potential function was used in Ref. [85], but the error function was present there.

For $\tau \ll 1$, the system becomes close to the one-dimensional continuous Hamiltonian $\mathscr{H}(p,q)$, thus the phase space is almost covered by KAM curves, as displayed in Fig. 6.1. When the parameter ε is small, the KAM circles are slightly deformed due to the presence of the modulation term in the potential $V(q)$. The reason for calling such a situation as ultra-near integrable is that the structures, such as Poincaré-Birkhoff chains or stochastic layers around the separatrix, are invisible compared to the size of the Planck cell. In other words, if the size of the Planck constant is small enough to resolve the structures of nonintegrability origin, we do not refer it to ultra-near integrable systems.

6.1.3 Tunneling tails of eigenfunctions

A natural expectation for the profile of the eigenfunctions would be that they exhibit a simple monotonic decay, as the integrable limit $\tau \to 0$. However, as seen in Fig. 6.2(a), the ground state $|\langle q|\Psi_0\rangle|^2$ does not yield a monotonically decaying profile, but the staircase structure appears in the tunneling tail when ε is set large. Here, numerical calculations have been performed using the Advanpix Multiprecision Computing Toolbox for MATLAB [86], which allows to raise the precision arbitrarily as far as the computational time is permitted [4].

For comparison, we plot the eigenfunctions for the one-dimensional continuous Hamiltonian, which is obtained by solving the eigenvalue equation,

$$\hat{H}^{(M)}_{q\mathrm{BCH}} \left|\Phi^{(M)}_k\right\rangle = E^{(M)}_k \left|\Phi^{(M)}_k\right\rangle, \tag{6.2}$$

where $E^{(M)}_k$ and $\left|\Phi^{(M)}_k\right\rangle$ denote eigenvalues and the associated eigenfunctions for the Hamilto-

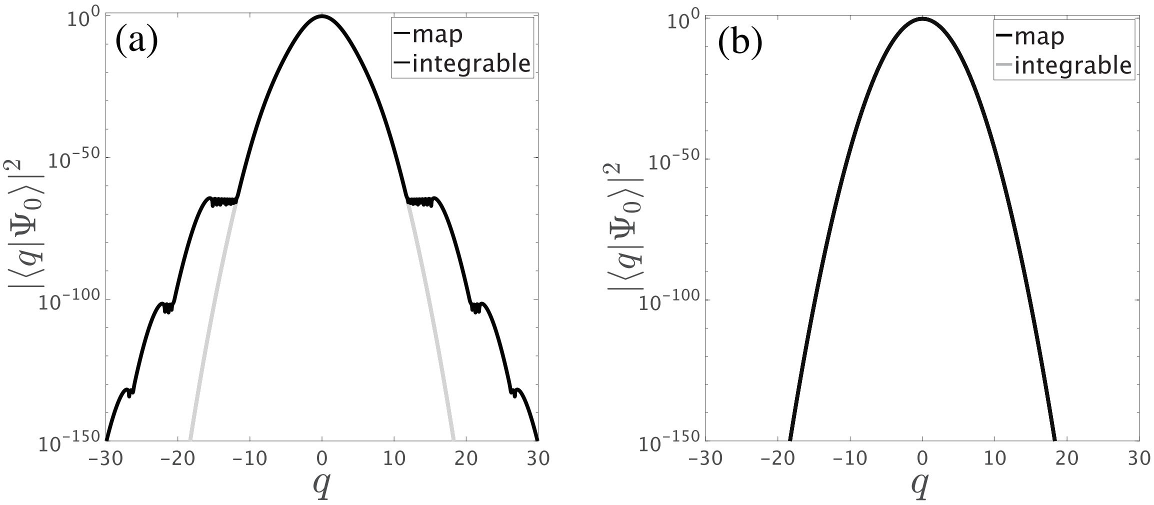

Figure 6.2: The black curve shows the ground state eigenfunction for the quantum map (3.21), and the gray one shows that for the truncated quantum BCH Hamiltonian $\hat{H}^{(M)}_{q\mathrm{BCH}}$ with $M = 3$. The parameters in the potential function (6.1) are set to (a) $\lambda = 1.2$ and (b) $\lambda = 3.0$, respectively. The remaining parameters are set to $\tau = 0.05$, $\varepsilon = 1.0$ and $\hbar = 1$.

nian,

$$\hat{H}^{(M)}_{q\mathrm{BCH}} = \sum_{j=1}^{M} \left(\frac{\tau}{\mathrm{i}\hbar}\right)^{j-1} \hat{H}_j. \tag{6.3}$$

Here $\hat{H}^{(M)}_{q\mathrm{BCH}}$ is obtained by truncating the Baker-Campbell-Hausdorff (BCH) Hamiltonian defined through the relation

$$\exp\left(-\frac{\mathrm{i}\tau}{\hbar}V(\hat{q})\right)\exp\left(-\frac{\mathrm{i}\tau}{\hbar}T(\hat{p})\right) = \exp\left(-\frac{\mathrm{i}\tau}{\hbar}\hat{H}_{\mathrm{BCH}}\right), \tag{6.4}$$

where

$$\hat{H}_{\mathrm{BCH}} = \hat{H}_1 + \left(\frac{\tau}{\mathrm{i}\hbar}\right)\hat{H}_2 + \left(\frac{\tau}{\mathrm{i}\hbar}\right)^2 \hat{H}_3 + \cdots . \tag{6.5}$$

Explicit expressions for $\hat{H}_n$ $(n \in \mathbb{N})$ can be derived from the BCH formula.

As demonstrated in Ref [4], the KAM curves for the classical map shown in Fig. 6.1 are perfectly approximated by the classical analog of the truncated quantum BCH Hamiltonian. Therefore, $\hat{H}^{(M)}_{q\mathrm{BCH}}$ can be a good candidate for the instanton approximation or direct tunneling [13, 15, 87]. As verified in Ref [4], the profile of $|\langle q|\Phi^{(M)}_0\rangle|^2$ does not change even with increasing truncation order M, implying that the original system is already sufficiently close to the integrable limit $\mathscr{H}(q,p)$. The reason why the step structure appears in Fig. 6.2(a) and not in Fig. 6.2(b) will be discussed in Section 6.4.6.

We cannot immediately conclude that the observed step structure originates from the non-integrability of the system only because the eigenfunction of the quantum map does not have

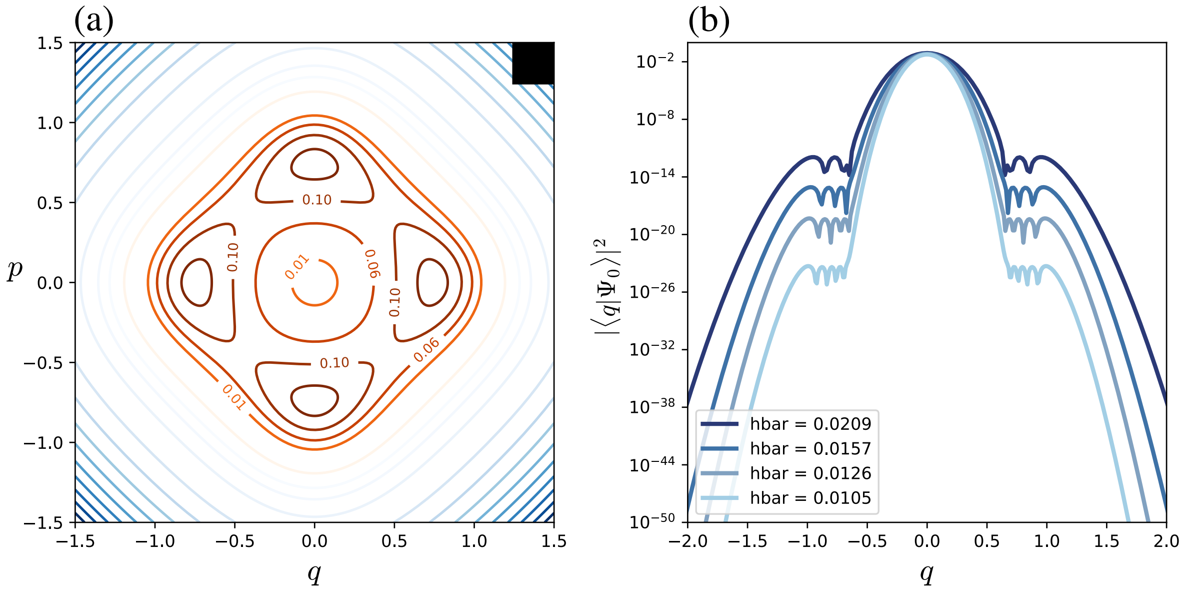

Figure 6.3: (a) Classical phase space profile for the Hamiltonian (6.6). (b) The ground state quantum eigenfunction with different values of the Planck constant. The corresponding eigenvalue is $E_0 = 6.24 \times 10^{-3}$. The black box at the right upper corner in the plot (a) represents the Planck cell for the case of $\hbar = 0.0105$. The parameters in Eqs. (6.6) and (6.7a) are set to $a = -0.55$ and $\varepsilon = 0.1$.

a monotonic tunneling tail but creates the step structure. To show this, we consider the one-dimensional Hamiltonian in a normal form, which is similar to the normal form studied in [88, 89]:

$$H(q,p) = H_0(q,p) + \varepsilon H_1(q,p), \tag{6.6}$$

with

$$H_0(q,p) = \frac{1}{2}(q^2+p^2) + a(q^2+p^2)^2, \tag{6.7a}$$

$$H_1(q,p) = p^4 - 6p^2q^2 + q^4. \tag{6.7b}$$

In Fig. 6.3, we give the classical phase space profile and the ground state eigenfunction for the corresponding quantum Hamiltonian. Clearly, the step structure appears in the tunneling tail at the exact location is exactly where the island-like equi-energy contours appear in the corresponding classical phase space. Therefore, the non-monotonic tunneling tail does not necessarily imply that the system is non-integrable. It is important to note that, as shown in Fig. 6.3(b), the position of the step does not move in the q-direction with the change of the Planck constant $\hbar$. As pointed out below, this is in sharp contrast to the ultra-near integrable situation.

Note that the island-like equi-energy contours are not nonlinear resonances because the system is one-dimensional and thus resonance cannot happen there. The staircase in this case consists of only one step, but in principle one could construct the one-dimensional Hamiltonian whose eigenfunctions mimic the staircase with multiple steps. However, this does not help to explain the observed phenomenon.

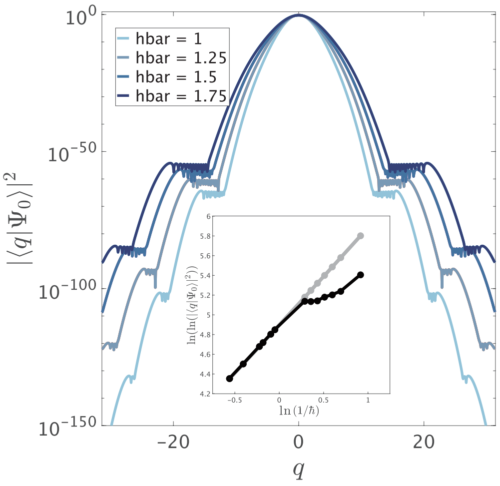

Figure 6.4: Ground state eigenfunction for the quantum map (3.21) where $V(q)$ is given by (6.1). with different values of the Planck constant. (Inset) Magnitude of the ground state eigenfunction at a fixed position ($q = 11$) plotted as a function of $1/\hbar$. Black and gray curves show the ground state eigenfunction for the quantum map (3.21) and for the truncated quantum BCH Hamiltonian $\hat{H}^{(M)}_{q\mathrm{BCH}}$ with $M = 3$, respectively. In both figures, the other parameters are set to $\tau = 0.05$, $\varepsilon = 1.0$, and $\lambda = 1.2$.

6.1.4 Planck constant dependence of the step structure

It would not be reasonable to hypothesize that the RAT mechanism works in the ultra-near integrable situation. First, as seen in Fig. 6.1, the nonlinear resonances, if any, are too small compared to the size of the Planck cell. The RAT mechanism is supposed to start only after the Planck cell resolves nonlinear resonances [15]. Before the RAT regime, the direct tunneling mechanism dominates, and a simple exponential decay without any specific structures is expected in the tunneling rate γ [15] (or the tunneling splitting ΔE) vs $1/\hbar$-plot [42]. The existence of the direct tunneling regime could be intuitively understood by the fact that the Planck cell smears out the underlying classical structures. As the the Planck constant becomes smaller, nonlinear resonances become visible. As a result, the transition from direct to RAT-driven tunneling is expected to take place. This is the scenario assumed in the RAT theory.

On the other hand, apart from the standard RAT scenario, one might think that extremely small nonlinear resonances could affect extremely small tunneling tails. It must be true that any invariant structure, no matter how small, will in principle leave some form of fingerprints on the corresponding quantum wave function. However, if the size of such nonlinear resonances is too small compared to the width of the step observed here, they cannot be the support of the step structure. Too thin nonlinear resonances cannot cover widespread plateaus in the q-direction.

More decisive evidence to exclude the possible role of nonlinear resonances is the $\hbar$-dependence of the step structure presented in Fig. 6.4. If the step structure were linked to some classical invariant objects, the steps should have kept the same position even if the Planck constant was changed. Recall that this is exactly realized in the integrable model examined above. The RAT assumes that the coupling is mediated by classical resonances, so that the resulting structure in the tunneling tail should be attached to the associated nonlinear resonances. This means that the step should not move with the change of the

Planck constant, just like the situation shown in Fig. 6.3(b). It would not be possible to explain the $\hbar$-dependent behavior within the RAT scenario. On the contrary, none of the scenarios based on certain classical invariant structures can explain the $\hbar$-dependent staircase structure [7, 10, 11, 14, 15, 16, 83, 84, 90, 91, 92].

Observation of the wave function amplitude at a certain fixed position reveals a non-trivial $\hbar$-dependence. As illustrated in the inset of Fig. 6.4, the wave function amplitude for the truncated quantum BCH Hamiltonian $\hat{H}^{(M)}_{q\mathrm{BCH}}$ exhibits a simple exponential decay, as expected. On the other hand, the amplitude of the eigenfunction for the quantum map shows an exponential decay in a large $\hbar$-regime, but it switches to a stretched exponential-type decay. The slope returns to 1 for smaller $\hbar$. Notice that stretched exponential regions appear when the observation points hit a plateau region of the wave function. We recall that similar behavior has also been found in tunneling splitting vs. $1/\hbar$ plot [42], where non-exponential regions appear due to the quantum resonance between the librational and rotational states, *i.e.*, the *coupling across the separatrix* in the phase space.

6.1.5 Quantum resonance

As clarified in Ref. [4], both the step structure and its $\hbar$-dependence are explained as manifestations of the *quantum resonance*. Here we show that the excited states satisfying the quantum resonance condition produce the step structure in the tunneling tail. Figure 6.5(a) plots the ground state under the the quantum BCH basis $\left|\Phi^{(M)}_k\right\rangle$ in logarithmic scale. We can see that the ground state of the quantum map is well approximated by that of the BCH basis, which is manifested by a sharp drop of the curve near the ground state energy. After this initial drop, the curves decay overall exponentially, except for small peaks indicated by the arrows in the plot.

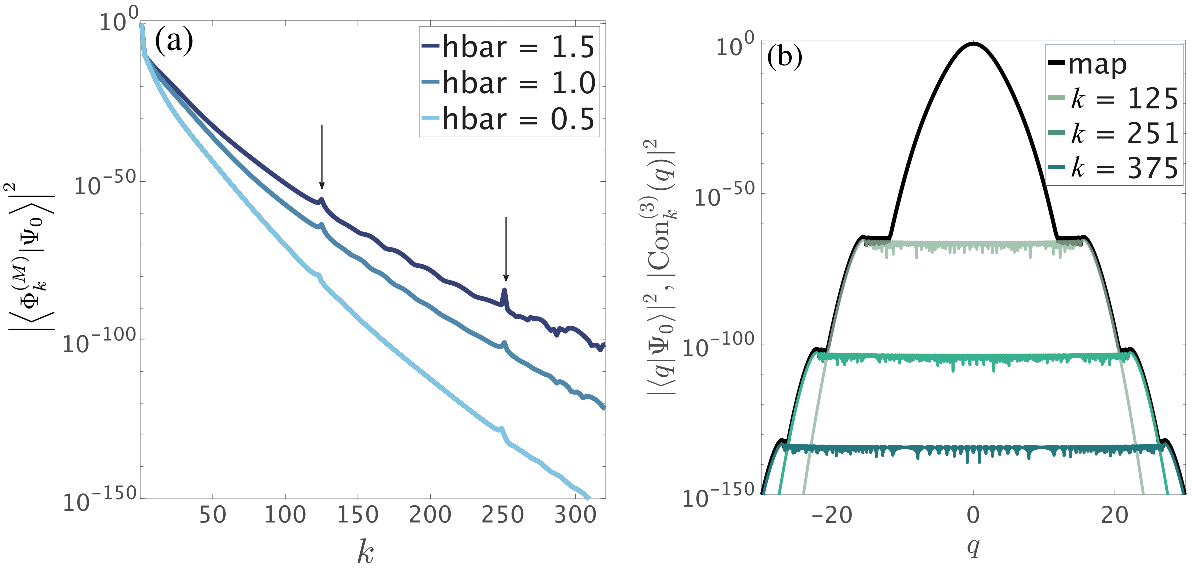

Figure 6.5: (a) Ground state eigenfunctions in the quantum BCH representation $|\Phi^{(M)}_k\rangle$ with $M = 3$ for different values of $\hbar$. (b) Ground state eigenfunction in the q-representation in the case $\hbar = 1$ (black). The states, $k = 125$, $k = 251$, and $k = 375$ in the sum (6.9), are superposed and shown in different green colors. These states are responsible for the small peaks indicated by the arrows in plot (a). The parameters are set to $\tau = 0.05$, $\varepsilon = 1.0$, and $\lambda = 1.2$.

The eigenvalues corresponding to the peaks can be read off from Fig. 6.5(a). That is, the component $\left\langle \Phi_k^{(M)} \middle| \Psi_0 \right\rangle$ takes a large value when the resonance condition

$$E_k^{(M)} = E_0^{(M)} + mE_{\mathrm{ex}}, \qquad m \in \mathbb{N} \tag{6.8}$$

is satisfied. Here note that the energy associated with the periodic kick is given by $E_{\mathrm{ex}} := 2\pi\hbar/\tau$. This condition (6.8) can also be derived from the perturbation analysis [4]. That is, taking the BCH Hamiltonian $H_{q\mathrm{BCH}}^{(M)}$ as the unperturbed Hamiltonian, the time-dependent perturbation calculation tells us that the resonance condition (6.8) is given by the condition that the denominator of the first-order perturbative term is zero.

We can directly confirm that the coupling with the states creating small peaks in the plot of $\left|\left\langle \Phi_k^{(M)} \middle| \Psi_0 \right\rangle\right|^2$ is responsible for the staircase found in the plot of $\left|\langle q|\Psi_0\rangle\right|^2$ (see Fig. 6.3). To this end, we expand the ground state as [42],

$$\langle q|\Psi_0\rangle = \sum_k \left\langle q \middle| \Phi_k^{(M)} \right\rangle \left\langle \Phi_k^{(M)} \middle| \Psi_0 \right\rangle. \tag{6.9}$$

Instead of taking the sum over all states k, we include only the states responsible for generating the peaks observed in Fig. 6.5(a). As shown in Fig. 6.5(b), the resulting state reproduces the observed staircase in the eigenfunction.

The role of quantum resonance has also been emphasized in nearly integrable situations [42]. For the standard map in a nearly integrable regime, the component $\left|\left\langle \Phi_k^{(M)} \middle| \Psi_0 \right\rangle\right|^2$ exhibits a series of equally spaced peaks at the energies satisfying the same quantum resonance condition (6.8). As a result, the staircase structure appears in the tunneling splitting ΔE vs $1/\hbar$ plot. In contrast to the spikes associated with classical nonlinear resonances [42], the staircase in the ΔE vs $1/\hbar$ plot induces the *persistent enhancement* of tunneling splittings. Here, the persistent enhancement is referred to as a phenomenon in which the anomalous enhancement of the splitting compared to the integrable limit is persistently maintained with the change of $1/\hbar$. The staircase structure observed in the splitting plot becomes less clear as the perturbation strength τ increases [42]. This is because the classical phase space becomes more complicated when the system is not sufficiently close to the integrable limit. In this respect, the ultra-near integrable system is a simpler or more ideal model than the system with a relatively large perturbation. For this reason, we can expect that the study of ultra-near integrable systems will advance our understanding of persistent enhancement.

6.1.6 Time evolution of wave packet and staircase structure

In the following sections we will seek a semiclassical understanding of the step structure observed in the previous section. However, as mentioned in Section 3.3.1, there is no semiclassical formula that provides eigenfunctions of non-integrable systems, and so the most we can do is to perform the semiclassical analysis in the time domain. We thus study the time-dependent problem, instead of observing the eigenfunctions.

Here, we observe the time evolution of the coherent state,

$$\langle q|\psi_0\rangle = \left(\frac{1}{\pi\hbar}\right)^{\frac{1}{4}} \exp\left[-\frac{1}{2\hbar}\left(q - \langle q\rangle_\alpha\right)^2 + \frac{i}{\hbar}\langle p\rangle_\alpha \left(q - \langle q\rangle_\alpha\right)\right]. \tag{6.10}$$

The center of the wave packet is chosen as $(\langle q\rangle_\alpha, \langle p\rangle_\alpha) = (0,0)$. Since the potential (6.1) is close to the harmonic potential when $\varepsilon \ll 1$, this initial packet is close to the ground state of the quantum map. As a result, we may expect that the initial wave packet is strongly coupled to the states satisfying the quantum resonance condition (6.8).

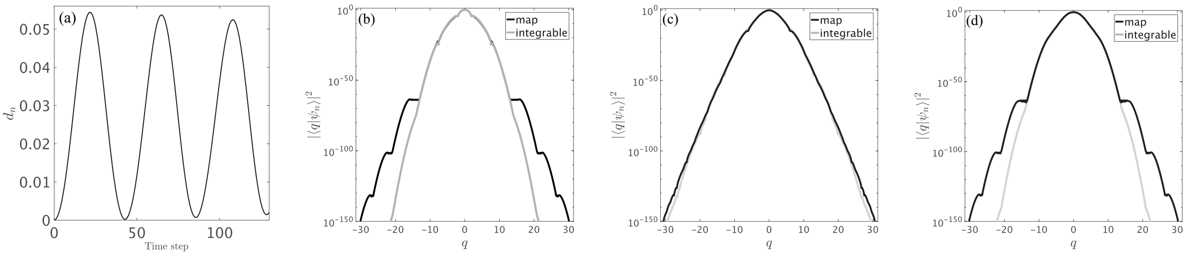

Figure 6.6: (a) The variation of the difference d_n between the time evolution of the quantum map and that of the quantum BCH Hamiltonian with $M = 3$ (see Eq. (6.11)). Snapshots of the time-evolved wave function at (b) $n = 63$, (c) $n = 94$, and (d) $n = 126$ in case of $\hbar = 1$. The parameters in the potential function (6.1) are set to $\tau = 0.05$, $\varepsilon = 1.0$, and $\lambda = 1.2$, respectively.

Figure 6.6(a) plots the difference between the time evolution of the quantum map and that of the BCH Hamiltonian with $M = 3$ as a function of the time step. The difference is measured using the norm defined by

$$d_n := \int_{-\infty}^{\infty} \left| \langle q|\hat{U}^n|\psi_0\rangle - \langle q|e^{-\frac{i}{\hbar}\left(\hat{H}_{q\mathrm{BCH}}^{(M)}\right)n}|\psi_0\rangle \right|^2 dq. \tag{6.11}$$

As can be clearly seen, the wave function of the quantum map oscillates periodically in time, and the period can be estimated in terms of the oscillation period of the states satisfying the quantum resonance condition. Recall that the time evolution of the coherent state $|\psi_0\rangle$ is expressed using the definition $E_{\mathrm{ex}} = 2\pi\hbar/\tau$ as

$$\langle q|\hat{U}^n|\psi_0\rangle = \sum_k \exp\left(-\frac{2\pi \mathrm{i} E_k}{E_{\mathrm{ex}}} n\right) \langle q|\Psi_k\rangle \langle \Psi_k|\psi_0\rangle . \tag{6.12}$$

Considering the phase part depending on the time step n, we find that the period N during which the ground state $|\Psi_0\rangle$ returns to the initial phase is given by the condition $(E_0/E_{\mathrm{ex}})n = 1$, which leads to $N\colon = E_{\mathrm{ex}}/E_0$. Since the coherent state (6.10) is close to the ground state $|\Psi_0\rangle$, we can expect that the projection $\langle \Psi_0|\psi_0\rangle$ to be maximum among others. As can indeed be verified in Fig. 6.6, the profile of the absolute value $|\langle q|\hat{U}^n|\psi_0\rangle|^2$ becomes close to that of the ground state at $n = kN/2 \ \ (k \in \mathbb{N})$.

The periodic revival allows us to study the origin of the step structure based on the time-domain semiclassical approach. The strategy adopted in the next section is essentially the same as that used in the time-domain semiclassical analysis for the mixed phase space situation [19, 20]. However, chaos in the real plane plays a significant role in the mixed phase space case, whereas the *rotational domains* in the complex plane control the observed feature of tunneling, as explained below.

6.2 Time-domain semiclassical propagator

In the following, we develop the time-domain semiclassical analysis in the complex domain. We will use the standard formulation based on the Van Vleck-Gutzwiller propagator [45, 93].

In the previous subsection we took the coherent state as the initial state of the time evolution and observed the time evolved wave function in the q-representation. We therefore consider the propagator $\langle q|\hat{U}^n|E\rangle$ where n denotes the time step. The propagator is expressed in a discrete Feynman path integral form:

$$\langle q|\hat{U}^n|E\rangle = \int\cdots\int\prod_j dq_j\prod_j dp_j \exp\left(\frac{\mathrm{i}}{\hbar}S_n(E,q)\right). \tag{6.13}$$

As mentioned above, the coherent state $|\psi_0\rangle$ is close to the ground state $|\Psi_0\rangle$ of the quantum map, and the support of the state $|\Psi_0\rangle$ can be well expressed by the action variable E, since the system is ultra-near integrable. Thus, we denote the variable representing the initial coherent state $|\psi_0\rangle$ by the symbol E. The classical action is written as

$$S_n(E,q) = \sum_{j=1}^{n}\Big((q_j - q_{j-1})p_j - \frac{\tau}{2}p_j^2 - \tau V(q_{j-1})\Big) + G(q_0,E), \tag{6.14}$$

where $G(q,E)$ is the generating function leading to the transformation from the original coordinate (q,p) to the action-angle variable (E,θ):

$$G(q,E) = \int^q p(q',E)dq'. \tag{6.15}$$

The function $p(q,E)$ is obtained by solving the condition $E(q,p) = \text{const}$, where the constant specifies the position of the initial classical manifold.

As a simple choice, we take an ellipse as the initial condition, as we did in the section 5.2. More specifically, the initial manifold is determined by fitting a rotated ellipse,

$$\Gamma : c_{11}q^2 + 2c_{12}qp + c_{22}p^2 = 1, \tag{6.16}$$

to the orbits numerically generated from an initial point on the manifold with $E_0^{(M)} = -1.24$. The generating function $G(q,E)$ is then written with the angle variable θ, which is conjugate to the action variable E, as Eq. (6.14).

To perform the semiclassical analysis in the complex domain, the initial manifold specified by the action variable E has to be complexified, which is achieved by extending the angle variable θ to the complex plane as $\theta = \xi + \mathrm{i}\eta$. Note that the complexified initial manifold E is locally two-dimensional.

The resulting expression of the semiclassical propagator takes the form as

$$\langle q|\hat{U}^n|E\rangle \simeq \sum_\gamma A_\gamma \exp\left(\mathrm{i}\frac{S_\gamma}{\hbar} - \mathrm{i}\frac{\pi}{2}\mu_\gamma\right), \tag{6.17}$$

where the sum γ is taken over all classical paths starting at the initial manifold E and ending at the final position q. $A_\gamma = \sqrt{\left|\det\frac{\partial^2 S_n^{(\gamma)}}{\partial q_n \partial q_0}\right|}$, and S_γ stand for the amplitude factor and the classical action for the classical orbit γ, respectively, obtained by inserting the path of each orbit. μ_γ represents the associated Maslov index.

6.3 Ergodicity in the complex space

As mentioned in introduction of chapter 6, transport between classical forbidden regions can only be achieved using the complex orbits. The instanton allows the tunneling transition between the regions separated by the potential barrier. However, the situation to which the instanton method can be applied is limited at most to one- or multi-dimensional integrable systems [94].

As shown in chapter 4, in the case of polynomial maps, the dynamics in the complex plane exhibits ergodicity even though the phase space in the real plane is decomposed into different ergodic components. We will claim the ergodicity of the dynamics in the complex plane, based mainly on rigorous results for polynomial maps and numerical results for the maps involving transcendental functions, including the form of our potential (6.1). Ergodicity in the complex plane has also been studied numerically for the standard and semi-standard maps [70, 71]. We expect that a similar scenario holds for continuous flow systems, but it would be a much harder task to claim this fact even numerically.

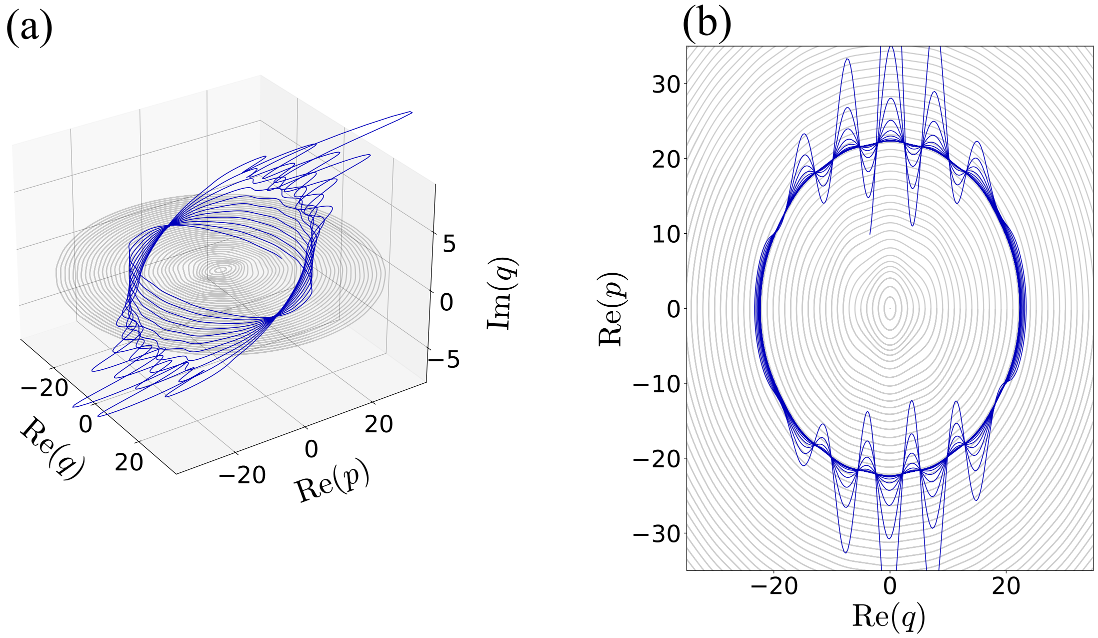

Figure 6.7: An example of CRK. (a) Projection onto the $(\mathrm{Re}\, q, \mathrm{Re}\, p, \mathrm{Im}\, q)$ space. (b) Projection onto the $(\mathrm{Re}\, q, \mathrm{Re}\, p)$ plane. The parameters are set to $\tau = 0.01$, $\varepsilon = 1.0$, and $\lambda = 1.2$.

6.3.1 Complexified real KAM curves

As for the rotational domain in the area-preserving map, the set of KAM curves could be a candidate in the area-preserving map. For a given angular frequency $\widetilde{\omega}$, the motion on the KAM curve, denoted by $\mathscr{C}_{\widetilde{\omega}}$, is expressed as a constant rotation using an appropriate coordinate, say φ, as

$$\sigma : \varphi \mapsto \varphi + 2\pi\widetilde{\omega} \pmod{2\pi}. \tag{6.18}$$

To find such a coordinate φ, the conjugation function h is introduced and it should satisfy the functional equation, $\sigma\big(h(p,q)\big) = h\big(F(p,q)\big)$. The functional equation could be solved, for example, by assuming the form of the Fourier series [95]

$$h(\varphi) = \sum_{m=-\infty}^{+\infty} h_m e^{im\varphi}. \tag{6.19}$$

If such a series has a positive radius of convergence in the complex φ-variable, then the corresponding invariant curve with a given angular frequency $\widetilde{\omega}$ survives in the real plane. A positive radius of convergence $\widetilde{\omega}$ implies that the corresponding KAM curves exist not only in the real but also in the complex plane. The motion on the resulting curve is also expressed as a rotation (6.18) with the same angular frequency $\widetilde{\omega}$ in the φ-coordinate. Hereafter, we call the set of such closed curves *complexified real KAM curves* (CRK), meaning that the curves are obtained by complexifying the conjugate function $h(\varphi)$ associated with a real KAM curve. Since the orbits on the KAM curves, either in $\mathbb{R}^2$ or in $\mathbb{C}^2$, are bounded as $n \to \pm\infty$, they are by definition contained in $K = K^+ \cap K^-$.

An example of CRK is shown in Fig. 6.7. This was not direclty obtained by calculating the conjugate function $h(\varphi)$, but by iterating an orbit starting from a point sufficiently close to the real plane. As confirmed in Ref. [27], if the real phase space is almost covered by the KAM curves, the orbits started in this way follow the CRK well. The orbit, initially close to the real plane, spirals up in a small interspace between successively aligned cylindrical walls formed by a series of CRK obtained by scanning the imaginary angle $\operatorname{Im}\varphi$. Such a spiral motion along a bundle of CRK curves is a typical behavior observed for orbits in the complex plane. The orbit eventually reaches a certain imaginary region and forms a wavy circle there (see Fig. 6.7). This wavy pattern is an indication that the natural boundary of the conjugation function $h(\varphi)$ is nearby. The natural boundary is a superposition of many more wave components, typically of a fractal nature [95, 96, 97, 98].

6.3.2 Complexified complex KAM curves

Invariant circles are not necessarily associated with the KAM curves in the real plane. To see this, we consider the case with $\varepsilon = 0$ in the potential function (6.1). In this case, the map is simply reduced to the discrete linear oscillator,

$$f_{\text{linear}} : \begin{pmatrix} q \\ p \end{pmatrix} \mapsto \begin{pmatrix} q + \tau p \\ p - \tau(q + \tau p) \end{pmatrix}. \tag{6.20}$$

The mapping relation (6.20) is nothing but the first order symplectic integration of the harmonic oscillator $\mathscr{H}(q,p) = p^2/2 + q^2/2$, so the map f_{linear} preserves the quantity,

$$E = \frac{1}{2}p^2 + \frac{1}{2}q^2 + \frac{1}{2}\tau qp. \tag{6.21}$$

For $E \in \mathbb{R}$, the orbits obviously move in the real plane. Note, however, that the value of E need not be real, but can be complex, *i.e.*, $E = |E|e^{\mathrm{i}\alpha}$ $(\alpha \in \mathbb{R})$. The constant of motion E makes sense for $E \in \mathbb{C}$, and the motion is confined by the complex-valued manifold. Note that the space $(E,\varphi) \in \mathbb{C}^2$ completely spans $\mathbb{C}^2$.

When ε becomes non-zero, the KAM scenario holds in the real plane, as explained. We may develop a similar argument not only in the real plane but also in the complex plane [99]. A

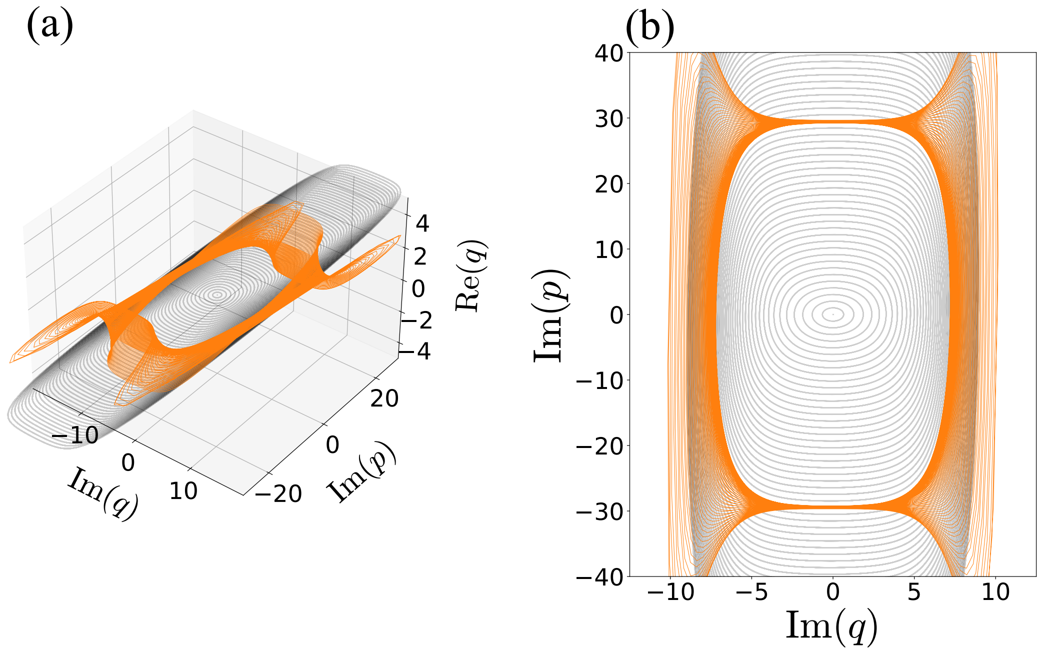

Figure 6.8: An example of CCK. (a) Projection onto the $(\operatorname{Im} q, \operatorname{Im} p, \operatorname{Re} q)$ space. (b) Projection onto the $(\operatorname{Im} q, \operatorname{Im} p)$ plane. The parameters are set to $\tau = 0.01$, $\varepsilon = 1.0$, and $\lambda = 1.2$.

simple way of looking at this is to perform a $\alpha = \pi/2$-rotation, that is $q \to \mathrm{i}q$ and $p \to \mathrm{i}p$, which results in the same map (2.24) with the potential

$$\widetilde{V}(q) = \frac{1}{2}q^2 + 2\varepsilon \cosh\left(\frac{q}{\lambda}\right). \tag{6.22}$$

The pure imaginary plane $(q, p) \in \mathrm{i}\mathbb{R}$ is thus an invariant plane under the map, and the orbits starting from it remain there. Although these invariant circles are not KAM curves in the standard terminology, we call these invariant curves *complex KAM curves* here. It is not clear whether or not the complex KAM curves exist not only in the pure imaginary plane $(q, p) \in \mathrm{i}\mathbb{R}$, but also more generally in the complex plane [99]. If such complex KAM curves exist, we can also expect them to form a family of invariant circles as seen in the pure imaginary plane (see Fig. 6.8). We call them complex KAM curves as in the case of the pure imaginary plane.

If the complex KAM curves have the same origin as the real KAM curve, we can expect that *complexified complex KAM curves* (CCK) will also appear, based on a similar argument using the conjugate function for the real KAM curves. It would be difficult to construct the conjugate function in general, but we can provide numerical evidence for the existence of the CCK associated with the pure imaginary plane $(q, p) \in \mathrm{i}\mathbb{R}$. Figure 6.8 shows an orbit moving along a set of closed curves in the pure imaginary plane, and it forms a cylindrical wall as in the case of the CRK (see Fig. 6.7). The CRKs are associated with a real KAM curve as mentioned above, while the CCKs are formed associated with a complex KAM curve.

We should note that the total dimension spanned by the rotational domains discussed here does not amount to the full dimension. First, for a given angular frequency $\widetilde{\omega}$, if the radius of convergence of the conjugate function $h(\varphi)$ is positive, the function $h(\varphi)$ can be analytically continued up to each natural boundary. As a result of the extension in the imaginary φ direction, we gain an additional dimension.

Second, the angular frequency of KAM curves has a positive Lebesgue measure in the angular frequency interval, so we gain another dimension in the angular frequency space, due to the KAM theorem. More precisely, this follows from the fact that the irrational numbers satisfying the Diophantine condition have a positive Lebesgue measure in the real numbers.

Third, we have a further extension in the α direction as performed above. It turns out that the total volume of the rotational domains including the complex KAM curves is less than 4, since unperturbed invariant circles with rational angular frequencies are broken when the perturbation is added, and thus the Hausdorff dimension in the direction of the rotation number is less than one. This implies that the bundle of rotational domains associated with KAM curves does not occupy a 4-dimensional volume. This speculation, together with the absence of the Siegel ball, suggests that the filled Julia set $K = K^+ \cap K^-$ has an empty interior.

6.3.3 J and J^* for the Hénon map

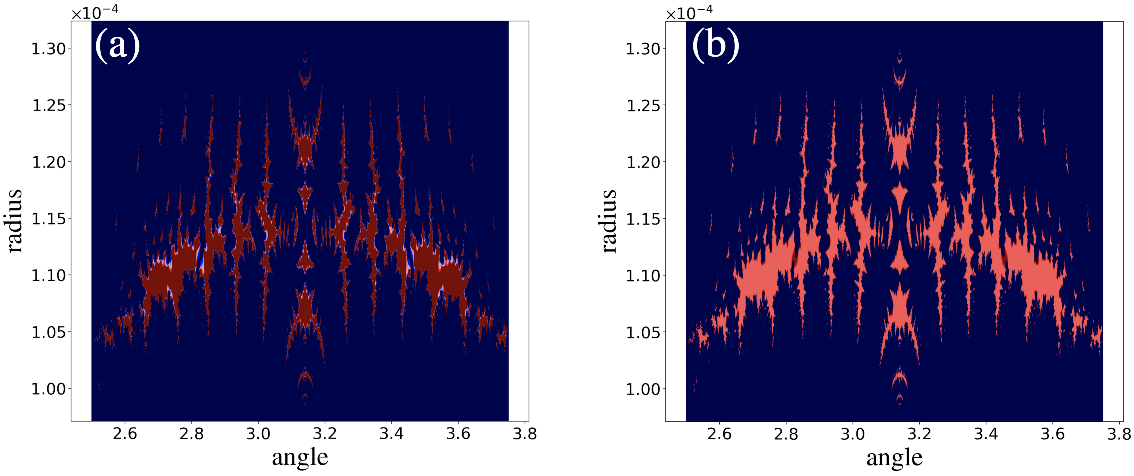

Figure 6.9: (a) The intersection $W^u(\mathfrak{p}) \cap K^+$ between the unstable manifold of an unstable fixed point $(x,y) = (0,0)$ for the Hénon map and the forward filled Julia set K^+. The plots are drawn in the coordinate plane (Θ, r) (see text). The colors reflect the number of time steps up to which the orbits leaving each point in this frame leave a properly chosen finite-sized box. The red regions show the set of initial points that remain in a finite region for a sufficiently long time, while the orbits in the blue region diverge to infinity relatively in a short time. (b) The Green function $G^+(x,y)$, which is evaluated numerically according to the definition (4.21). The parameters of the Hénon map (4.12) are set to $a = 0.8$ and $b = 1$.

Here we provide further evidence that ergodicity in the complex plane is not a far-fetched hypothesis, but a rather reasonable one. The first observation is the comparison of J with J^* for the Hénon map. There may be several ways to visualize the Julia set in $\mathbb{C}^2$, for example by taking a 3-dimensional slice or projection onto a 2- or 3-dimensional plane. However, as discussed above, the Julia set is likely to have null 4-dimensional volume. This means that a random sampling of the initial points in $\mathbb{C}^2$ will not hit the points on J. So we take a slice of J by an unstable manifold, because unstable manifolds are contained in J^- by definition, which restricts our sample space to a (locally) two-dimensional plane.

For this purpose, we introduce a local coordinate on the unstable manifold, which is expressed in terms of the coordinates in the radial and angle direction as

$$\{(\xi_x = r\cos\Theta, \xi_y = r\sin\Theta) \mid (\delta/\lambda) \le r \le \delta,\ \Theta_1 \le \Theta \le \Theta_2\}, \tag{6.23}$$

where λ is the stability exponent for the unstable direction. Below, Θ_1 and Θ_2 are taken such that the orbits in the Julia set are contained in this frame. The radial-angle coordinate is used to represent the Julia set on the unstable manifold.

If the orbits initially placed on the unstable manifold remain in a finite region as $n \to +\infty$, then these points are contained in the forward filled Julia set K^+. If $K^+ = J^+$ holds, then such orbits should be contained in the set $J = J^+ \cap J^-$. Note that it will be still difficult to find the orbits that do not diverge to infinity, since a two-dimensional slice of J is expected to be an object whose dimension is less than one if $K^+ = J^+$ holds.

Figure 6.9 plots the intersection $W^u(\mathfrak{p}) \cap K^+$, where $\mathfrak{p}$ is an unstable fixed point of the Hénon map. The plot was obtained by counting the number of iterations up to which the orbits leaving each point in this frame leave a properly chosen box of finite size. Thus, the plot can be considered as an approximation of $W^u(\mathfrak{p}) \cap K^+$. By increasing the iteration step, we can observe that all points eventually diverge to infinity and do not stay in a finite region, even though the shirking rate is extremely slow. This is also another numerical proof that the set K^+ does not have a finite 4-dimensional volume. As can be seen, the set K^+, as well as the set J^+, exhibits a fractal structure, which is a typical signature of the Julia set in one-dimensional complex maps [52].

We show the Green function $G^+(p,q)$ in Fig. 6.9(b) using the local coordinate introduced above. Here, the Green function $G^+(p,q)$ is numerically evaluated according to the definition (4.21). As explained in Chapter 4, the support of the Green function $G^+(p,q)$ is the set J^+. We can see that the finite-step approximation of J^+, shown in Fig. 6.9(a), gives a similar profile to the support of $G^+(p,q)$, shown in Fig. 6.9(b). This result therefore suggests that $J = J^*$ holds even if the phase space is a mixture of regular and chaotic orbits and the system is not uniformly hyperbolic.

6.3.4 Ergodicity in the complex plane for the ultra-near integrable system

Rigorous results for the Hénon map introduced in Section 4.2.1 imply ergodicity of the dynamics in the complex plane. The orbits are mixing and thus ergodicity follows on the potential-theoretic Julia set J^*. The argument developed in the last paragraph of Section 4.2.2, based on the fact that $\overline{W^s(\mathfrak{p})} = J^+$ and $\overline{W^u(\mathfrak{p})} = J^-$ for any unstable periodic orbit $\mathfrak{p}$, suggests that any two regions are connected via the complex plane if the two regions contain unstable periodic orbits.

Next, we examine the ergodicity for the map under consideration. The formulation based on the Green function is only available in the case where the map is expressed as polynomial functions. This is because the normalization, which is achieved by the factor $1/2^n$ in Eq. (4.21), is not available if the map contains transcendental functions. Hence, we perform brute-force numerical experiments to verify the ergodicity here.

Since our current interest is in the transition from the classical manifold supporting the quantum initial wave packet $|\psi_0\rangle$, we focus on the transitivity of the orbit starting from the manifold specified by the action E, which is more explicitly specified by the rotated ellipse Γ given in Eq. (6.16).

Here we focus on the orbits starting from the initial manifold, which is specified by the coordinate (E,θ), and tending towards the real KAM or complex KAM curves. The latter

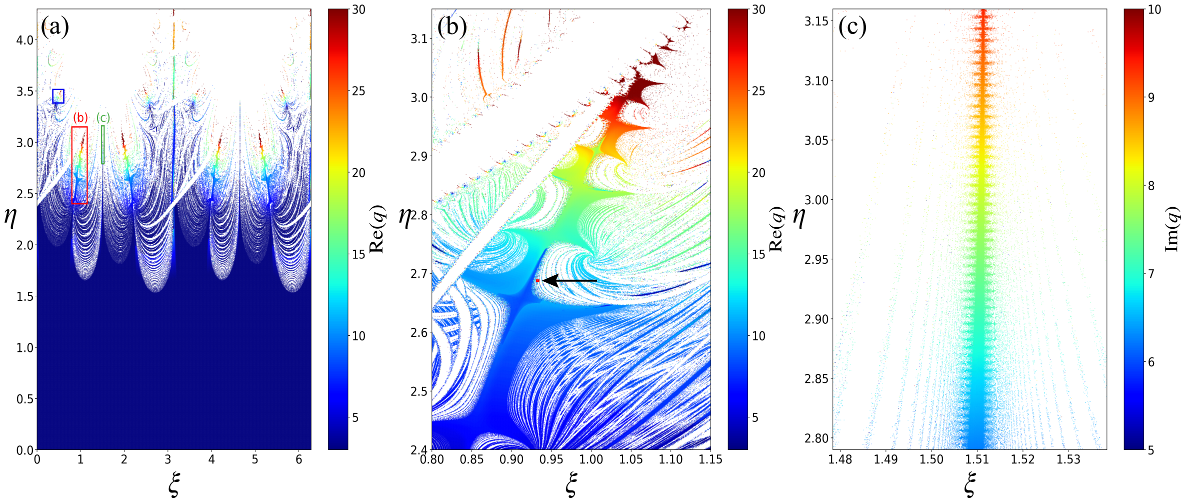

Figure 6.10: (a) The color plot of the radius of the real KAM curves that the orbits first approach. The part indicated by the blue box at the upper left is referred to in Fig. 6.15. (b) Magnification of the part indicated by the red box in plot (a). The small red box with the arrow indicates the area that is magnified to show the hierarchical structure in Fig. 6.12(a). (c) Magnification of the area indicated by the green box in plot (a). In plot (c) we place the colors representing the radius of the imaginary KAM curves to which the orbits first tend. The parameters are set to $\tau = 0.01$, $\varepsilon = 1.0$, and $\lambda = 1.2$.

is chosen here as the pure imaginary plane. As explained above, the orbit comes close to a family of CRKs or CCKs and then spirals down to the associated real or complex KAM curve. Figure 6.10(a) shows the initial value plane $\theta = \xi + \mathrm{i}\eta$, on which we place the colors representing the radius of the real KAM curves to which the orbits first tend. The radius of each KAM curve is measured using the coordinate of the position where the corresponding real KAM curve intersects. Figure 6.10(b) is a magnified plot of Fig. 6.10(a), whereas Fig. 6.10(c) shows a part of the initial conditions that first approach the CCK curves associated with the $(\operatorname{Im} q, \operatorname{Im} p)$ plane. In the latter case, the radius of the KAM curves is also measured using the coordinate of the position where the associated complex KAM curve intersects. Note that the set of initial conditions associated with the CCK (see Fig. 6.10(c)) is located around $\xi = \pi/2$ or $3\pi/2$. The positions are shifted exactly by $\pi/4$ in the ξ-direction from the position for the CRK. In other words, the initial conditions for CRK and CCK are found in the (ξ, η)-plane with different values of ξ.

These figures tell us that the target KAM curves change continuously as one varies the initial condition, meaning that the orbits on the initial manifold can transfer to any KAM curves, either in the real or imaginary plane. The initial manifold chosen here is nothing special, so this result suggests ergodicity in the complex plane. Moreover, as plotted in Fig. 6.12(a), if we zoom in some spots, we can find a similar color pattern, which implies that the observed structure is self-similar and hierarchical. The detail of this tree-like structure is described in Fig. 6.12(b).

After approaching the real (resp. imaginary) plane, the orbits spiral up along the family of CRK (resp. CCK) associated with a real (resp. imaginary) KAM curve that the orbits first approach. Then they switch to another CRK (or CCK) and start spiraling down again. An orbit

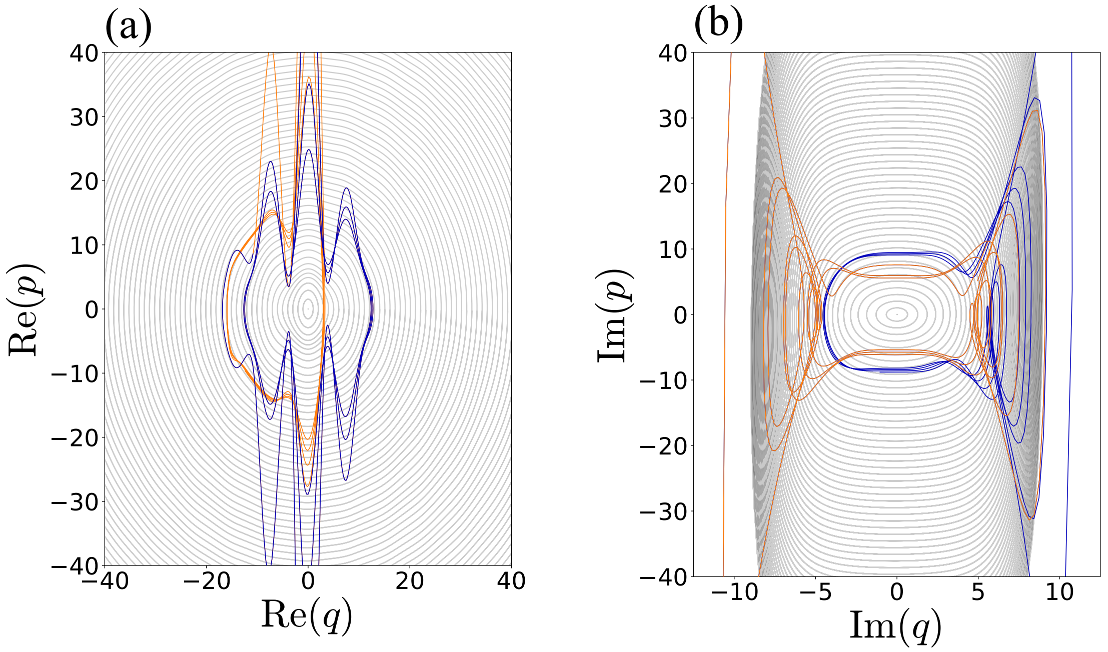

Figure 6.11: An example of the orbit that first rotates around a set of CRK (blue) and then switches to a set of CCK (orange). (a) Projection onto the $(\mathrm{Re}\, q, \mathrm{Re}\, p)$ plane. (b) Projection of the same orbit onto the $(\mathrm{Im}\, q, \mathrm{Im}\, p)$ plane. The parameters are set to $\tau = 0.01$, $\varepsilon = 1.0$, and $\lambda = 1.2$.

exhibiting such behavior is shown in Fig. 6.11. Figure 6.11(a) and (b) show the orbits projected on the $(\mathrm{Re}\, q, \mathrm{Re}\, p)$ plane and the $(\mathrm{Im}\, q, \mathrm{Im}\, p)$ plane, respectively. The orange and blue parts represent the spiral motion along the CRK and CCK curves, respectively. In this case, the orbit first rotates around a CRK and then switches to a CCK. On the other hand, an orbit shown in Fig. 6.14(b) exemplifies the case where the transition occurs from one CRK to another CRK. These observations also confirm the transitivity of the orbits in the complex plane.

6.4 Imaginary action of complex paths and the plateau amplitude

6.4.1 Classification of the type of the orbits

As confirmed in the previous section, the orbits in the complex plane explore the set J in an ergodic way, so that the orbit initially placed on the initial manifold Γ can come close to arbitrary real KAM curves. The question we have to ask then is which complex orbits give the most dominant contribution to the semiclassical propagator (6.13). The magnitude of each contribution in the semiclassical sum (6.17) is determined by the amplitude factor and the magnitude of the imaginary part of the action (imaginary action, for short). Of these, we focus on the imaginary action because it controls the order of magnitude of the tunneling tail. The amplitude factor could come into play, especially if one needs to examine the balance between the number of contributing orbits and each weight associated with the amplitude factor, but we

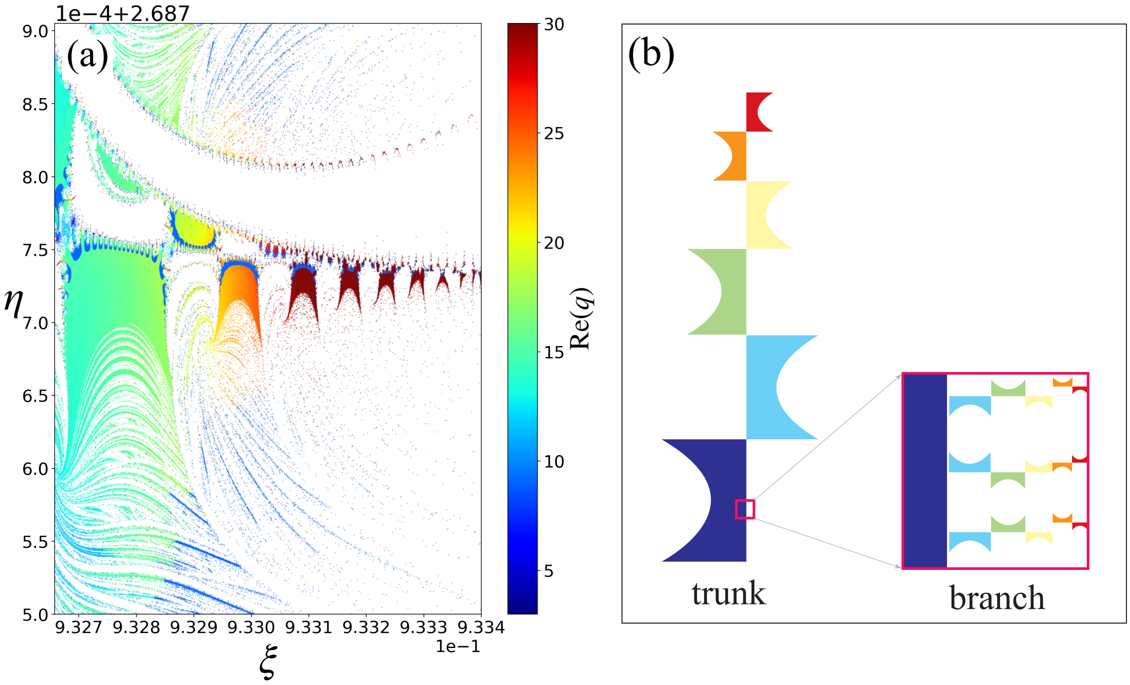

Figure 6.12: (a) The area that enlarges the small red box indicated by the arrow in Fig. 6.10(b). (b) Illustration of the hierarchical structure. The vertically aligned structure on the left side represents the trunk shown in Fig. 6.10(b). The horizontally aligned structures in the right box represent the branches growing from the trunk, and one such branch structure is shown in plot (a).

will not develop such a detailed argument here, just try to find a rough estimate in terms of the imaginary action.

To do this, we first classify the type of complex orbits according to their itinerary in the complex plane. As explained in the previous section, the orbits spend most of their time along either the CRK or the CCK. They exhibit spiral motions along them unless they are exactly on the KAM curves. Therefore, it makes sense to classify the type of orbits according to whether they are along the CRK or along the CCK. Note that the initial manifold Γ is close to the former type of orbits.

Figure 6.7 displays the case where the orbits first move to the CRK, while Fig. 6.8 gives the case corresponding to the CCK. As remarked above, these two types of orbits are found in separate regions of the (ξ,η)-plane. In the course of time, the orbits once moving along a set of CRK curves may jump to other CRK or CCR curves and vice versa, as shown in Fig. 6.11. Thus, we need to further classify the orbits according to which complexified KAM curves the orbits approach after moving once along a complexified KAM curve.

The itinerary of the orbits is encoded in the hierarchical structure in the (ξ,η)-plane. Figure 6.12(a) gives the area that enlarges the small red box pointed by the arrow in Fig. 6.10(b).

The main trunk, shown in Fig. 6.10(b), represents the orbits that jump directly to the target CRK, and the higher-order branches, shown in Fig. 6.12(a), represent the orbits that stop over several CRKs before reaching the target. Figure 6.12(b) illustrates the hierarchical structure in the (ξ, η)-plane. Similar tree structures appear in the case of CCK, although not shown here.

6.4.2 Imaginary action of roundabout paths

The classical action (6.14) is given as a sum over intermediate variables. So we can expect that the longer the detour, the larger the imaginary action will be. In particular, if the orbit once travels along a set of the CCK and returns to another set of the CRK, it gains an extra imaginary action, resulting in a smaller contribution to the semiclassical propagator.

Before examining roundabout paths, we confirm that the orbits associated with the CCK do not qualify as candidates for the semiclassical contribution. In Fig. 6.13, we show the behavior of the imaginary action and the projection of the orbits onto the $(\mathrm{Re}\, q, \mathrm{Re}\, p)$ plane, respectively. Several representative initial conditions are chosen from the plot in Fig. 6.10(c). As can be seen in Fig. 6.13(a), the imaginary actions do not remain constant, but increase or decrease monotonically. This behavior is in sharp contrast to that found for the orbits associated with the CRK (see Figs. 6.14 and 6.15). In addition, Fig. 6.13(b) clearly shows that the orbits projected onto the $(\mathrm{Re}\, q, \mathrm{Re}\, p)$ plane obviously deviate from the real KAM curves, since they rotate around the

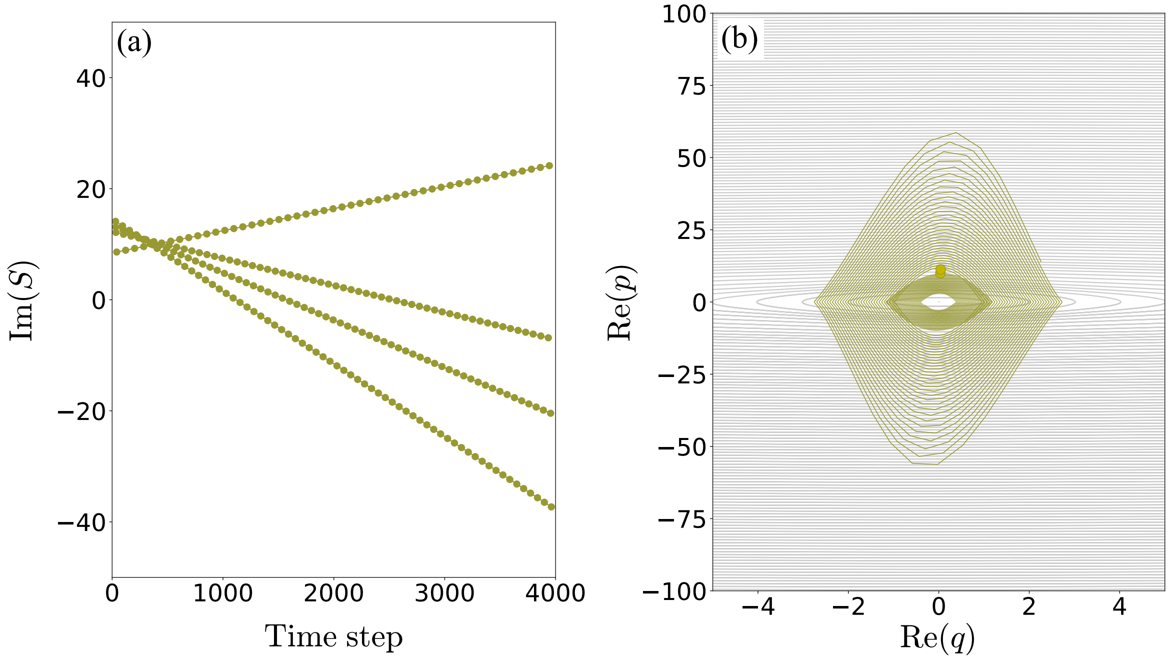

Figure 6.13: (a) The variation of the imaginary action for the case where the initial conditions are chosen from the plot shown in Fig. 6.10(c). The dot is plotted at each time when $\mathrm{Im}\, q_n = 0$ is satisfied. (b) The projection onto the $(\mathrm{Re}\, q, \mathrm{Re}\, p)$ plane of the two of the orbits used to plot (a). One rotates in an outer region, while the other rotates in an inner region. The initial conditions of these two orbits are close to each other and are represented by the dot. The parameters are set to $\tau = 0.01$, $\varepsilon = 1.0$, and $\lambda = 1.2$.

CCK and do not approach the real KAM curves. For these reasons, we can conclude that the orbits associated with the CCK do not need to be taken into account.

As for the orbits starting from the side branches in the hierarchical tree structure, the associated imaginary action is larger than that for the main trunk as shown in Fig. 6.14(a). The imaginary action of the orbit starting from the trunk quickly reaches almost the final value. On the other hand, the imaginary action for the orbit leaving a branch in the hierarchical structure takes a rather small value for a while, then it gives a value that is larger than the imaginary action obtained for the trunk orbit, although its final manifold is almost the same as that for the trunk orbit. This is also due to the fact that higher-order orbits make a detour before reaching the final real KAM curves. As can be seen in Fig. 6.14(b), the former orbit jumps directly to the final manifold, whereas the latter orbit rotates several times before reaching the final manifold. The latter orbit is temporarily trapped by an inner CRK, then it moves to the final manifold. This observation tells us that the relevant complex orbits that dominate the semiclassical propagator (6.17) are the orbits located in the main trunk in the hierarchical structure.

Notice that all the complex orbits do not necessarily contribute to the semiclassical propagator when applying the semiclassical approximation in the complex domain. This is because the so-called Stokes phenomenon occurs when applying the saddle point approximation [100, 101, 102, 103, 104]. A simple example of the Stokes phenomenon can be found in the evaluation of the Airy function using the saddle point method [105]. The Stokes phe-

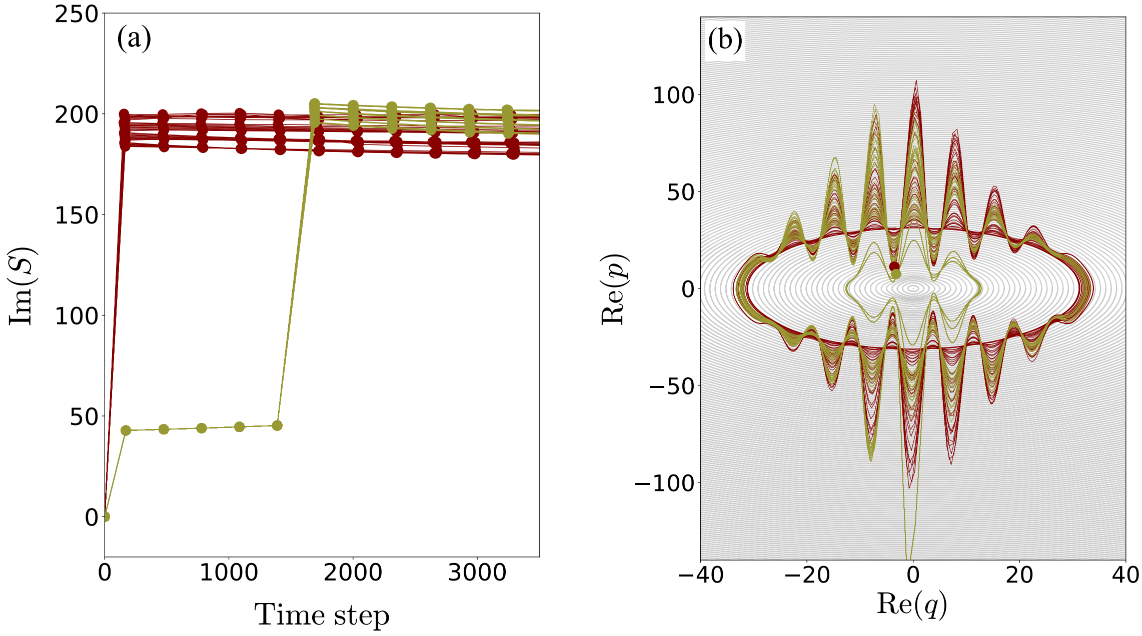

Figure 6.14: (a) The variation of the imaginary action for the case where the initial condition is taken from the main trunk shown in Fig. 6.10(b) (red) and the case where it is taken from a higher order branch shown in Fig. 6.12(a) (yellow). (b) The projection onto the $(\mathrm{Re}p, \mathrm{Re}q)$ plane of the orbits used to plot (a). The red and yellow dots placed around the center of the plot indicate the initial points. Note that the target real KAM curves are almost the same for both cases. The parameters are set to $\tau = 0.01$, $\varepsilon = 1.0$, and $\lambda = 1.2$.

nomenon also occurs when evaluating the multiple integral, but it is by no means trivial how to deal with the Stokes phenomenon for the integral with more than two saddles [106, 107]. This is a central issue in recent developments in resurgent theory, and some attempts have even been made in chaotic systems [22, 69]. However, we do not take such a sophisticated approach here, but simply observe the sign of imaginary action. Such a crude approach is justified by the fact that the complex orbits with negative imaginary actions give exponentially divergent contributions, which should be eliminated when evaluating the exponentially decaying tunneling tail. Therefore, we will treat the problem simply by neglecting the region where the resulting imaginary actions take negative values.

6.4.3 Complex orbits attaining the minimal imaginary action

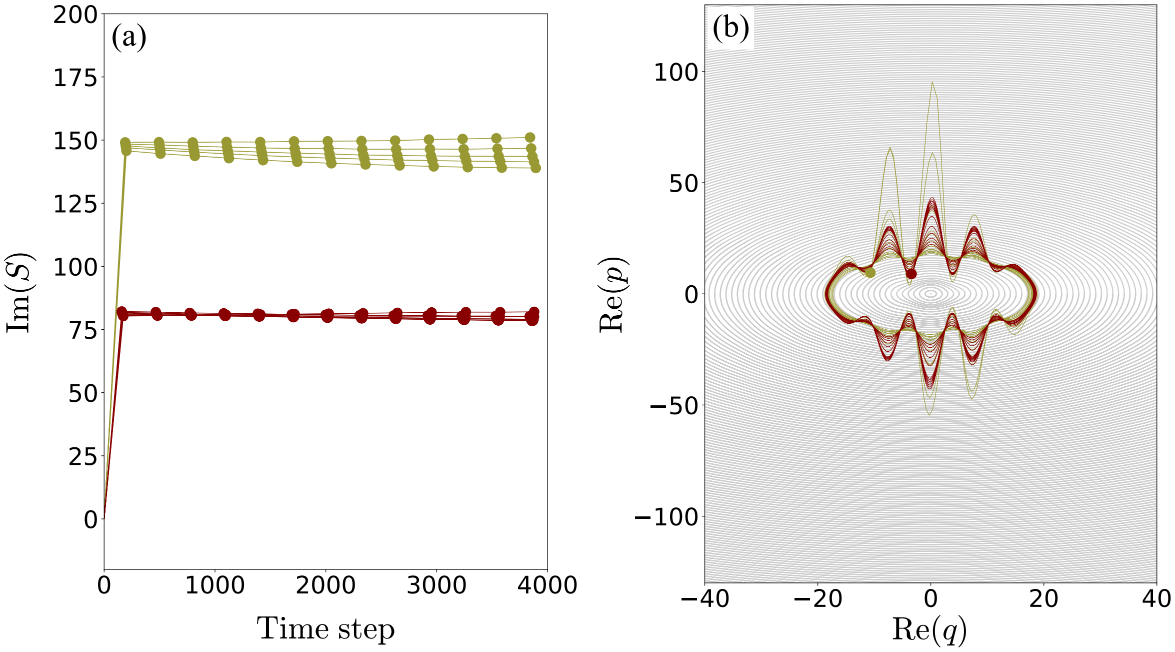

Figure 6.15: (a) The variation of the imaginary action for the cases where the initial conditions are chosen from the main trunk with smaller values of η (red) and larger values of η (yellow). The former is taken from the point in Fig. 6.10(b), while the latter is taken from the point in the blue box in Fig. 6.10(a). So the value of η is smaller in the former case than in the latter. (b) The projection onto the $(\mathrm{Re}\, q, \mathrm{Re}\, p)$ plane of the orbits used to plot (a). Note that the target real KAM curves are almost the same for both cases. The parameters are set to $\tau = 0.01$, $\varepsilon = 1.0$, and $\lambda = 1.2$.

We will further narrow down the candidate complex orbits. As shown in Fig. 6.10, there are not one but many trunks accompanying the hierarchical structure. Among them, the most dominant orbits are determined by the value of η, the depth of the initial position in the (ξ, η)-plane. Such a principle is generally valid not only for ultra-near integrable systems, but also for mixed systems, where chaotic regions are relatively large and visible [20, 27, 67, 68].

As found in [27], the complex orbits departing from the position with smaller η give larger contribution in mixed systems. We have compared the imaginary action along the stable manifold associated with unstable periodic orbits in chaotic regions surrounding the regular region. The reason for focusing on stable manifolds is precisely the fact that $\overline{W^s(\mathfrak{p})} = J^+$ holds. It was also shown in [28] that the complex paths connecting the initial and final manifolds for the propagator are well approximated by the stable manifold over time.

Note, however, that there is an important difference between the situations examined here and in [27]. In the previous case, the complex orbits eventually approach real chaotic seas, while in the present case, the orbits repeat spiral-up and spiral-down motions and keep oscillating in the complex plane, as explained above. Despite this difference, it is common that the orbits with smaller η carry smaller imaginary actions and thus give larger contributions in the semiclassical sum. This can indeed be verified by plotting the imaginary action for the cases with different η. As shown in Fig. 6.15, the orbits leaving a trunk with smaller η gain smaller imaginary actions compared to the cases with larger η, even though the target real KAM curves for both cases are almost the same.

6.4.4 Complex orbits satisfying the boundary conditions

Now that we have information about which orbits have the smallest imaginary action, we examine whether these orbits can explain the step structures found in the time evolution of the wave packet, shown in Section 6.1. Since we consider the propagator in the form (6.17), we have to consider complex orbits whose final q_n is real-valued. We also need to focus on the propagator at each time the condition when the step structure appears in the time evolution. As shown in Fig. 6.6 and discussed in Section 6.1, the step structure appears periodically with

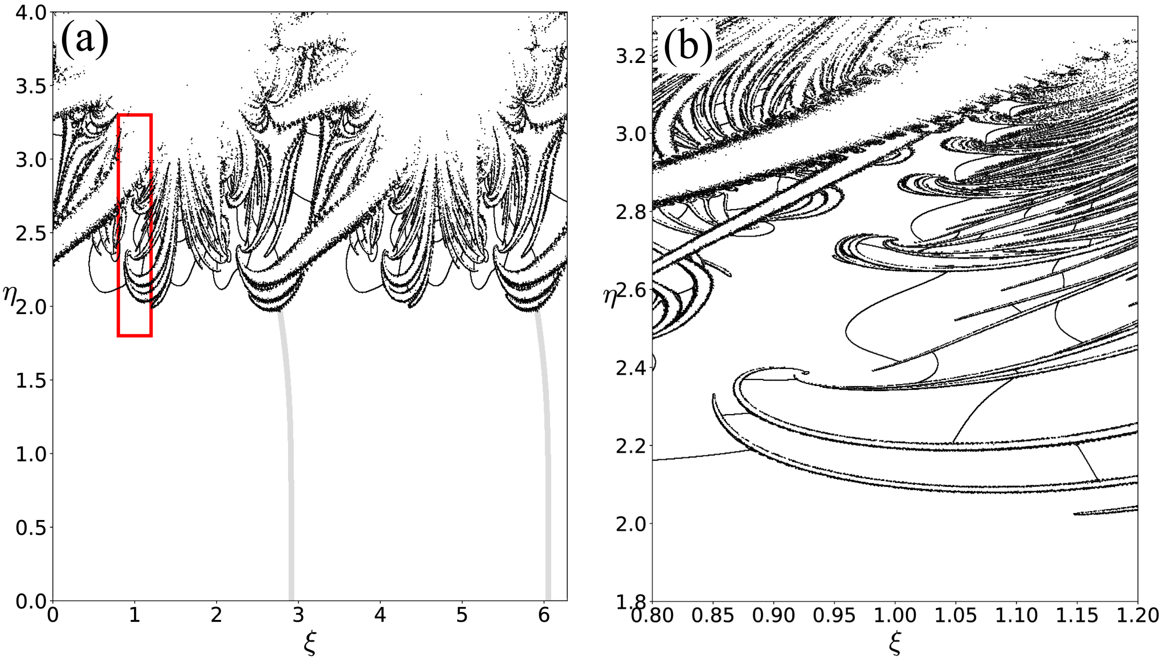

Figure 6.16: The set $\mathscr{M}_N$ defined by (6.24). Plot (b) is a magnification of the area enclosed by the red square in plot (a). The gray curves in plot (a) attached to the ξ-axis are called natural branches [19, 20]. The parameters are set to $\tau = 0.05$, $\varepsilon = 1.0$, and $\lambda = 1.2$.

period $N/2 = E_{\mathrm{ex}}/E_0 = 63$. The factor 1/2 appears because we are looking at the absolute value.

Figure 6.16 plots the set of initial conditions satisfying $\operatorname{Im} q_N = 0$:

$$\mathscr{M}_N = \{\, q_0 = (\xi, \eta) \in \mathbb{C}^2 \,|\, (q_0, p_0) \in \Gamma, \operatorname{Im} q_N = 0 \,\}. \tag{6.24}$$

The plotted region is chosen to contain the region that gives the minimum imaginary action. Each string in Fig. 6.16 represents a single complex orbit satisfying the condition $\operatorname{Im} q_N = 0$. As one moves along each string, the final value Re q_n changes from $-\infty$ to $+\infty$.

Since we are interested in the amplitude of the time-evolved wave function at the position where the underlying real KAM curve supports the eigenstate excited by the resonance condition (6.8), we focus on the orbit satisfying the condition $\operatorname{Re} q_N = q^{\mathrm{t}}$, where q^{t} denotes the coordinate of the turning point obtained by projecting the associated real KAM curves onto the q-axis.

Figure 6.17 shows the variation of $\operatorname{Re} q_n$ and $\operatorname{Im} q_n$ as a function of the time step. As expected, $\operatorname{Im} q_n$ is found to be zero when $\operatorname{Re} q_n$ is almost equal to the position q^{t} of the turning point. This period coincides with the period of oscillation of the step structure of the wave function (see Fig. 6.6). Therefore, it makes sense to evaluate the corresponding imaginary action at each point in time when the periodic oscillation occurs.

Figure 6.18 gives the behavior of $\operatorname{Im} S_n$, for which the two different KAM curves satisfying the resonance condition (6.8) are chosen as the final manifolds. The light blue curve shows the case where the final KAM curve is the support for the first excited state ($m = 1$) in Eq. (6.8)

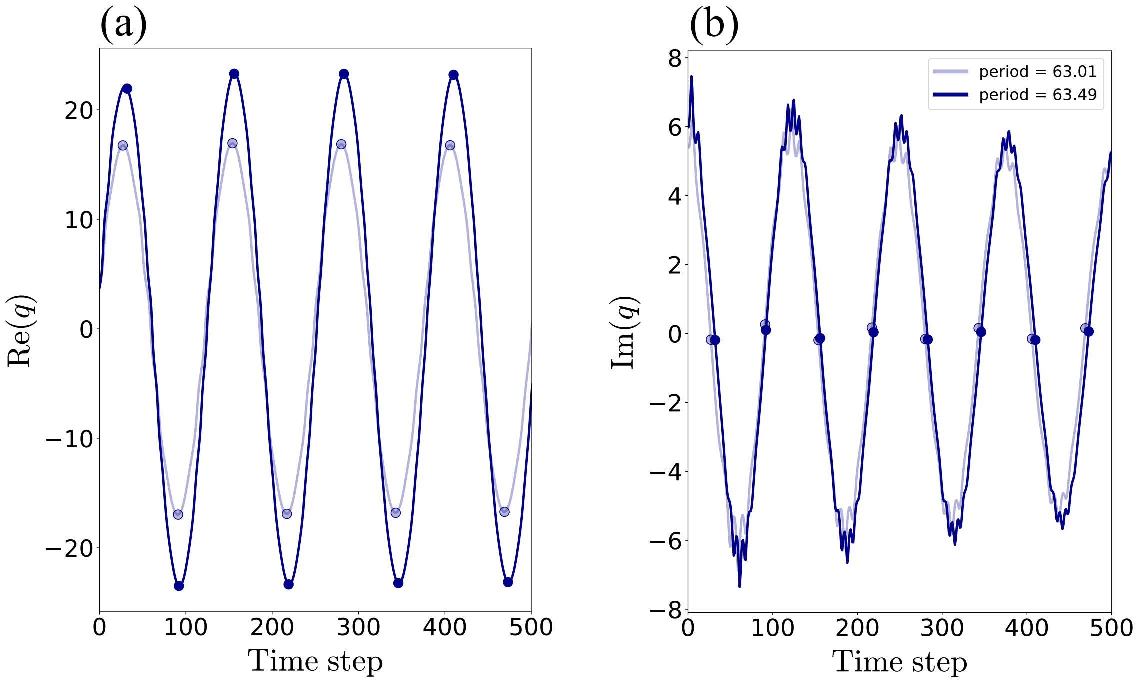

Figure 6.17: The behavior of (a) $\operatorname{Re} q_n$ and (b) $\operatorname{Im} q_n$ for the orbits moving along the CRK. The light blue and dark blue curves show the cases where the orbits move along the CRK associated with the real KAM curve supporting the first resonance state ($m = 1$ in Eq. (6.8)) and the second resonance state ($m = 2$), respectively. The dots in the plot (a) indicate the points when $\operatorname{Im} q_n = 0$ in plot (b). The parameters are set to $\tau = 0.05$, $\varepsilon = 1.0$, and $\lambda = 1.2$.

and the dark blue curve corresponds to the case for the second excited ($m = 2$) state. We can see that, at each time step where $\mathrm{Im}\, q_n = 0$, the value of $\mathrm{Im}\, S_n$ remains almost constant. The behavior of $\mathrm{Im}\, S_n$ is the same in the case where the value of η of the initial position is large (see Fig. 6.15), but the imaginary action thus obtained is larger and makes a smaller contribution, for the reason mentioned above.

As shown in Fig. 6.14, the orbits with larger imaginary action make a detour before reaching the target manifold, while the orbits with the smallest imaginary action jump directly to the final manifold. As shown in Fig. 6.14(a), the variation of $\mathrm{Im}\, S_n$ occurs in a very short time, which means that there is almost no “loss of imaginary action" in the transition process. The wavy pattern of the final manifold appears, as explained in Section 6.3.1, because the iterated orbits are close to the natural boundary. We notice that the initial condition for the orbit with the smallest imaginary action is located around the region where the wavy manifold bends most inward. It is as if the orbit was on the final manifold from the beginning.

We can understand the behavior of the most dominant complex path more clearly by observing the 3D plot. As shown in Fig. 6.19, the most dominant path is located very close to or exactly on the wavy part of the final manifold from the beginning. It shows no detour, but jumps directly to the final manifold. After that it starts to spiral down to the real plane. In other words, the ‘shortest path’ in terms of distance in the complex phase space gives the orbit with the minimal imaginary action, and this would be a principle specifying the most dominant complex path.

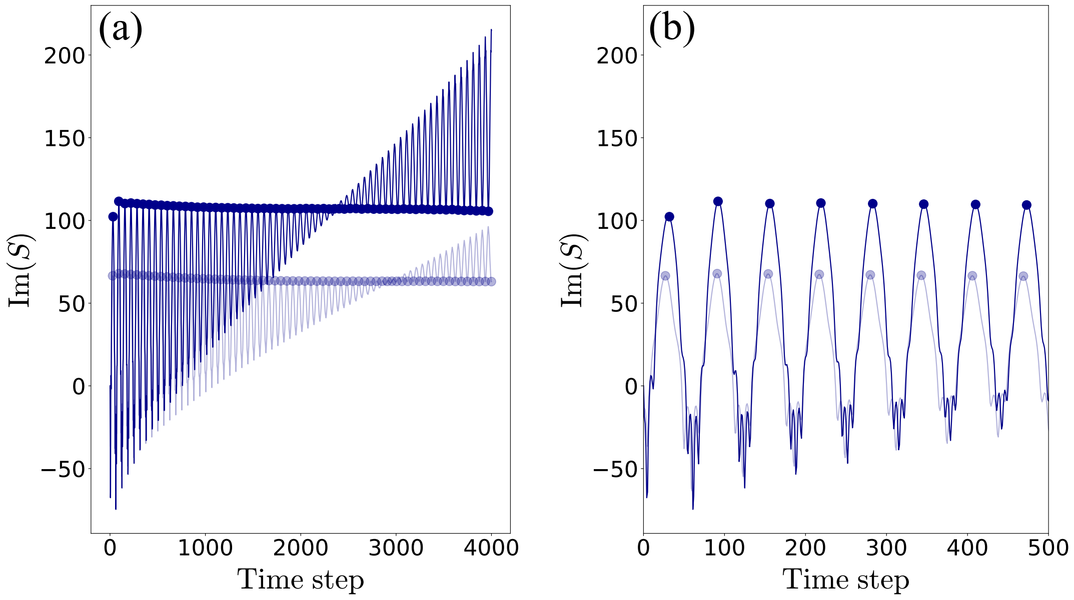

Figure 6.18: The behavior of $\mathrm{Im}\, S_n$ for the orbits moving along the CRK. The light blue and dark blue curves show the cases where the orbits move along the CRK associated with the real KAM curve supporting the first resonance state ($m = 1$ in Eq. (6.8)) and the second resonance state ($m = 2$), respectively. Plot (b) is a magnification of plot (a). The dots indicate the points where the condition $\mathrm{Im}\, q_n = 0$ is satisfied (see Fig. 6.17). The parameters are set to $\tau = 0.05$, $\varepsilon = 1.0$, and $\lambda = 1.2$.

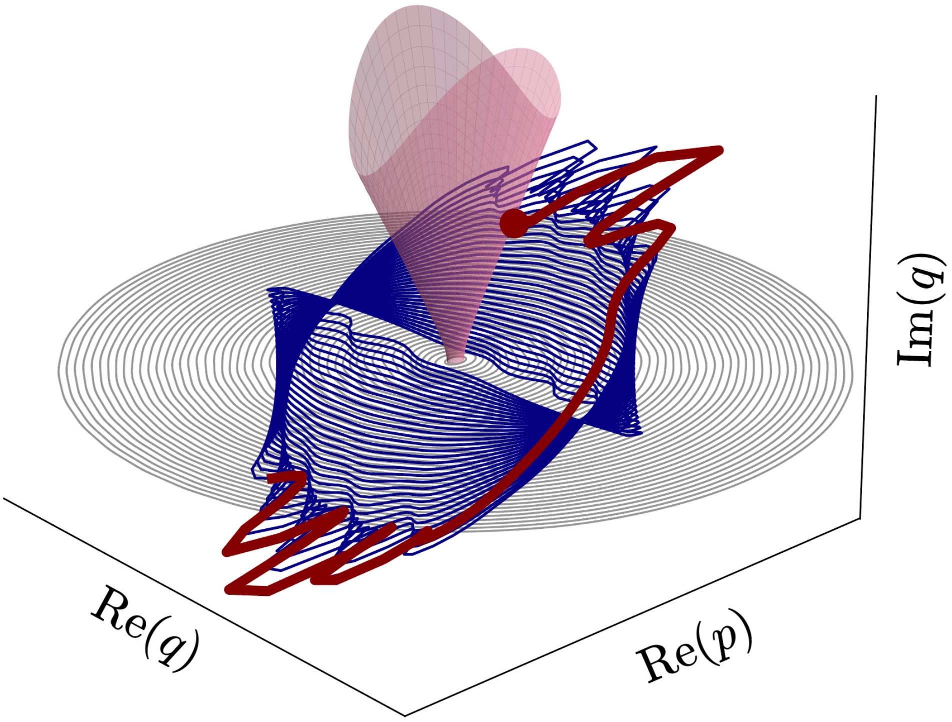

Figure 6.19: Illustration of the complex path with the minimal imaginary action. The pink bottle-shaped manifold represents the initial manifold Γ. The red curve shows the complex path with the minimal imaginary action, which jumps to the final manifold colored in blue. The wavy pattern indicates that the CRK is close to its natural boundary. The complex path is captured by such a wavy part of the final manifold.

Figure 6.20 shows that the minimal imaginary action $\mathrm{Im}\, S$, evaluated according to the principle described above, reasonably well reproduces the squared magnitude $|\mathrm{Con}_k^{(M)}(q)|^2 = \left|\left\langle q \middle| \Phi_k^{(M)} \right\rangle \left\langle \Phi_k^{(M)} \middle| \Psi_0 \right\rangle\right|^2$ in the sum (6.9). The reason why the semiclassical prediction quantitatively overestimates the quantum calculation would be that we have given a rough estimate only using the imaginary action, without including the amplitude factor here. Another reason, which must be a major one, is that our initial condition $|\psi_0\rangle$ and the associated classical initial manifold Γ is too crude to approximate the ground state $|\Psi_0\rangle$. As found in Fig. 6.1, the classical invariant circles are deformed from the set of ellipsoidal curves Γ due to the second term in (6.1), so the support of the minimal wave packet does not approximate the underlying invariant curve supporting the ground state of the quantum map.

As can be seen in Fig. 6.2(a), the grand state wave function $|\langle q|\Psi_0\rangle|^2$ of the quantum map coincides with that of the truncated quantum BCH Hamiltonian $\hat{H}_{q\mathrm{BCH}}^{(M)}$ up to the first plateau. Recall that the part up to the first plateau could be reproduced by the branches that are connected to the ξ-axis, shown by gray curves in Fig. 6.16. These branches are called *natural branches* in Refs. [19, 20]. The points connected to the ξ-axis correspond to the turning points of the KAM curves in the real plane. The natural branches are the complex paths that already exist in the integrable limit, so they can be regarded as an analog of the instanton. The result shown in Fig. 6.20 implies that, up to the first step, the complex orbits other than the natural branches

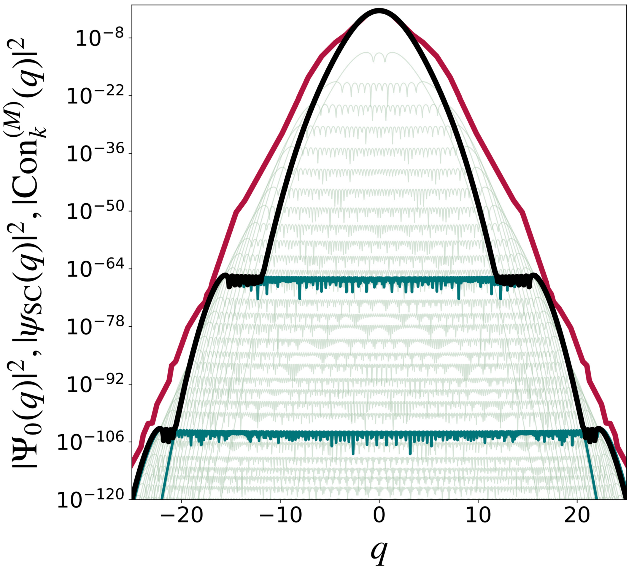

Figure 6.20: Ground state eigenfunction $|\langle q|\Psi_0\rangle|^2$ (black). Squared magnitudes $|\mathrm{Con}_k^{(M)}(q)|^2 = \left|\left\langle q\middle|\Phi_k^{(M)}\right\rangle\left\langle\Phi_k^{(M)}\middle|\Psi_0\right\rangle\right|^2$ in the sum (6.9) (light green). The resonance states $k = 125$ and $k = 251$ are shown in dark green, respectively. The red curve shows $|\psi_{\mathrm{sc}}(q)|^2 := \exp(-2|\mathrm{Im}\,S|/\hbar)$, where $\mathrm{Im}\,S$ is the minimal imaginary action evaluated according to the principle given in the text. The parameters are set to $\hbar = 1$, $\tau = 0.05$, $\varepsilon = 1.0$, and $\lambda = 1.2$.

do not manifest themselves in the amplitude of the wave function, although they have smaller imaginary actions. This must be due to the fact that the real actions $\mathrm{Re}\,S$ of these orbits are random and cancel each other out.

On the other hand, at the plateau energy for which the resonance condition (6.8) is satisfied, the complex orbits contribute coherently due to the constructive interference, which will be explained in Section 6.5. The decay after the plateau, similar to the initial decay curve described by the natural branches, would be associated with the natural branches connected to the KAM curve supporting the first resonance state ($m = 1$).

The most important result would be that the minimal imaginary action $\mathrm{Im}\,S$ always takes lower values than the instanton action represented by the natural branches. This means that the enhancement of the tunneling probabilities occurs precisely because the transport is driven by the orbit in the Julia set. So far, the origin of the enhancement of tunneling probability in non-integrable systems has been sought in several ways, but the description in the paper [108] is the first time, to the author's knowledge, that its direct origin has been pointed out.

6.4.5 $\hbar$-dependence of the step height

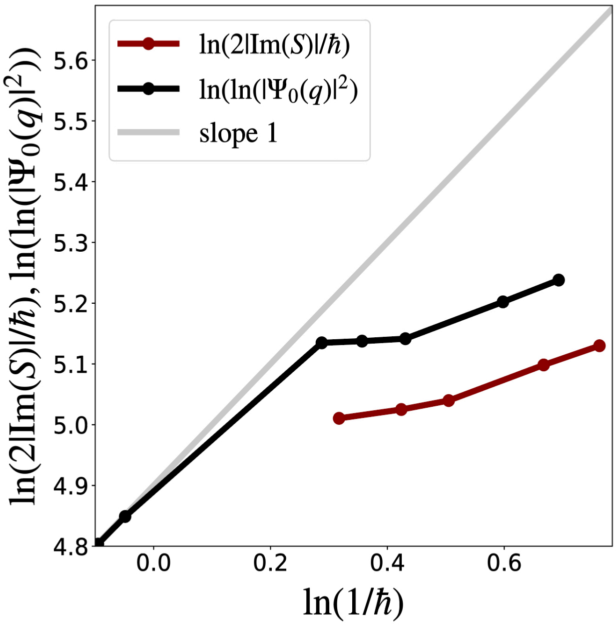

Figure 6.21: The black curve shows the ground state eigenfunction for the quantum map (3.21) and the red curve is obtained by the smallest imaginary action $\mathrm{Im}\, S$ (see text). The line with slope 1 is added for reference. The parameters are set to $\tau = 0.05$, $\varepsilon = 1.0$, and $\lambda = 1.2$.

We now recall that the position and height of the steps move as a function of $\hbar$, as shown in Fig. 6.4. The step appears on the KAM curve supporting the eigenstates that satisfy the resonance condition (6.8), so we can specify the $\hbar$-dependence of the step position. On the other hand, the dependence of the step height on $\hbar$ is not trivial. In fact, as demonstrated in the inset of Fig. 6.4, the stretched exponential growth appears when evaluating the step height at a fixed q as a function of $\hbar$. This behavior is quite anomalous since one normally expects an exponential dependence in the tunneling tail.

Our semiclassical calculation qualitatively predicts this stretched exponential dependence well, as shown in Fig. 6.21. The reason for the quantitative discrepancy between the semiclassical and quantum calculations is the same as mentioned above. As the value of $\hbar$ increases, the KAM curve satisfying the resonance condition shifts outward. Correspondingly, the complex orbits necessary to describe the transition should reach outer KAM curves, so the associated imaginary action becomes larger. However, we have to divide the imaginary action by $\hbar$ to calculate an individual semiclassical contribution of the form $\exp\left(-\mathrm{Im}\, S_\gamma/\hbar\right)$. Thus, $\mathrm{Im}\, S_\gamma$ increases with increase of $\hbar$, while the denominator is simply proportional to $\hbar$, so that a subtle balance arises from the competition between the denominator and the numerator in the imaginary phase $-\mathrm{Im}\, S_\gamma/\hbar$. Our result shows that the resulting $\hbar$-dependence is stretched exponential, which is consistent with exact quantum calculations.

This stretched exponential dependence predicts a non-trivial nature in the complex classical dynamics. The above result shows that

$$\exp\left[-\mathrm{Im}\ S(I_0, I)/\hbar\right] \sim \exp\left(-\hbar^{-\mu}\right), \tag{6.25}$$

where $\mu \approx 0.275$ is numerically estimated. Here I_0 and I denote initial and final actions, respectively. Assuming the classical quantization condition $I_0 = n_0\hbar$ and $I = n\hbar$ for the initial and final KAM curve, and also focusing on the decay of the height on a certain fixed plateau, meaning that $n - n_0$ is fixed, the above $\hbar$ dependence holds if

$$\mathrm{Im}\ S(I_0, I) \sim (I - I_0)^{(\mu-1)} \tag{6.26}$$

is satisfied. This is a relation that should hold in order to understand the observed phenomenon in the tunneling tail. This relation is purely classical, so it should be derived from the property of complex classical dynamics. This task is left for future investigation.

6.4.6 λ-dependence of the step structure

As shown in Fig. 6.2, the step structure appears in the tunneling tail for a smaller λ case, while it is hidden in the tail of the grand state contribution for a larger λ case. The result given in Fig. 6.20 implies that this is due to the fact that the minimal imaginary action for the former case is smaller than that for the latter case. Since the smaller the value of η in the initial value plane (ξ, η), the smaller the imaginary action is, as discussed above, we can expect that the orbits with the minimal imaginary action for the smaller λ case will be found in a smaller η region in the (ξ, η) plane compared to the larger λ case.

The validity of such a prediction is almost confirmed by plotting the set K^+ in the (ξ, η) plane. The colors in Fig. 6.22 show the number of time steps until the orbits leaving each point in the (ξ, η) plane are out of a properly chosen finite sized box. Such a plot is expected to approximate the set K^+, as done in Fig. 6.9(a).

The boundary between the red and blue regions roughly indicates the natural boundary of the KAM curve supporting the ground states. Recall that our initial value curve Γ is determined to approximate such a supporting KAM curve. Since the orbits with the minimal imaginary action are close to the natural boundary, the comparison between Figs. 6.22(a) and (b) would lead to the prediction that the minimal imaginary action for the $\lambda = 1.2$ case is smaller than that for the $\lambda = 3.0$ case. This qualitatively explains the difference between Figs. 6.2(a) and (b).

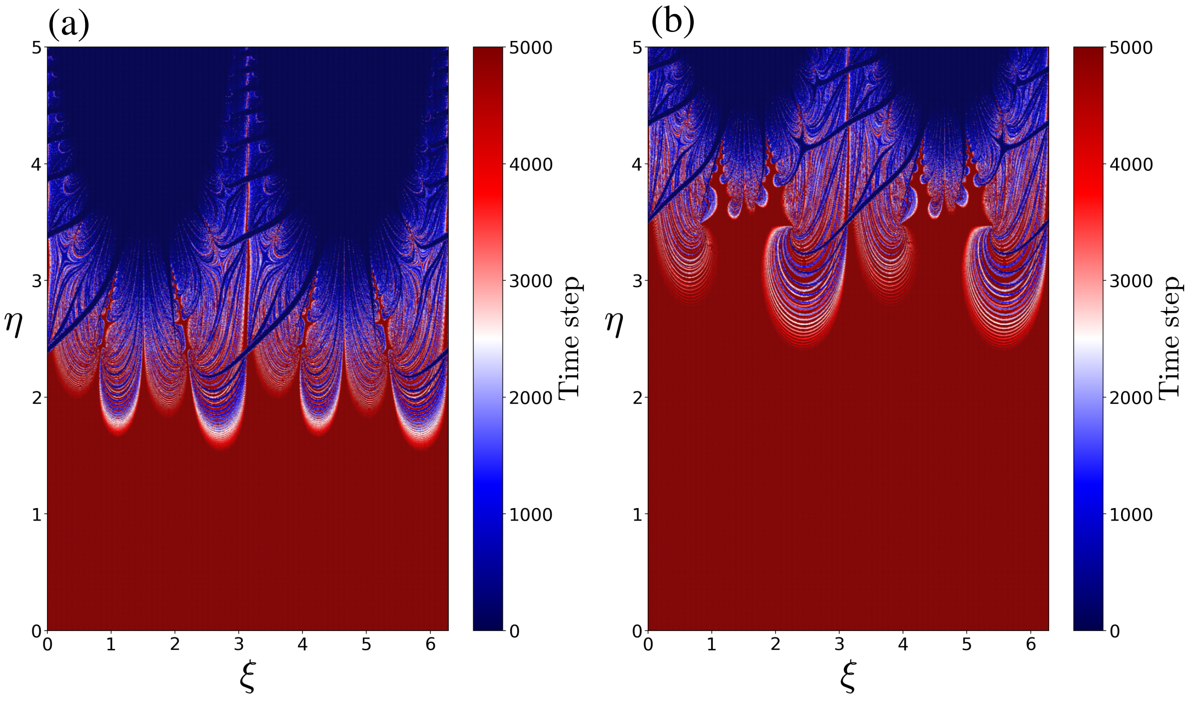

Figure 6.22: The initial value plane (ξ,η), in which each color is assigned to reflect the number of time steps until the orbits leaving each point in the (ξ,η) plane leave a properly chosen finite-size box. The red regions show the set of initial points that remain in the finite region for a sufficiently long time, while the orbits in the blue region diverge to infinity within a short time. (a) $\lambda = 1.2$. (b) $\lambda = 3.0$. The parameters are set to $\tau = 0.01$, $\varepsilon = 1.0$.

6.5 Real action of complex paths and quantum resonances

As shown in Fig. 6.4, the step structure shifts with the change of the Planck constant $\hbar$. This $\hbar$-dependence is explained by the fact that the step structure is caused by the quantum resonance. We can see the resonance in the plot of $\left|\left\langle\Psi_k^{(M)}\middle|\Psi_0\right\rangle\right|^2$ (see Fig. 6.5(a)). Small peaks found in the plot are responsible for creating the step structure in the plot of $\left|\langle q|\Psi_0\rangle\right|^2$ (see also Fig. 6.5(b)). Here we try to give a semiclassical understanding of this quantum resonance phenomenon.

Since the eigenfunction $\left|\left\langle\Psi_k^{(M)}\middle|\Psi_0\right\rangle\right|^2$ is not directly accessible in the energy-domain semiclassical analysis, we consider the problem again from the time domain. Below we use the notation $|E\rangle$ instead of $|\Psi\rangle$ in order to represent the eigenstate of the integrable approximation.

For simplicity, we assume that the complex orbit with the minimal imaginary action is unique.

In this case, the semiclassical propagator can be expressed as

$$\begin{aligned}\langle E|\hat{U}^n|E_0\rangle &\simeq \sum_\gamma A_\gamma \exp\left(\frac{\mathrm{i}}{\hbar}S_\gamma(E,E_0)\right)\\ &= \sum_\gamma A_\gamma \exp\left(\frac{\mathrm{i}}{\hbar}\left(S'_\gamma(E,E_0)+\mathrm{i}S''_\gamma(E,E_0)\right)\right)\\ &\simeq A_{\gamma_{\min}}\exp\left(-\frac{1}{\hbar}S''_{\gamma_{\min}}(E,E_0)\right)\exp\left(\frac{\mathrm{i}}{\hbar}\left(S'_{\gamma_{\min}}(E,E_0)\right)\right), \qquad (6.27)\end{aligned}$$

where $S_\gamma(E,E_0)$ denotes the classical action of the orbit γ, which connects the initial state $|E_0\rangle$ and the final state $|E\rangle$, and A_γ the associated amplitude factor. The initial and final states are assumed to be the eigenstates of the Hamiltonian $H^{(1)}_{\mathrm{BCH}}$. $S'_\gamma(E,E_0)$ and $S''_\gamma(E,E_0)$ are the real and imaginary part of the action, respectively, and $\gamma_{\min}$ represents the complex orbit with the minimal imaginary action.

Let ω be the angular frequency of the KAM curve supporting the states $|E\rangle$. We can assume that the number of time steps during which the orbit travels along the associated KAM circle is

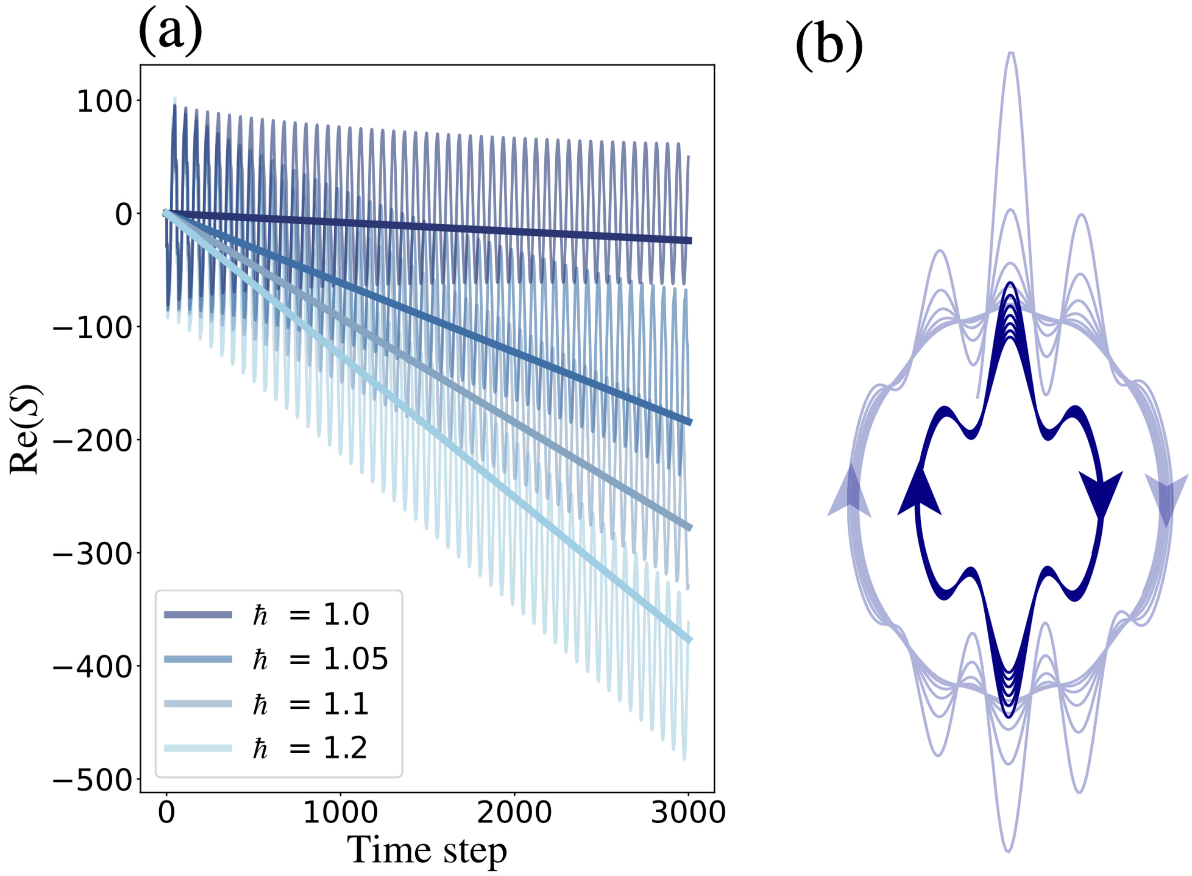

Figure 6.23: (a) The behavior of the real action as a function of time step for different values of $\hbar$. The straight line is obtained by applying the formula (6.32). (b) Schematic illustration showing the direction of rotation on different CRK curves.

N, where N is the period of oscillation of the quantum wave packet. Since $\tau \ll 1$ is assumed, we can approximate the discrete-time dynamics by the flow of the continuous Hamiltonian $H^{(1)}_{\mathrm{BCH}}$. Using the relation $\omega : \Omega = 1 : N$, the period T of one cycle for the flow system is given by $T = N\tau = 2\pi/\omega$. The classical action for one cycle

$$S(E) = \sum_{j=1}^{N} \Big((q_j - q_{j-1})\, p_j - \tau \left(T(p_{j+1}) + V(q_j) \right), \Big) \tag{6.28}$$

admits the continuous approximation,

$$\begin{aligned} \widetilde{S}(E) &= \oint_E p dq - \int_0^{\frac{2\pi}{\omega}} (T(p) + V(q))\, dt \\ &= 2\pi \left(I(E) - E/\omega \right) \\ &= \frac{2\pi N}{\Omega} (I(E)\omega - E). \end{aligned} \tag{6.29}$$

Here the action integral for one cycle

$$I(E) = \frac{1}{2\pi} \oint_E p dq, \tag{6.30}$$

is introduced.

In the following, the number of iterations will be counted in unit of one cycle over each KAM curve. Under such a count, the amount of action gained in a cycle is given by

$$S_{\mathrm{cycle}}(E) := \widetilde{S}(E)/N = \frac{2\pi}{\Omega} \left(I(E)\omega - E \right). \tag{6.31}$$

As shown in Fig. 6.23, the real action increases while oscillating periodically in time, and we can confirm that the slope of the points taken at each period of oscillation follows the above formula (6.31).

Now suppose that the orbit, initially located on the manifold given by $H^{(1)}_{\mathrm{BCH}} = E_0$, rotates around it ℓ-times. Then it moves to another manifold $H^{(1)}_{\mathrm{BCH}} = E$ and rotates around it also ℓ-times. We can assume the existence of such an orbit due to the ergodicity of the dynamics in the complex plane. The action gained in the course of such an itinerary should be

$$S'_{\gamma_{\min}}(E, E_0) \simeq \ell S_{\mathrm{cycle}}(E) - \ell S_{\mathrm{cycle}}(E_0) = \frac{2\pi\ell}{\Omega} \Big((I(E)\omega - E)) - (I(E_0)\omega_0 - E_0) \Big). \tag{6.32}$$

Here we have neglected the real action contribution gained in the transition process from the initial manifold to the target manifold. This is justified by the fact that the orbit with the minimal action jumps almost instantaneously from the initial manifold to the final manifold. The minus sign in front of the second term is necessary because the orbit rotates in the same direction on both manifolds (see the illustration in Fig. 6.23(b)) .

We then recall the quantum resonance condition (6.8), which implies that

$$I(E)\omega - I(E_0)\omega_0 = m\hbar\Omega. \qquad (m \in \mathbb{N}) \tag{6.33}$$

Here we assumed the Bohr-Sommerfeld quantization condition on each KAM curve.

Using the expression (6.32) together with (6.33), we find that

$$\lim_{n\to\infty}\langle E|\hat{U}^n|E_0\rangle \simeq A_{\gamma_{\min}} \exp\left(-\frac{1}{\hbar}S''_{\gamma_{\min}}(E,E_0)\right)\sum_{\ell=1}^{\infty}\exp\left(-\frac{\mathrm{i}}{\hbar}\frac{2\pi\ell}{\Omega}(E-E_0)\right).$$

Since we are looking for the nature of the eigenfunction shown in Fig. 6.2, we include the iteration in the backward direction so that the sum should go from $\ell=-\infty$ to ∞. Applying the Poisson sum formula, we obtain that

$$\lim_{n\to\infty}\langle E|\hat{U}^n|E_0\rangle \simeq \hbar\Omega A_{\gamma_{\min}} \exp\left(-\frac{1}{\hbar}S''_{\gamma_{\min}}(E,E_0)\right)\sum_{n=-\infty}^{\infty}\delta(E-\hbar\Omega n). \tag{6.34}$$

The final expression is consistent with the observation made in Fig. 6.5(a). The mechanism that produces a series of peaks in the plot of $\left|\left\langle \Psi_n^{(M)}\middle|\Psi_0\right\rangle\right|^2$ is explained by constructive interference of the complex orbit going back and forth between the initial and final manifolds.

Finally, we examine the validity of our assumptions. First, we have considered only a single orbit, while other complex orbits with imaginary actions comparable to the minimal imaginary action may come into play. This is very likely because the orbits are dense in the Julia set J. In every neighborhood of the orbit found to have the minimal imaginary action, there would be other complex orbits with almost the same imaginary action. If this is the case, we need to consider the initial phase differences between equally weighted orbits. There is no a priori information about such relative phases, but as shown in Fig.6.10, it would be plausible to assume that there are correlations between orbits leaving different spots in the initial value plane (ξ,η). If the relative phases are completely random, the above scenario will not work because a sequence of delta functions in (6.34) will be killed by the random phase.

Another assumption is that we have only considered the repetition of the same number of rotations in both the initial and final manifolds. This may be somewhat artificial, but a core part of the argument is the constructive interference that occurs in both manifolds. Thus, we believe that the idea will essentially survive, even if explicit treatments become elaborate.

Chapter 7

Conclusion

In this thesis, we have investigated quantum tunneling in non-integrable systems based on the complex semiclassical theory in the time domain. We first analyzed the case of mixed systems, where structure such as chaotic regions, nonlinear resonances etc. arising from non-integrability are visible in phase space. According to the results of complex dynamical systems, the set of complex orbits contributing to the semiclassical propagator are approximated by the complex stable manifolds for the periodic orbits in the real plane [28]. However, there are infinitely many periodic orbits in the real plane, so the candidate complex orbits that could contribute to the semiclassical propagator are infinitely many as well. One of the purposes of this thesis was to specify the complex orbits that could provide the most dominant contribution to the semiclassical propagator out of such candidates associated with complex stable manifolds, and characterize their dynamical properties. To this end, we have developed an algorithm to find the intersection points of the complex stable manifold supporting the quantum wavepacket and the initial manifold, and then compared the magnitude of the imaginary part of the action associated with the complex orbits transporting along the complex stable manifolds [27]. The results reveal that the orbits tending to the sticky zone of the KAM region provide the most dominant contribution in the semiclassical sum.

This is consistent with the result of Frischat and Doron [81, 82], They developed a hybrid semiclassical approach that combines classical and quantum dynamics, and showed the transport passing through the so-called beach state, chaotic states attached to the KAM regions, dominates the tunneling process from regular to chaotic regions. It is worth emphasizing that we find the behavior of the most dominant orbits is affected by the presence of chaos in the complex plane, which is an aspect far beyond the scope of dynamics in the real plane.

The instanton approximation has been a widely used approach to construct the semiclassical theory of tunneling [109]. The instanton path bridges the regions that are not connected by classical dynamics in the real plane, but the connection can be achieved only if the two regions have the same energy. This is a major obstacle when applying the instanton method to non-integrable systems. In non-integrable systems, instantons are broken up by the natural boundary of the complex KAM tori. Consequently, it is not possible to discuss tunneling effects in non-integrable systems with instantons. This is the case even in the ultra-near integrable system, where visible invariant structures arising from the non-integrability of the system do not appear. It has been found that non-trivial staircase structures appear in tunneling tails of wave functions

[4]. The mechanism can be explained simply using quantum mechanics; the quantum resonance between the lower energy and the excited state via the external field occurs. On the other hand, the semiclassical interpretation is less easy to find. In this thesis, we have again performed the semiclassical analysis to search for the origin of non-trivial step structures observed in ultra-near integrable systems [108]. Although the real phase space of the ultra-near integrable system is well controlled, it is not easy to perform the full semiclassical calculation in the time domain. Here we have focused on the principle of finding the complex orbits with minimal imaginary actions that dominate the tunneling transition for given initial and final states, and also explore the underlying mechanism that creates the staircase structure observed in the tunneling tails.

To this end, we first classify the types of complex orbits that appear in the complex space and narrow down the candidate complex orbits that dominate the transition between given states. Since complex orbits belonging to the filled Julia set K^+, which is assumed to coincide with the Julia set J^+, spend most of their time rotating around the complex KAM curves, it would be reasonable to classify the orbits according to whether they move along the set of complex KAM curves obtained by analytically continuing the KAM curves in the real plane, or along the set of complex KAM curves associated with the KAM curves in the complex plane. It was immediately found that the latter type should be excluded from the candidates, since additional imaginary actions are gained in the course of the transition. The next task was thus to sort out the complex paths with minimal imaginary actions out of the former type of orbits. Again, our working hypothesis is to specify complex paths with the minimum itinerary length, i.e. a path without detours. A hint to find such orbits is a hierarchical structure hidden in the Julia set. The complex orbits found under such a principle indeed turn out to have minimal actions. It should be noted that the ergodicity of the dynamics in the complex plane, which was proved by Bedford and Smillie to hold in the Julia set for a class of polynomial maps and confirmed here numerically for the map with transcendental functions, plays a central role. The stretched exponential scaling with respect to $\hbar$ found in tunneling tails of ultra-near-integrable systems can also be reproduced by the minimal imaginary action.

Another important issue in the semiclassical analysis is the interference between complex orbits. The staircase structure observed in ultra-near integrable systems can be explained by the quantum mechanics. This strongly suggests that the interference mechanism works between complex orbits, and the role of real actions should thus be taken into account. In this regard, we have proposed a possible scenario explaining the quantum resonance in terms of interference between complex orbits.

Our claim throughout this thesis is that the Julia set is an alternative to the instanton path, and the ergodicity in the Julia set ensures the tunneling coupling between arbitrarily separated regions in the real classical phase space. One can reach everywhere via the orbits in the Julia set, and the transition between arbitrarily disconnected regions in the real phase space is possible via the complex space. One may even say that quantum tunneling in non-integrable systems is a manifestation of the ergodicity of classical dynamics in the complex plane. Complex dynamical systems have so far been studied purely out of mathematical interest. As a result, physicists have been unaware of recent advances, especially in the topics discussed in this thesis. However, for the reason explained here, the complex dynamical system would be an indispensable tool for understanding quantum tunneling in non-integrable systems.

Acknowledgements

I am grateful to my supervisor Professor Akira Shudo for his advices and all aspects of his helping during the course of Ph.D student. I also would like to thank Professor T. Harayama, Professor T. Hotta and Professor T. Hyodo for careful reading of this thesis.

I would like to thank present members of Nonlinear Physics Group, Mr. K. Fujioka, Mr. Iizuka, Mr. D. Gima, Ms. M. Nakamura, Mr. H. Iwakura, Mr. K. Watanabe, Ms. C. Akimoto and Mr. Y. Sodeno for discussions. Especially, I am grateful to Dr. A. Tanaka for his advice on seminar and support for research activities. I also would like to thank the past members of Professor Shudo's lab group, especially, Mr. K. Yoshida, Mr. H. Yoshino, Mr. R. Kogawa, Mr. M. Nakahama, Mr. Y. Nakahara, Mr. R. Iijima, Mr. M. Ohshika, Mr. T. Iida, Mr. T. Kogure, Mr. S. Teramoto and Mr. R. Ando.

I would like to thank Professor K. S. Ikeda, Professor H. Ito, Professor Y. Ishii, Professor H. Mori and Dr. H. Otsuka for their advices. Especially I thank Dr. Y. Hanada for his helpful comments and fruitful discussion on tunneling.

Finally, I am especially thankful to my family for constant support and encouragement.

Appendix A

Exploration of periodic points and numerical methods

This section explains how to find periodic points in the mixed phase space in order, starting with the shortest periodic orbit. In order to do that, the Newton method could be used as an algorithm, but depending on a periodic point, it may happen that the iteration diverges immediately unless the associated initial point should be taken very close to the periodic point. Unless we know approximately where they are in advance, it may be challenging to calculate all periodic points using the Newton. On the other hand, there is a method called the SD (Schmelcher-Diakonos) method [77, 110] for obtaining periodic points but the SD method converges more slowly than the Newton method and is not suitable for obtaining many periodic points. In the following, the DL (Davidchack-Lai) method [76, 111, 112], which is a hybrid of the Newton and SD methods, is explained: by using the DL method, periodic points can be obtained globally in a shorter calculation time than by using the SD method.

A.1 Newton method

In this section, the Newton method is briefly explained. Let M be $\mathbb{R}^N (N \in \mathbb{N})$. In the following, we aim to find a period orbit $\boldsymbol{x}^*$ with period m, i.e. $\boldsymbol{x}^* \in M \; s.t. \; f^m(\boldsymbol{x}^*) - \boldsymbol{x}^* = \boldsymbol{x}_0 \;\; (m \in \mathbb{N})$ for the dynamical system $f: M \to M$. Let $g(\boldsymbol{x}) = f^m(\boldsymbol{x}) - \boldsymbol{x}$. Then $g'(\boldsymbol{x}) = (f^m)'(\boldsymbol{x}) - I$ where I is the identity matrix. First, let $N = 1$ and consider the Newton method in one dimension. Let M be $\mathbb{R}$. Starting from a suitable initial condition x_0, draw the tangent line about $g(x)$ at $x = x_0$. Find the intersection of this tangent line with the x-axis and let this point be x_1. Draw the tangent line for $g(x)$ again at $x = x_1$, and find the intersection of the tangent line and the x-axis. Denote this point by x_2. By repeating this, a point sequence $\{x_i\}_{i=0}^{\infty}$ is obtained. The process mentioned above is expressed by the formula below.

$$x_{i+1} = x_i - \frac{g(x_i)}{g'(x_i)}. \tag{A.1}$$

If the point sequence $\{x_i\}_{i=0}^{\infty}$ converges, a period orbit x^* with period m is obtained, i.e. as

$i \to \infty$. Here, we extend this procedure to N-dimension. Expand $g(\boldsymbol{x})$ around $\boldsymbol{x}_i$.

$$g(\boldsymbol{x}) \simeq g(\boldsymbol{x}_i) + J(\boldsymbol{x}_i)(\boldsymbol{x} - \boldsymbol{x}_i), \tag{A.2}$$

where,

$$J(\boldsymbol{x}) = \frac{\partial g}{\partial \boldsymbol{x}}, \tag{A.3}$$

which represents the Jacobian matrix of $g(\boldsymbol{x})$. Consider an $N-1$-dimensional hyperplane $S(\boldsymbol{x})$ in $\boldsymbol{x}_i$ as in the 1-dimension.

$$S(\boldsymbol{x}) = g(\boldsymbol{x}_i) + J(\boldsymbol{x}_i)(\boldsymbol{x} - \boldsymbol{x}_i). \tag{A.4}$$

Let $\boldsymbol{x}$ satisfying $S(\boldsymbol{x}) = 0$ be $\boldsymbol{x}_{i+1}$ and introduce a recursion equation.

$$F : \boldsymbol{x}_{i+1} = \boldsymbol{x}_i - J^{-1}(\boldsymbol{x}_i) g(\boldsymbol{x}_i). \tag{A.5}$$

For the point sequence $\{\boldsymbol{x}_i\}_{i=0}^{\infty}$ obtained by the Newton method to converge, the initial conditions must be chosen close to the target periodic point. The concrete algorithm is given as follows:

1. Take the initial condition $\boldsymbol{x}_0$.
2. Repeat F to obtain the point sequence $\{\boldsymbol{x}_i\}_{i=0}^{\infty}$.
3. If the point sequence converges, the positions of the periodic points are obtained. Then, the map f is repeated $m-1$ times and the position information of each point is stored. If the point sequence diverges, repeat the above with different initial conditions.

A.2 SD method

The SD method [77] is another numerical methods to search for periodic points, similar to the Newton method. The Newton method does not converge to the periodic point and diverges even if the equation (A.5) is used repeatedly if the initial values are not chosen appropriately. On the other hand, the SD method, unlike the Newton method, can converge to the periodic point even if we roughly choose initial value by changing the stability of the periodic point as explained below. In the SD method, we first consider the following map F: $\mathbb{R}^n \to \mathbb{R}^n$.

$$F : \boldsymbol{x}_{i+1} = f(\boldsymbol{x}_i). \tag{A.6}$$

Now consider a new mapping system $\overline{F_k}$ such that

$$\overline{F_k} : \boldsymbol{x}_{i+1} = \boldsymbol{x}_i + hC_k(f^m(\boldsymbol{x}_i) - \boldsymbol{x}_i), \tag{A.7}$$

where m is a positive integer. Here, $\{C_k\}_{k=1}^{2^N N!}$ is called the stabilisation matrix, which changes the stability of the periodic points in the system F. The C_k satisfies $C^2 = 1$. Furthermore, it is a matrix such that one component of each row and column is ± 1 and all the other components are 0. If C_k is N-dimensional, there exist $2^N N!$ possible patterns for C_k of type $k = 1, \ldots, 2^N N!$. The parameter h is a small quantity representing the size of the steps of the mapping. The maps F and $\overline{F_k}$ have periodic points at the same position $\boldsymbol{x}^*$ $s.t.$ $\boldsymbol{x}^* = f^m(\boldsymbol{x}^*)$, but the stability of the system F with respect to periodic points changes. Note that the stability of periodic points mentioned here is not stability for the mapping system f, but for the mapping systems F and $\overline{F_k}$. Also, a stable periodic point for the system $\overline{F_k}$ is a periodic point for which the magnitudes of the eigenvalues of $D\overline{F_k}$ are all less than 1. Now consider the Jacobian for $\overline{F_k}$,

$$\frac{d\boldsymbol{x}_{i+1}}{d\boldsymbol{x}_i} = I + hC_k(Df^m(\boldsymbol{x}_i) - I). \tag{A.8}$$

From the equation (A.8), if the real parts of the eigenvalues in the $C_k(Df^m(\boldsymbol{x}_i) - I)$ are all negative, the periodic orbits with peirod m that were unstable in F becomes stable and can be found by repeating the mapping $\overline{F_k}$ if we take h sufficiently small. The SD method is an algorithm for finding stable periodic points by trying all possible C_k, but it is not obvious whether all periodic points can be found by doing so. The following conjecture is given in [110].

Conjecture 1 (Schlemmer-Diakonos)**.** Let $\mathscr{C}_{SD}$ be the set of all orthogonal matrices such that each entry is either -1 or $+1$. For any $N \times N$-regular matrix G, such that all eigenvalues of CG are negative, there exists some stabilising matrix $C \in \mathscr{C}_{SD}$ such that all eigenvalues of CG are negative.

For the maps of 2-dimensions or less, the conjecture 1 has indeed been proved to be true, but not for 3-dimensions or more [110]. From the conjecture 1, we can say that for equation (A.8), there always exists C_k such that all eigenvalues of $C_k(Df(\boldsymbol{x}_i) - I)$ are negative. If the value h is small, the absolute values of the eigenvalues of $I + hC_k(Df(\boldsymbol{x}_i) - I)$ can all be smaller than 1, and stable periodic points can be found by applying the map $\overline{F_k}$ to $\boldsymbol{x}_i$

Here, we define the *basin of attraction* as follows.

Definition 7 (Basin of attraction)**.** For a discrete dynamical system $f : M \to M$ on M, let point $\mathfrak{p}$ be a fixed point. Then the set

$$B(\mathfrak{p}, f) = \{\boldsymbol{x} \in M \mid f^k(\boldsymbol{x}) \to \mathfrak{p} \ \ (k \to \infty)\}, \tag{A.9}$$

is called a basin of attraction to the point $\mathfrak{p}$.

By repeating the mapping f, the point sequence $\{\boldsymbol{x}_i\}_{i=0}^{\infty}$ converges if and only if some point in the point sequence enters the domain of the basin of the periodic point for the mapping f. Note that changing the value of h is equivalent to changing the size of the basin attraction to a periodic point. If the size of the basin for a periodic point is too small, the point sequence will not come into the basin attraction to the periodic point.

A.3 DL method

The DL method is a hybrid of the Newton and SD methods developed by Davidchack and Lai [76, 111]. As with the Newton and SD methods, the point sequence $\{\boldsymbol{x}_i\}_{i=0}^{\infty}$ is obtained by repeating the following formula

$$F : \boldsymbol{x}_{i+1} = \boldsymbol{x}_i + [\beta s_i C^T - J(\boldsymbol{x}_i)]^{-1} g(\boldsymbol{x}_i), \tag{A.10}$$

where T denotes the transpose of the matrix. β is a suitable constant and $s_i := ||g(\boldsymbol{x}_i)||$. C is a stabilisation matrix as used in the SD method.

In the following, we derive Eq. (A.10). First, consider the following map, which has a form similar to that of the SD method (but unlike the SD method, it is an implicit Euler method),

$$F_0 : \boldsymbol{x}_{i+1} = \boldsymbol{x}_i + hCg(\boldsymbol{x}_{i+1}). \tag{A.11}$$

Expand $g(\boldsymbol{x}_{i+1})$ around $\boldsymbol{x}_i$ to the first order of h as

$$g(\boldsymbol{x}_{i+1}) \simeq g(\boldsymbol{x}_i) + J(\boldsymbol{x}_i)\Delta\boldsymbol{x}_i + O((\Delta\boldsymbol{x}_i)^2), \tag{A.12}$$

where $\Delta\boldsymbol{x}_i = \boldsymbol{x}_{i+1} - \boldsymbol{x}_i$. Substitute (A.12) into equation F_0, we find that

$$\boldsymbol{x}_{i+1} \simeq \boldsymbol{x}_i + hCg(\boldsymbol{x}_i) + hCJ(\boldsymbol{x}_i)\Delta\boldsymbol{x}_i + O((\Delta\boldsymbol{x}_i)^2).$$

Ignoring the terms beyond the second order in $\Delta\boldsymbol{x}_i$ and rearranging, we have

$$\boldsymbol{x}_{i+1} - \boldsymbol{x}_i = (\beta I - CJ(\boldsymbol{x}_i))^{-1} Cg(\boldsymbol{x}_i), \tag{A.13}$$

where $\beta = 1/h$. Using $C^T C = CC^T = 1$ and $C^T = C^{-1}$ we have

$$F : \boldsymbol{x}_{i+1} = \boldsymbol{x}_i + [\beta C^{\mathrm{T}} - J(\boldsymbol{x}_i)]^{-1} g(\boldsymbol{x}_i). \tag{A.14}$$

By replacing β with βs_i, the equation (A.10) is derived. Near the periodic point, s_i approaches 0. In this case, we get $F : \boldsymbol{x}_{i+1} \simeq \boldsymbol{x}_i - J(\boldsymbol{x}_i)^{-1} g(\boldsymbol{x}_i)$, which is similar to the Newton method (A.5). Since β is the reciprocal of the step width h, the step width in each iteration becomes smaller with increase of β. Also, increasing the size of β reduces the size of the basin $B(\mathfrak{p}, F)$ of the periodic point $\mathfrak{p}$ with respect to the map F.

The DL method has been proved to cover all periodic points with period m only for one-dimensional maps when periodic points with period $m-1$ are taken as the initial values of iteration [111]. The DL method [76] uses initial values of the periodic points with neighboring periods $m-1, m+1$ when searching for the periodic points with period m. In chaotic regions, periodic orbits with period m are often located near periodic orbits with period $m-1$ and $m+1$, so the number of steps required before the point sequence $\{\boldsymbol{x}_i\}_{i=0}^{\infty}$ converges is reduced by using these as the initial conditions. In Ref. [76], the periodic points for a strongly chaotic system are calculated, and it is assumed that all periodic points with period m have been found by taking the periodic points with period $m-1$ as initial values.

In the calculation done in this thesis, the periodic points are not calculated for strongly chaotic systems, but for the system with mixed phase space. There are no specific parameter restrictions on the intensity of chaos for applying the DL method. Nevertheless, numerical calculations show that the point sequences $\{\boldsymbol{x}_i\}_{i=0}^{\infty}$ often converge to a point close to the initial value. A possible explanation for why all the periodic orbits cannot be obtained is that if several stable periodic orbits are associated with a single stabilisation matrix C, they may converge to a nearby stable periodic orbit.

In the following, we will discuss how to improve the numerical accuracy when using the DL method to find periodic orbits. In the DL method, if $\beta s_i = 1/h$ is small, the step width is so large that the periodic orbit can be approached only by a step width even if the map is repeated. To increase the numerical accuracy of finding the periodic orbit, the value of β must be reduced. However, as mentioned earlier, the larger β is, the smaller the width of the mapping step $|\boldsymbol{x}_{i+1} - \boldsymbol{x}_i|$ becomes, which increases the calculation time. Therefore, we increase the size of β only when approaching the desired periodic orbit. If one can reduce the step size by increasing the size of $1/\beta$, then it becomes possible to approach the periodic orbit by a distance of the $1/\beta$. If the value of the corresponding s_i becomes small enough by increasing β, then $\boldsymbol{x}_i$ at that time is taken as the periodic point $\boldsymbol{x}^*$. The following algorithm is an example of how to increase the value of β.

Below, we provide an explicit procedure of the DL method for finding periodic orbits with period m in mixed phase space.

1. Prepare a sufficient number of grids in phase space and take a point on each grid as an initial value. Determine the value of β appropriately.
2. Choose one initial value and one stabilisation matrix $\{C_k\}_{k=1}^{2^N N!}$. Repeat the mapping (A.10) respectively. As s_i decreases, β is increased so that step size $s_i\beta$ is kept approximately constant. Continue this process until $1/\beta$ is smaller than the desired accuracy and find the periodic point $\boldsymbol{x}^*$.
3. When one periodic orbit with period m is obtained, iterate $m-1$ times to calculate all the points belong to the same periodic orbit.
4. Remove the already found periodic points from the found periodic points.
5. Repeat the steps 2-4 above for all stabilization matrices $\{C_k\}_{k=1}^{2^N N!}$.
6. Repeat the above steps 1-5 for all the initial values.

Bibliography

[1] M. J. Davis and E. J. Heller, J. Chem. Phys. **75**, 246 (1981).

[2] S. Creagh, Tunneling in Complex Systems (World Scientific, Singapore, 1998) (1998).

[3] S. Keshavamurthy and P. Schlagheck, *Dynamical tunneling: theory and experiment* (CRC Press, 2011).

[4] R. Iijima, R. Koda, Y. Hanada, and A. Shudo, Phys. Rev. E **106**, 064205 (2022).

[5] C. Dembowski, H.-D. Gräf, H. Harney, A. Heine, W. Heiss, H. Rehfeld, and A. Richter, Physical review letters **86**, 787 (2001).

[6] W. A. Lin and L. E. Ballentine, Phys. Rev. Lett. **65**, 2927 (1990).

[7] S. Tomsovic and D. Ullmo, Phys. Rev. E **50**, 145 (1994).

[8] S. Shinohara, T. Harayama, T. Fukushima, M. Hentschel, T. Sasaki, and E. E. Narimanov, Physical review letters **104**, 163902 (2010).

[9] D. A. Steck, W. H. Oskay, and M. G. Raizen, science **293**, 274 (2001).

[10] O. Brodier, P. Schlagheck, and D. Ullmo, Phys. Rev. Lett. **87**, 064101 (2001).

[11] O. Brodier, P. Schlagheck, and D. Ullmo, Ann. Phys. **300**, 88 (2002).

[12] A. Bäcker, R. Ketzmerick, S. Löck, M. Robnik, G. Vidmar, R. Höhmann, U. Kuhl, and H.-J. Stöckmann, Phys. Rev. Lett. **100**, 174103 (2008).

[13] A. Bäcker, R. Ketzmerick, S. Löck, and L. Schilling, Phys. Rev. Lett. **100**, 104101 (2008).

[14] S. Löck, A. Bäcker, R. Ketzmerick, and P. Schlagheck, Phys. Rev. Lett. **104**, 114101 (2010).

[15] A. Bäcker, R. Ketzmerick, and S. Löck, Phys. Rev. E **82**, 056208 (2010).

[16] P. Schlagheck, A. Mouchet, and D. Ullmo, in *Dynamical Tunneling: Theory and Experiment*, edited by S. Keshavamurthy and P. Schlagheck (CRC Press, 2011), p. 177.

[17] J. Le Deunff, A. Mouchet, and P. Schlagheck, Phys. Rev. E **88**, 042927 (2013).

[18] S. Coleman, Phys. Rev. D **15**, 2929 (1977).

[19] A. Shudo and K. S. Ikeda, Phys. Rev. Lett. **74**, 682 (1995).

[20] A. Shudo and K. S. Ikeda, Physica D **115**, 234 (1998).

[21] A. Shudo and K. S. Ikeda, Phys. Rev. Lett. **76**, 4151 (1996).

[22] A. Shudo and K. S. Ikeda, Nonlinearity **29**, 375 (2016).

[23] E. Bedford and J. Smillie, Invent. Math. **103**, 69 (1991).

[24] E. Bedford and J. Smillie, J. Amer. Math. Soc. pp. 657–679 (1991).

[25] E. Bedford, M. Lyubich, and J. Smillie, Invent. Math. (1992).

[26] E. Bedford and J. Smillie, Math. Annal. **294**, 395 (1992).

[27] R. Koda and A. Shudo, J. Phys. A **55**, 174004 (2022).

[28] A. Shudo, Y. Ishii, and K. Ikeda, Europhys. Lett. **81**, 50003 (2008).

[29] M. Shibayama, *Zyutenkaisetu Hamiltonrikigakukei*, Bessatsu Suurikagaku (Saiensusha,

Tokyo, 2023).

[30] Y. Ohnuki and H. Yoshida, *rikigaku*, gendaibutsurigakugoutyo (iwanamisyoten, Tokyo, 2001).

[31] V. I. Arnol'd, *Mathematical methods of classical mechanics*, vol. 60 (Springer Science & Business Media, 2013).

[32] M. Tabor, *Chaos and Integrability in Nonlinear Dynamics: An Introduction, WileyInterscience.* (1989).

[33] B. V. Chirikov, Physics reports **52**, 263 (1979).

[34] R. C. Robinson, *An introduction to dynamical systems: continuous and discrete*, vol. 19 (American Mathematical Soc., 2012).

[35] S. Smale, The Mathematical Intelligencer **20**, 39 (1998).

[36] H. Ito, *Jyoubibunhouteishikito kaisekirigaku* (Kyouritsushuppannsha, Tokyo, 1998).

[37] S. C. Creagh, in *Tunneling in Complex Systems*, edited by S. Tomsovic (World Scientific, 1998), p. 35.

[38] F. Haake, *Quantum signatures of chaos (springer-verlag)* (2006).

[39] L. D. Landau and E. M. Lifshitz, *Quantum mechanics: non-relativistic theory*, vol. 3 (Elsevier, 2013).

[40] L. I. Schiff, *Quantum mechanics* (McGraw-Hill, New York, 1955).

[41] R. Roncaglia, L. Bonci, F. M. Izrailev, B. J. West, and P. Grigolini, Phys. Rev. Lett. **73**, 802 (1994).

[42] Y. Hanada, A. Shudo, and K. S. Ikeda, Phys. Rev. E **91**, 042913 (2015).

[43] F. Grossmann, *Theoretical femtosecond physics: atoms and molecules in strong laser fields* (Springer, 2018).

[44] Y. Hanada, K. S. Ikeda, and A. Shudo, to be submitted.

[45] M. C. Gutzwiller, J. Math. Phys. **12**, 343 (1971).

[46] M. C. Gutzwiller, *Chaos in classical and quantum mechanics*, vol. 1 (Springer Science & Business Media, 2013).

[47] L. S. Schulman, *Techniques and applications of path integration* (Courier Corporation, 2012).

[48] A. Shudo, Y. Ishii, and K. S. Ikeda, J. Phys. A **35**, L225 (2002).

[49] A. Shudo and K. S. Ikeda, in *Dynamical Tunneling: Theory and Experiment*, edited by S. Keshavamurthy and P. Schlagheck (CRC Press, 2011), p. 139.

[50] A. F. Beardon, *Iteration of rational functions: Complex analytic dynamical systems*, vol. 132 (Springer Science & Business Media, 2000).

[51] J. Milnor, *Dynamics in One Complex Variable.(AM-160):(AM-160)-*, vol. 160 (Princeton University Press, 2011).

[52] R. L. Devaney, *An introduction to chaotic dynamical systems* (CRC press, 2021).

[53] M. Klimek, London Math. Soc. Monogr.(NS) (1991).

[54] J. F. Ritt, Transactions of the American Mathematical Society **21**, 348 (1920).

[55] H.Tsuji, *Fukusotayoutaironkougi* (Saiensusya, 2013).

[56] H. Brolin, Ark. Mat. **6**, 103 (1965).

[57] M. Hénon, in *The Theory of Chaotic Attractors*, edited by B. R. Hunt, T.-Y. Li, J. A. Kennedy, and H. E. Nusse (Springer, 2004), pp. 94–102.

[58] S. Friedland and J. Milnor, Ergod. Theor. Dyn. Syst. **9**, 67 (1989).

[59] R. Devaney and Z. Nitecki, Commun. Math. Phys. **67**, 137 (1979).

[60] H. Ryouichi and S. Akira, Journal of Physics A: Mathematical and General **37**, 10521

(2004).
[61] J. H. Hubbard and R. W. Oberste-Vorth, Publications Mathématiques de l'IHÉS **79**, 5 (1994).
[62] J.-P. Demailly, *Complex analytic and differential geometry* (Citeseer, 1997).
[63] S. Morosawa, Y. Nishimura, M. Taniguchi, and T. Ueda, *Holomorphic dynamics*, vol. 66 (Cambridge University Press, 2000).
[64] M.-R. Herman, in VIII-*th international congress on mathematical physics (Marseille)* (1986), pp. 138–184.
[65] J.-C. Yoccoz, Astérisque **231**, 3 (1996).
[66] C. L. Siegel, Ann. Math. pp. 607–612 (1942).
[67] A. Shudo, Y. Ishii, and K. S. Ikeda, J. Phys. A **42**, 265101 (2009).
[68] A. Shudo, Y. Ishii, and K. S. Ikeda, J. Phys. A **42**, 265102 (2009).
[69] A. Shudo and K. S. Ikeda, Nonlinearity **21**, 1831 (2008).
[70] V. Lazutkin and C. Simó, Int. J. Bifurcation and Chaos **7**, 253 (1997).
[71] V. G. Gelfreich, V. F. Lazutkin, C. Simó, and M. B. Tabanov, Int. J. Bifurcation and Chaos **2**, 353 (1992).
[72] N. Mertig and A. Shudo, Phys. Rev. E **97**, 042216 (2018).
[73] H. Yoshino, R. Kogawa, and A. Shudo, Condensed Matter **5** (2020), ISSN 2410-3896.
[74] A. Ishikawa, A. Tanaka, K. S. Ikeda, and A. Shudo, Phys. Rev. E **86**, 036208 (2012).
[75] O. Biham and W. Wenzel, Phys. Rev. Lett. **63**, 819 (1989).
[76] R. L. Davidchack and Y.-C. Lai, Phys. Rev. E **60**, 6172 (1999).
[77] P. Schmelcher and F. K. Diakonos, Phys. Rev. Lett. **78**, 4733 (1997).
[78] J. Meiss, Rev. Mod. Phys. **64**, 795 (1992).
[79] H. Yoshino, N. Mertig, and A. Shudo, Nonlinearity **36**, 5097 (2023).
[80] T. Onishi, A. Shudo, K. S. Ikeda, and K. Takahashi, Phys. Rev. E **64**, 025201 (2001).
[81] E. Doron and S. D. Frischat, Phys. Rev. Lett. **75**, 3661 (1995).
[82] S. D. Frischat and E. Doron, Phys. Rev. E **57**, 1421 (1998).
[83] O. Bohigas, S. Tomsovic, and D. Ullmo, Phys. Rep. **223**, 43 (1993).
[84] O. Bohigas, D. Boosé, R. de Carvalho, and V. Marvulle, Nucl. Phys. A **560**, 197 (1993).
[85] G. M. Lando and A. M. O. de Almeida, Phys. Rev. Lett. **124**, 010402 (2020).
[86] P. Holoborodko, http://www.advanpix.com.
[87] A. Shudo, Y. Hanada, T. Okushima, and K. S. Ikeda, Europhys. Lett. **108**, 50004 (2014).
[88] J. Le Deunff, A. Mouchet, and P. Schlagheck, Phys. Rev. E **88**, 042927 (2013).
[89] H. Harada, A. Mouchet, and A. Shudo, J. Phys. A **50**, 435204 (2017).
[90] N. Mertig, J. Kullig, C. Löbner, A. Bäcker, and R. Ketzmerick, Phys. Rev. E **94**, 062220 (2016).
[91] F. Fritzsch, A. Bäcker, R. Ketzmerick, and N. Mertig, Phys. Rev. E **95**, 020202 (2017).
[92] K. Clauß, M. J. Körber, A. Bäcker, and R. Ketzmerick, Phys. Rev. Lett. **121**, 074101 (2018).
[93] J. H. Van Vleck, Proceedings of the National Academy of Sciences **14**, 178 (1928).
[94] S. C. Creagh, J. Phys. A **27**, 4969 (1994).
[95] I. C. Percival, Physica D **6**, 67 (1982).
[96] J. M. Greene and I. C. Percival, Physica D **3**, 530 (1981).
[97] A. Berretti and L. Chierchia, Nonlinearity **3**, 39 (1990).
[98] A. Berretti and S. Marmi, Phys. Rev. Lett. **68**, 1443 (1992).
[99] R. Krikorian, Publications mathématiques de l'IHÉS **135**, 1 (2022).

[100] R. Dingle, *Asymptotic expansions: their derivation and interpretation*, vol. 521 (Academic Press London, 1973).

[101] J. Écalle, *Les fonctions résurgentes:(en trois parties)*, vol. 1 (Université de Paris-Sud, Département de Mathématique, Bât. 425, 1981).

[102] A. Voros, Annales de l'I.H.P. Physique théorique **39**, 211 (1983).

[103] E. Delabaere, H. Dillinger, and F. Pham, J. Math. Phys. **38**, 6126 (1997).

[104] T. Kawai and Y. Takei, *Algebraic analysis of singular perturbation theory*, vol. 227 (Amer. Math. Soc., 2005).

[105] F. Olver, *Asymptotics and special functions* (CRC Press, 1997).

[106] M. V. Berry and C. J. Howls, Proc. R. Soc. London **434**, 657 (1991).

[107] C. Howls, Proc. R. Soc. London **453**, 2271 (1997).

[108] R. Koda, Y. Hanada, and S. Akira, Phys. Rev. E **108**, 054219 (2023).

[109] J. Le Deunff and A. Mouchet, Phys. Rev. E **81**, 046205 (2010).

[110] D. Pingel, P. Schmelcher, F. Diakonos, and O. Biham, **62**, 2119 (2000).

[111] A. Klebanoff and E. Bollt, Chaos, Solitons & Fractals **12**, 1305 (2001).

[112] J. J. Crofts and R. L. Davidchack, SIAM Journal on Scientific Computing **28**, 1275 (2006).